Enhancement of Diamagnetic CEST MRI Contrast Efficiency: An Electronic and NMR Experimental Parameter Optimization Approach

By

SUBHAYAN CHAKRABORTY

CHEM11201504015

National Institute of Science Education and Research Bhubaneswar, Odisha – 752050

A thesis submitted to the
Board of Studies in Chemical Sciences
In partial fulfillment of requirements
for the Degree of

DOCTOR OF PHILOSOPHY
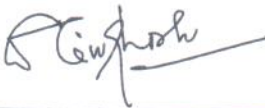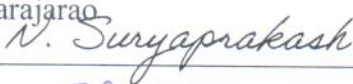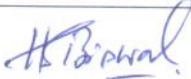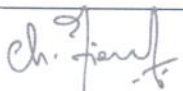
of

HOMI BHABHA NATIONAL INSTITUTE

October, 2021

Homi Bhabha National Institute[1]

Recommendations of the Viva Voce Committee

As members of the Viva Voce Committee, we certify that we have read the dissertation prepared by **Subhayan Chakraborty** entitled **"Enhancement of Diamagnetic CEST MRI contrast efficiency: An electronic and NMR experimental parameter optimization approach "** and recommend that it may be accepted as fulfilling the thesis requirement for the award of Degree of Doctor of Philosophy.
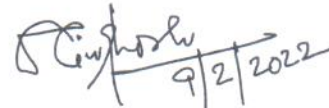
Chairman – Prof. A. Srinivasan		Date: 09.02.2022
Guide/Convener- Dr. Arindam Ghosh		Date: 9/2/2022
Examiner-Prof.SuryaprakashNagarajarao		Date: 09/02/2022
Member 1-Dr. Moloy Sarkar		Date: 09/02/2022
Member 2-Dr. Himansu Sekhar Biswal		Date: 09/02/2022
Member3-Dr.TirumalaKumarChowdary		Date: 09/02/2022

Final approval and acceptance of this thesis is contingent upon the candidate's submission of the final copies of the thesis to HBNI.

I/We hereby certify that I/we have read this thesis prepared under my/our direction and recommend that it may be accepted as fulfilling the thesis requirement.

Date: **09.02.2022**

Place: **NISER, Bhubaneswar**

(Dr. Arindam Ghosh)

Guide

---

[1] This page is to be included only for final submission after successful completion of viva voce.

STATEMENT BY AUTHOR

This dissertation has been submitted in partial fulfillment of requirements for an advanced degree at Homi Bhabha National Institute (HBNI) and is deposited in the Library to be made available to borrowers under rules of the HBNI.

Brief quotations from this dissertation are allowable without special permission, provided that accurate acknowledgement of source is made. Requests for permission for extended quotation from or reproduction of this manuscript in whole or in part may be granted by the Competent Authority of HBNI when in his or her judgment the proposed use of the material is in the interests of scholarship. In all other instances, however, permission must be obtained from the author.

Subhayan Chakraborty

DECLARATION

I, hereby declare that the investigation presented in the thesis has been carried out by me. The work is original and has not been submitted earlier as a whole or in part for a degree / diploma at this or any other Institution / University.

Subhayan Chakraborty

List of Publications arising from the thesis: ([#] Pertaining to The Thesis)

Journal Published

1. [#]**Subhayan Chakraborty**, Mainak das, A Srinivasan*, Arindam Ghosh* *New J. Chem.*, **2021**,45, 1262-1268.

2. [#]**Subhayan Chakraborty**, S Peruncheralathan*, Arindam Ghosh* *RSC Adv.*, **2021**,11, 6526-6534.

3. Rabindra Nath Pradhan, **Subhayan Chakraborty**, Pratibha Bharti, Janesh Kumar, **Arindam Ghosh***, Akhilesh Singh* *Dalton Trans.*, **2019**,48, 8899-8910.

4. Abhilash Chandra, Prabhat Kumar Sahu, **Subhayan Chakraborty**, Arindam Ghosh**,** Moloy Sarkar (equal contribution) ,*MRC,***2018***,* 56, 120-126.

5. Milan Pramanik, Khokan Choudhuri, **Subhayan Chakraborty,** Arindam Ghosh**,** Prasenjit Mal* *Chem. Commun.*, **2020**,56, 2991-2994.

6. A K Naik, U pandey, R Mukherjee, S Mukhopadhyay, **Subhayan Chakraborty**, Arindam Ghosh, P Aich* *Toxicol. Res.*, **2019**,8, 361-372

Manuscript Communicated

7. Shalini Pandey, **Subhayan Chakraborty,** Rimilmandrita Ghosh**,** S. Peruncheralathan,***** Arindam Ghosh***** " The role of hydrogen bonding in tuning CEST contrast efficiency: A comparative study of intra and inter-molecular hydrogen bonding." (*manuscript submitted*)(equal contribution)

Manuscript under preparation

8. [#]**Subhayan Chakraborty,** Arindam Ghosh***** "Enhancement of diamagnetic CEST MRI contrast efficiency: An NMR experimental parameter optimization approach"

CONFERENCE AND PRESENTATIONS

1. **Poster Presentation:** Functional and Supramolecular Smart Materials (FSSM-2020) at IIT Kharagpur on (29-30)th January,2020, Title: 'Impact of stereo-electronic properties of molecules on CEST efficiency'

2. **Poster Presentation:** Nuclear Magnetic Resonance Society (NMRS-2020) at Saurashtra University on (18-21)st February 2020, Title: 'Impact of NMR experimental parameters on CEST efficiency'

Subhayan Chakraborty

Dedicated
To
My Parents

ACKNOWLEDGEMENTS

CONTENTS **Page No**

CHAPTER 2: Instrumentation and Methods

List of Figures

CHAPTER 3: TmPyP as a potential diaCEST agent

CHAPTER 5: Optimization of experimental NMR parameters towards enhanced diaCEST efficiency.

SUMMARY

The widespread popularity of Magnetic Resonance Imaging (MRI) as a non-invasive localized imaging technique can be attributed to a large extent to the invention of MRI contrast agents. Contrast agents bring clarity in the image by creating a difference in brightness (intensity) between the region of interest and the surroundings. They are classified based on their working principle behind generating the contrast. The traditional relaxation-based contrast agents shorten either the longitudinal or the transverse relaxation time constants of the solvent water to infuse intensity variation. However, relaxation based contrast agents mostly contain metal and hence are considered unsafe. The search for alternative contrast agents led to the introduction of Chemical Exchange Saturation Transfer (CEST) based contrast agents in the year 2000. This class of contrast agents is again broadly divided into two categories based on the presence (paraCEST) or absence (diaCEST) of a metal center. In spite of the fact that paraCEST agents are more efficient in creating contrast, the safety aspect prompted many to look for efficient contrast agents within the large repertoire of already known 'safe' molecules. In a different vein, search for avenues to enhance the CEST efficiency of the diaCEST contrast agents also began. The present thesis work introduces methods for enhancement of CEST efficiency either by altering the electronic structure of a system or by suitably modifying the experimental NMR parameters. In brief, the first working chapter proposes a simple modification that makes a porphyrine derivative a potential diaCEST contrast agent having high CEST contrast efficiency in a large range of pH compared to the first reported porphyrin where the exchange rate and therefore the CEST efficiency drops drastically at physiologically relevant temperature and pH. The second working chapter first demonstrates how hydrogen bonding in acetanilide derivatives enhances the CEST efficiency and can work as a physiologically relevant diaCEST agent at physiological condition and then proposes paracetamol,

a well-known analgesic as a potential diaCEST contrast agent. The third working chapter shows that given a contrast agent, suitable parameter optimization can enhance the efficiency and demonstrates that the efficiency of an already reported highly efficient diaCEST contrast agent (salicylic acid) can be further elevated through parameter optimization. In a different vein, we also introduce CEST as a reliable and quick analytical tool for the estimation of average power delivery associated with any shape pulses.

CHAPTER 1

Introduction

Nuclear Magnetic Resonance was originally developed as a method to correlate nuclear properties of atoms and magnetic field. Gradually it evolved as an essential technique to understand the structure of organic molecules as well as polymers. In 1970s, NMR was revolutionized into an altogether new domain as new techniques were developed to extract spatial information that had practical value in the field of biology and medicine. As NMR slowly started getting attention in biochemical analysis, attempts were made to employ NMR as a non-invasive diagnostic tool in biology. Detection of metabolites at the physiological concentration in the millimolar range became possible with the invention of high-field magnets and pulse Fourier transform methods. Eventually, wide bore magnets, having modernized design of probes including surface coils and localization techniques, were developed that could easily examine humans and animals. These advancements constituted the upsurge for *in-vivo* application of NMR. Raymond Damadian was first to notice that longitudinal NMR relaxation rate of water varies greatly from healthy to tumor tissues in rats.[1] It was suggested that this might be an alternative way to study tumors. Nobel prize winner professor Paul Lauterbur later said, 'The attention of the medical community was first attracted by the report of Damadian that some animal tumors have remarkably long water proton NMR relaxation time'. Lauterbur explored Damadian's experiments and was highly satisfied with the outcome, indicating that NMR was indeed a promising diagnostic tool for examining tumors. He, however, pointed out that the only problem associated with this protocol would be the invasive nature of NMR measurements as the tissue must be removed from the body and studied *ex-vivo*. Lauterbur later reported that 'biopsies were commonly done and examined by histologists, and I believed that NMR relaxation time measurements on tissue specimens were unlikely to contribute much to the rich variety of information from optical microscopy'. He started exploring the possibilities of measuring the longitudinal relaxation time of tissue water without taking them out

of the body. To be specific, the aim was to extract information through spatial selection from the NMR signal *in vivo*. The answer was lying in the judicious use of magnetic field gradients. A gradient is referred to as a controlled variation in the magnetic field as a function of space. In case of conventional NMR experiments, currents are passed through a specially designed solenoid surrounding the probe to diminish the inhomogeneities of the main magnetic field across the sample length. This process is termed as 'shimming' of a magnet. It was necessary to remove the undesired variation in the magnetic field to obtain sharp signals. The drawback underlying the shimming process was that it delivered precise chemical information at the cost of spatial information as the spatial degeneracies were removed. Lauterbur attempted using 'sets of linear gradients oriented in different directions' instead of removing the gradient coils altogether to retain both spatial as well as chemical information. The linear set of gradients eventually generated a multidimensional NMR image. The two-dimensional images were produced using back-projection of one-dimensional spectra obtained from each gradient. The animal that was used to produce an image for the first time was a clam having a diameter of 4mm, which was well fitted inside a 5mm sample tube.[2] Shortly after that Lauterbur put forward the protocol to obtain both spatial as well as chemical information simultaneously and named the protocol as "magnetic resonance spectroscopy imaging".[3] Peter Mansfield, in 1974, used a frequency selective pulse to excite only the region of interest inside an MRI scanner.[4] In 1974, Nobel prize winner Prof. Richard Ernst replaced the back-projection method through time-domain experiments with varying magnetic field gradients. This method was then further developed to formulate the concept of 'NMR Fourier Zeugmatography' by Kumar et.al.[5] Mansfield later developed useful images from the MRI radio signals by analyzing them mathematically. He also developed an MRI method known as EPI (Echo Planar Imaging) which is capable of producing multidimensional images much faster.[6] The

technique utilized his previously developed method for slice selection, to obtain imaging information from a single slice with one excitation pulse followed by a string of echoes that resulted from a very rapid and repeated switching of field gradients. This eventually led to the establishment of the protocol later termed as fMRI (functional Magnetic Resonance Imaging).

Gradually, MRI evolved to be a predominant tool for clinical diagnosis. It has proved to be a useful non-invasive method to produce multidimensional images of the brain, heart, as well as muscles. It has also proved its potential in the analysis of tumors in various organs. For their outstanding contributions in developing MRI methods Paul Lauterbur and Peter Mansfield were awarded the Nobel prize in medicine in the year 2003.

1. Contrast

Contrast is the luminescence or color difference that makes an object (or its image or display representation) distinguishable from the background. Contrast is generally determined in the visual perception of the real world by the difference in the color and brightness of the object of interest and other objects within the same field of view. The human visual system is more sensitive to contrast than absolute luminescence; regardless of the vast variations in lighting during the course of a day or from place to place, we can interpret the environment in a similar manner. The maximum contrast for an image is termed as contrast ratio or dynamic range.

Conventionally proton density-based contrast is used for clinical diagnosis. Proton density weighted images relate directly to the nuclei density in the area that is being imaged. Tissues having high proton density appear brighter in the image. Fat tissue contains a high density of proton nuclei, and thus, appears hyperintense.

Diffusion weighted imaging is another MRI protocol that uses variation in Brownian motion of water molecules to generate contrast. Tissues with cellular swelling have lower diffusion coefficients, and thus, appear brighter. This kind of imaging is useful for the characterization of cerebral ischemia.

A contrast agent (CA) is used to produce artificial contrast in situations where natural contrast is not sufficient.

1.1 Characteristics for a contrast agent (CA) suitable for clinical use

1.1.1 Good water solubility with low osmolality and viscosity

The extent of contrast produced in MRI depends significantly upon the concentration of CA injected (the typical dose lies in the millimolar range for low molecular weight Gd(III) complexes).[7] Such high concentration of the CAs are used to maximize the contrast efficiency. To address the problem of water solubility at high concentrations of CAs, hydrophilic groups (OH and carboxylic groups) have been introduced in the CA structure to enhance water-solubility.[8] The viscosity and osmolality are also very important factors for designing any CA because the contrast agents injected for imaging are concentrated and are injected in a relatively small volume.[9] Neutral complexes are therefore preferred in order to minimize the discomfort from the injection of high osmolality salt solution and to improve the dose tolerance.[10]

1.1.2 High Stability and low Toxicity

One of the key factors to be considered while designing CAs is that they should have low toxicity and should not produce any acute side effect.[11-12] CAs, in general, consist of heavy metal gadolinium (Gd) ions (commercially used) that are tightly encapsulated by organic multidentate

ligands to form complexes that are stable under physiological conditions. This is to ensure that dissociation of the complexes into toxic free Gd ion and ligand species can be avoided once the CA is administered to a patient.[13] Since lanthanide ions are hard acids, hard donor atoms (nitrogen and oxygen) that form kinetically and thermodynamically stable complexes at physiological conditions, are generally incorporated into the ligand systems.

1.1.3 Relaxivity

The fundamental property of any relaxation-based CA is the ability to alter the relaxation rates of water protons in presence of the agent. A potential relaxation-based CA must have a high relaxivity value for producing good contrast in MRI.[8] Generally, relaxivity is measured by the change of the relaxation rate (longitudinal or transverse) of the bulk water per unit concentration.

1.1.4 Rapid Clearance

For clinical use, CAs should be rapidly cleared from the body after injection to prevent any prolonged toxicity due to leaching of free metal ions from the coordinated ligand into tissue or organs. The faster removal is a necessity for the clinical CAs, because none of the MRI CA is 100% resistant to metal ions dissociation. The approved clinical CAs have three types of biodistribution: intervascular with renal elimination, extracellular with mixed renal and hepatobiliary elimination and extra cellular with renal elimination.[14]

2. Different types of contrast agents

An MRI CA is mainly used in clinical diagnosis for enhancing the information gained from an image. The work on the development of CAs started in 1980.[15] The first paper on MRI CA, published in 1984 by H. Weinmann, presented Gd complexes as potential MRI CAs.[16] In MRI,

the signal can be enhanced with the help of iQMR processing, without CAs, by shortening the scan time needed to acquire the images.[17] In presence of CAs the signal intensity of the particular region is different as compared to the regions not associated with the CAs. The first-generation CAs were designed to decrease the longitudinal relaxation time constant or T_1 of water protons. T_1 CAs mainly contain paramagnetic metal ions such as, Gd(III), Mn(II), and Fe(III) or stable free radicals, such as nitroxides.[18-19] These CAs are highly paramagnetic due to the presence of several unpaired electrons and thus decrease the spin-lattice relaxation time and give positive contrast.[20] On the other hand, the T_2 CAs decrease the spin-spin relaxation time constant and give negative contrast. T_2 CAs typically use superparamagnetic particles, such as iron oxides or Dy(III) metal ions.[21] These particles alter the spin-spin relaxation time by creating microenvironment capable of producing magnetic field inhomogeneity. As a result, the spins rapidly dephase with a decrease in effective T_2.

In the last few decades, a conceptually new class of CAs based on chemical exchange saturation transfer (CEST) has evolved that offers a viable alternative to conventional CAs for MRI. A CEST CA is always contains one or more exchangeable protons (-NH, -OH, or bound water) of amides, alcohols, imidazoles and pyrazoles that can undergo chemical exchange with the solvent water.[22-23]

To generate contrast through CEST in imaging, the exchangeable protons of the contrast agents are completely saturated with the application of frequency selective saturation pulse. Upon transfer of this saturation to the bulk water through chemical exchange, the signal intensity of the bulk water decreases mimicking proton density drop.[23] The effect is, however, observed only when the chemical shift difference ($\Delta\omega$) between two pools of protons (the solute and the solvent pools) is higher than or at least equal to the exchange rate of protons between the two pools.[22, 24]. The

importance of the artificial contrast and contrast agents can be understood from the total number of publications on MRI CAs till June, 2019 as depicted in figure 1.
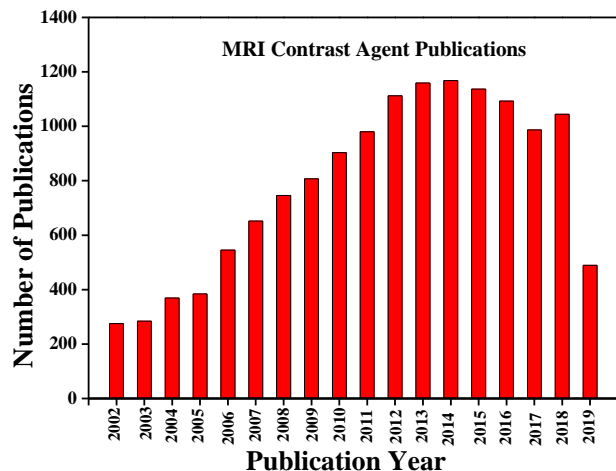
Figure 1: The number of publications focused on the concept of magnetic resonance imaging and contrast agents obtained from Scifinder web query (03/06/2019).

2.1 T1 CAs

The paramagnetic T_1 CAs consist of mostly Gd (III), or less commonly Mn (II) or Fe (III), where the multidentate ligand binds strongly to the metal ions to form kinetically and thermodynamically stable complexes. Gd-based CAs were first developed in the 1980s. The first clinically accepted Gd(III) CA (Magnevist) was approved by FDA in 1987. These Gd (III) ions are coordinated with eight coordination sites of ligands and the ninth coordination is completed by an exchangeable water molecule. For T_1 CAs, Gd(III) is the most widely used metal ion because it contains seven unpaired electrons. The seven unpaired electrons create a strong overall magnetic moment and the symmetric S-state of Gd (III) leads to shortening of the T_1 relaxation time constant of the bound water protons.

The extent of change to the relaxation time constant of the water molecules residing outside the first coordination shell of the Gd complex is dependent upon the strength of dipolar interaction between the electron spin, S, of gadolinium ion and the nuclear spin, I, of the water proton. For complete characterization of T_1 CAs many equations have been developed. To solve these equations, all the parameters that affect the T_1 relaxation time are required. These parameters can be obtained from NMR field cyclic experiments, electron paramagnetic studies and liquid NMR experiments at various pressures.[14, 25]

A T_1 weighted image is generated by utilizing the differential spin-lattice relaxation time of a tissue's net magnetization vector (NMV). Upon application of a non-selective 180^0 radiofrequency (RF) pulse, the bulk magnetization gets aligned antiparallel to the z-axis, which is a non-equilibrium state with no detectable transverse magnetization component. During a delay after the pulse, it starts relaxing back to the equilibrium. A readout pulse is then applied to measure the amount of magnetization that has been relaxed back to equilibrium. Protons in fat tissues possess relatively shorter T_1 and thus quickly relax back to equilibrium producing brighter regions in a T_1 weighted image. On the other hand, water, owing to its longer T_1 relaxation time, contributes to the darker part of the image. T_1 weighted imaging, therefore, generally employs short echo time (TE) and short repetition time (TR). The echo time is the delay between the application of the last RF pulse and the reception of the signal, whereas the repetition time is the delay between two repetitions of the pulse sequence to the slice. Without short TR, all the protons would relax back to the equilibrium, irrespective of long or short T_1, resulting in the formation of a uniformly intense image. Gd (III) CAs give positive contrast by decreasing the T_1 relaxation time constant of the water protons (Figure 2).
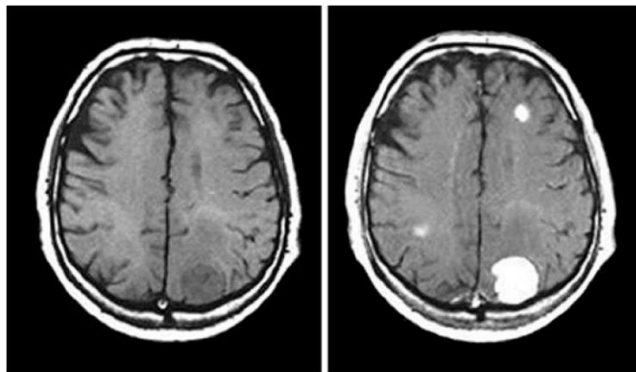
Figure 2: MRI images of brain (a) Pre-contrast (b) Positive contrast enhancement in a brain tumor obtained by using a T1-weighted CA Gd-DTPA. Image was adopted from reference.[26]

To assess the side effects and performance, when Omniscan (gadodiamide) was administered in ascending doses (from 0.05 mmol/kg to 0.3 mmol/kg) to 20 healthy male volunteers, it was observed that it had a distribution half-life of about 5 min in the intestine and the elimination (through kidney) half-life of approximately 70 min. Only mild post-injection side effects, such as dizziness, perversion of taste and light-headedness were registered in 9 out of 20 cases.[27] Patients with impaired kidney function or chronic liver disease are generally considered to be prone to risk while using Gd(III) based CA. This category of patients exhibited the symptoms of nephrogenic systemic fibrosis (NSF)[28], a rare disease caused by Gd CAs. Most of the cases have been reported with Omniscan.

2.2 T2 CAs

After an RF excitation, the transverse component of the magnetization relaxes back to equilibrium following an exponential pathway. Theoretically speaking, all nuclei in a particular environment should keep precessing with a single frequency in complete harmony. Contrary to that in real systems, due to the dissimilarity of the chemical micro-environment of the same nuclear spin in

different molecule, there exists a spread of resonance frequencies about the ideal frequency. With time this brings in decoherence of the alignment of the bulk transverse magnetization. The transverse magnetization decays following an exponential nature with time constant T_2, known as the spin-spin relaxation time constant. The method of refocusing of spin-magnetization is termed as spin-echo. The role of the refocusing pulse in a spin-echo sequence is to render the image free from the influence of field inhomogeneities. The spin-spin relaxation time is an inherent property of a molecule given an environment, such as water within tissues. T_2 of a molecule in different environment can change rather drastically. The T_2 weighted MRI is based upon the different transverse relaxation rate of water in tissues from that of free water outside the tissues. When the echo time is set to a long value, only the tissues with a longer spin-spin relaxation time survive to produce any signal.

In case of T_2 CAs, the field inhomogeneity produced by the metal ions alters the local magnetic field, leading to a shortening of the transverse relaxation time. As a result, the water signal intensity decreases. Typically, superparamagnetic iron oxides (SPIO) are used as T_2 based CAs. The magnetic field gradient produced by SPIOs efficiently dephases the transverse magnetization of water signals thus producing negative contrast (Figure 3). The superparamagnetic nanoparticles of iron oxide coated with dextran, silicates or other non-immunogenic polymers are currently being used as T_2 CAs. These surface coatings make the agent biocompatible, target selective and useful for multimodal applications. The tissue biodistribution and T_2 relaxivity of these CAs depend upon the size of the coated iron oxide particles. The different types of T_2 CAs include SPIO (superparamagnetic iron oxide, 50-500 nm), USPIO (ultrasmall superparamagnetic iron oxide, 4-50 nm), MION (monocrystalline iron oxide) and CLIO (cross-linked) nanoparticles.[29]

Recently lanthanide-based T_2 CAs have also been developed using the same macrocyclic chelators that were previously used for T_1 contrast agents. The lanthanides metals such as dysprosium (Dy^{+3}), thulium (Tm^{+3}) and terbium (Tb^{+3}) are used in these agents because they produce large hyperfine splitting and have high shifting capability. As an example, the chemical shift of bound water on a Dy^{+3} is observed as 700 ppm compared to the bulk water.[30] This large difference in frequency, dephases the water signal when the bound water exchanges with the bulk water, resulting in an overall decrease in the bulk water signal intensity.
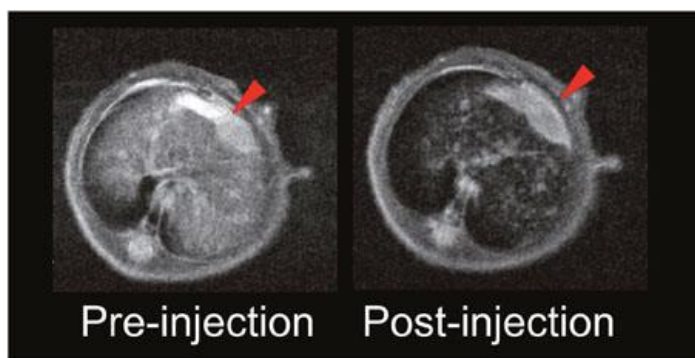
Figure 3. *In vivo* continuous observations of the orthotopic liver cancer model administrated with SPIO@Liposome-ICG-RGD. Image was taken from reference.**[31]**

2.3 CEST CAs

In recent years, chemical exchange saturation transfer, originally conceived as an NMR tool for binding studies, emerged as a promising contrast generation mechanism. As discussed in the last section, different contrast mechanisms use differential of different parameters such as, proton density, relaxation time constant or mobility (diffusion-weighted imaging). On the contrary, contrast through CEST depends on the 'solute-solvent' saturation transfer efficiency of a molecule having a labile proton resonating far away from water. The exchangeable protons of the solute are saturated by a frequency selective low power long RF perturbation and then the saturation is

transferred to bulk water through chemical exchange, resulting in a re-distribution of Zeeman level population and thereby decreasing the bulk water signal. The influence of transfer of saturation is termed as 'CEST effect'.

The idea of alteration of effective longitudinal magnetization by chemical exchange was first demonstrated by Forsen and Hoffman where the rate of chemical exchange between salicylaldehyde and 2-hydroxyacetophenone was first studied by using the magnetic double resonance method.[32] Nearly 30 years later, Balaban and co-workers proposed a new application of saturation transfer in the field of MRI by showing that application of selective RF pulse at the frequency of ammonium proton in an ammonium chloride solution resulted in a decrease in the bulk water intensity. [33] This, in turn, stimulated the study of biologically relevant exogenous as well as endogenous molecules as potential diamagnetic chemical exchange saturation transfer (diaCEST) CA. Around the same time several paramagnetic metal centers, coordinated with multi-dentate ligand were also used to create contrast through saturation transfer. The advantage of exogenous CAs lies in the fact that they can be chemically modified by altering their electronic as well as steric properties to tune the CEST contrast. This helps in removing the possible interference of either water direct saturation (DS) or magnetization transfer (MT) towards the CEST effect. Water direct saturation is undesired direct saturation of bulk water by the selective saturation pulse meant to saturate only the solute. Magnetization transfer, on the other hand, is related to the exchange of protons with semisolid macromolecules. Dipole-dipole interaction between protons of large macromolecules and water, having similar resonant Larmor frequencies, is held responsible for producing MT effects. Different classes of physiologically relevant exogenous CAs have been synthesized ever since the first report by Balaban and many of them exhibit appreciable contrast efficiency.

3. CEST THEORY

An exchangeable proton pool in contact with the bulk water is responsible for CEST. Let us denote the difference between the chemical shifts of the solute labile protons, and the bulk water as

$$\Delta\omega = \omega - \omega_0 \tag{1}$$

where the chemical shift of the labile protons is designated as ω and the chemical shift of the bulk water is designated as ω_0.

3.1 Saturation

In the backdrop of CEST, saturation refers to the equalization of two Zeeman level populations that in turn reduces the coherent signal of the labile protons. The overall bulk magnetization of the protons of interest eventually leads to zero when the preferential alignment of the spins with respect to the magnetic field is completely eliminated. At the starting of an experiment, the spins stay in thermal equilibrium. At thermal equilibrium, the population of the spins aligned parallel with respect to the static magnetic field is always higher compared to that aligned anti-parallel to the static magnetic field, since the former is energetically favorable. Saturation is achieved under the perturbation of a highly selective, long-duration RF pulse at the resonant frequency of the labile protons. The Bloch equation governing the precessional motion of the magnetization for an ensemble of spins, when modified to add the effects of RF irradiation along the x-axis of the rotating frame, is represented as[34]

$$\frac{dM_x}{dt} = \frac{-1}{T_2}M_x - 2\pi(\Delta - \Delta_0)M_y$$

$$\frac{dM_y}{dt} = \frac{-1}{T_2}M_y + 2\pi(\Delta - \Delta_0)M_x + \omega_1 M_z$$

$$\frac{dM_z}{dt} = \frac{M_0 - M_z}{T_1} - \omega_1 M_y \qquad (2),$$

where, M_x, M_y, and M_z represent the magnetization components of the solute along the directions of the Cartesian axes. M_0 represents the equilibrium magnetization of the pool, Δ_0 is the CEST pool offset frequency, Δ is the offset frequency of the saturation pulse, and ω_1 is the saturation pulse amplitude in rad/s. Gradually, the coherence of the spins in the transverse plane starts getting lost at the rate of transverse relaxation time. The continuous rotation of the spins under the application of RF irradiation helps in losing the original orientation due to dephasing. If the time derivatives of the previous equation are set to zero, then the equations predicting the magnetization at steady state become:

$$M_y = -\frac{T_2 \omega_1}{1 + T_1 T_2 \omega_1^2} \text{ and } M_z = \frac{1}{1 + T_1 T_2 \omega_1^2} \qquad (3),$$

where T_1 and T_2 represent the spin-lattice (longitudinal) and spin-spin (transverse) relaxation time of the solute respectively.

The saturation pulses are the most efficient when the transverse relaxation time is approximately 10-15% of the pulse length.[35] In order to have a significant saturation of the labile proton pool, the

pulse length must be at least five times the longitudinal relaxation time for the said spin. Apart from that the T_1 of water also plays a significant role. If the water T_1 is not sufficiently long, then the saturation would not survive for long.

According to the quantum mechanical description, a mixed state of a spin, where all the particles are not in the same state can be designated as a statistical mixture of many pure states. For a spin ½ nucleus, the spin state where the magnetization is aligned with respect to the external magnetic field is generally termed as "spin-up" while the other state is termed as the "spin-down". When a RF perturbation, with a frequency component at the resonance Larmor frequency of the spin is applied, it induces spin flip. The rate at which the spin angular momentum absorbs the RF irradiation and changes the state from spin-up to spin-down or the other way round is termed as transition probability per unit time and is generally designated by W.[36] With time under the continuous application of selective saturation pulse the spins attend equal population at both the spin states. This phenomenon is termed as saturation of the spin states. Once saturation is selectively incurred upon the labile protons of the solute it can be transferred to the bulk water spin pool through multiple pathways.

The amplitude of the selective saturation pulse is in general expressed in microtesla (µT). In case of modified Bloch equation, the frequency unit rad/s is more suitable for representing the amplitude of a saturation pulse.

$$\omega_1 = \gamma B_1[rad/s] = 2\pi \cdot \gamma B_1[Hz] = 2\pi \cdot B_1[\mu T] \cdot \gamma \left[\frac{Hz}{\mu T}\right] \tag{4}$$

For a specific pulse length with a specific shape the saturation pulse is in general described by the total nominal flip angle designated by *mtflip* in case of MRI scanners and is represented by

$$mtflip[deg] = \frac{\int_0^T \gamma B_1(t)dt}{2\pi}$$

(5),

where T corresponds to the duration of saturation pulse.
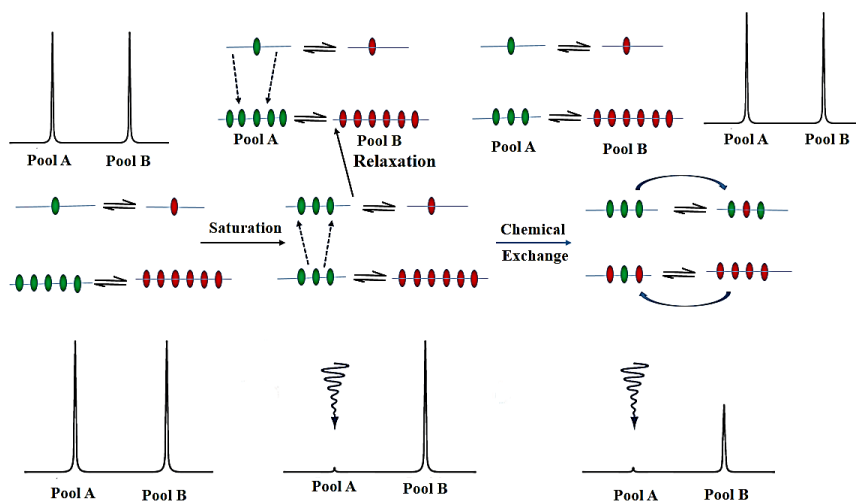
Figure 4. Schematic representations of the distribution of spins, aligned with and against the field; (left) peaks in absence of presaturation; (middle) after applying pre-saturation pulse to pool A; (right) after chemical exchange, decreasing the intensity of both peaks. If the relaxation of pool A is fast with respect to the rate of chemical exchange with pool B then the spins relax back to the ground state from high energy state and normal NMR spectra is obtained. Image was adopted from reference.[22]

3.2 Saturation transfer and exchange

There are different mechanisms through which a spin can perturb the magnetization and thus transfer saturation to the surrounding spins. While magnetization transfer refers to the crosstalk between two protons resulting in the alteration of their individual spin states, "saturation transfer" is the phenomena in which the saturation of one spin pool is transferred to another pool in 'contact'. This may happen either when the protons physically detach from one pool and enter the other spin

pool or via a transient interaction where the two protons are involved through the interaction of their corresponding magnetic fields. The former is an example of chemical exchange while the latter refers to cross-relaxation in case of semi-solid macromolecules. A proton might get involved in all the pathways simultaneously to different extents. Therefore, to have a theoretical understanding of the underlying phenomena, the predominant mechanisms must either be singled out, or multiple pathways must be incorporated into the theoretical model. The schematic is given in figure 4.

3.2.1 Dipole-dipole interaction:

Two spins interact through dipole-dipole interaction when they are close enough in space that the local magnetic field of one spin can be felt by the other spin.

The energy of dipole-dipole interaction is given by:

$$H = -\frac{\mu_0}{4\pi} \frac{\gamma_j \gamma_k}{r_{jk}^2} (3(I_j \cdot e_{jk})(I_k \cdot e_{jk}) - I_j \cdot I_k) \tag{6},$$

Where, *I* and γ are, respectively, the nuclear spin angular momentum, and the gyromagnetic ratio of the nucleus, r represents the spatial distance between the magnetic moments of different nuclei and 'e' corresponds to the unit vector along the line joining nucleus 'j' to nucleus 'k'. If the oscillation frequency of the dipolar interaction overlaps with the Larmor frequency, then a change in the spin state might be induced in neighboring protons. Transfer of energy can also occur between protons residing in either the same or different environments. Higher the spectral density component at the Larmor frequency, the more effective is the interaction and higher is the probability of changing the spin states of the surrounding nuclei.

3.2.2 Cross-relaxation and spin diffusion:

When mutual flip of the spin states is responsible for exchange in energy between two spins,[37] the process is termed as cross-relaxation. For cross-relaxation to happen, proximity of the two spins in space is necessary and hence it occurs when the two spins stay on the same molecule. Abundant nuclei of the same species participate in mutual spin flip. On the other hand, spin diffusion occurs when many such spins remain connected through a network and disturbance in any one of the spins is relayed to all the other spins residing in the network. Spin diffusion and cross-relaxation are the most significant ways through which relaxation occurs provided the product of the rotational correlation time of the whole molecule and the resonant Larmor frequency of the spins is much smaller than one. Such a criterion is fulfilled generally by large macromolecules or proteins.[37] Spin diffusion helps the spins residing in same environment to have the same spin temperature since any disturbance in one spin is effectively transferred to all the spins of the same network affecting only the z component of magnetization[38]. Although, spin diffusion influences longitudinal relaxation but it has almost no effect on spin-spin relaxation.[39] However, as the spins remain in close proximity, their coherent phase is lost instantaneously resulting in a smaller spin-spin relaxation time. Thus, upon application of an RF saturation pulse on any of the spins residing in the extended spin network, the effect is eventually relayed to the full set of interconnected spins. Magnetization transfer imaging predominantly utilizes this mechanism.

3.2.3 NOE

The Nuclear Overhauser effect (NOE) comes into play when a spin, having dipolar interaction with other spins, residing in close proximity, is saturated via application of an RF perturbation. As discussed earlier, a saturated spin pool consists of an equal population of spin-up and spin-down states. A dipolarly coupled system of spins may transfer energy through different mechanisms.

When a pair of spin up nuclei is converted to spin down state or the other way round, the mechanism involved is termed as double quantum transitions. Similarly, the single spin-flip is referred to as single quantum interaction while zero-quantum interactions induce a simultaneous flip of a spin up-down pair. The probability of the transitions is exclusively dependent upon the correlation time of the coupled spins as well as the strength of the dipolar interaction and the respective gyromagnetic ratios. In the case of homonuclear magnetization, the double quantum transition is produced at an energy that is equivalent to double the Larmor frequency of any of the involved spins, while the zero-quantum transition is equivalent to zero frequency. Followed by an RF perturbation, the energy of the saturated system starts getting relayed to the non-saturated spins residing in the network and consequently, their bulk z-magnetization starts changing. Dipolar coupling between slowly rotating aliphatic protons of large macro-molecules are responsible for negative NOE in CEST experiments when a long saturation pulse (longer than the longitudinal relaxation value of tissue) is applied for saturation of labile protons.[40]

3.2.4 Chemical exchange

Chemical exchange is the phenomenon where a proton physically detaches from one molecule and attaches to another molecule. Occurrence of the event per second is defined as the exchange rate. The exchange rate which is relevant to CEST should be less than the difference of chemical shift between the labile protons of the solute and the bulk water in order CEST is observed. Although, two pools of protons are involved in the process of saturation transfer via chemical exchange, the chemical rate process is described via a pseudo-first order dynamics. This is attributed to the fact that the high concentration of bulk water (in the order of 55.5M compared to the solute concentration lying in the range of millimolar) is not altered during the exchange process and thus

can be taken as a constant term. The equation characterizing the rate of change of concentration of the respective pools in two-pool exchange phenomena can be written as follows:

$$\frac{dM_A}{dt} = -K_{AB}M_A + K_{BA}M_B$$

$$\frac{dM_B}{dt} = -K_{BA}M_B + K_{AB}M_A \qquad (7).$$

The exchange rate constant is determined by the number of times an exchange favorable condition, such as proximal distance, spatial orientation or charge distribution in the locality of the nuclei, are attained for a particular spin per unit time. However, the time required for one spin, to execute the physical detachment from one molecule and attachment to another molecule once the exchange has started, is sufficiently small. This helps conserve the saturation that has been incurred. Thus, chemical exchange is one of the pathways through which saturation incurred upon one spin can be efficiently transferred to other spins with which physical exchange is taking place.

One of the greatest confusions that lies inherently with the CEST measurements is the intertwined effect of magnetization transfer pathways other than chemical exchange. This often leads to a spurious inference of the experimental observations. Carefully chosen experimental parameters might lead to the dominance of one of the pathways. For example lowering the temperature reduces the exchange rate to the extent that the impact of chemical exchange becomes negligible.[41] Following the same rationale an increase of temperature leads to the removal of the effect of dipolar exchange pathways as the average residence time of one spin in close proximity with the other spin effectively reduces. In general, the spin-spin relaxation time relevant to magnetization transfer pool is smaller (in the order of µs) compared to the CEST pool (where the relaxation time is in the order of ms).

Irrespective of the type of exchange mechanism that is operating in the sample, the fundamental MR pulse sequences for detecting CEST and MT are similar. The basic pulse sequence consists of an RF saturation pulse applied at the resonance frequency of the labile proton of interest followed by a read pulse which measures the intensity drop of the bulk water signal due to the transfer of saturation incurred upon the labile protons.

CEST spectra (also known as z-spectra) are obtained by plotting normalized ($100 \times M_z / M_0$) water signal intensities as a function of the frequency offsets of saturation with respect to bulk water. M_z is the net magnetization of water protons after application of a frequency selective RF perturbation having sufficient duration and amplitude to saturate the labile protons. M_0 is the intensity of water signal at thermal equilibrium in absence of any saturation transfer. In a CEST spectrum, two inverted peaks (or dips) are generally observed when the saturation pulse is scanned across the resonance frequency of water. The highest intensity peak at 0 ppm offset (with respect to water position) arises due to the direct saturation of water and the second low-intensity peak is due to diminished intensity of water signal after exchange with the contrast agent protons (assuming only one type of exchangeable proton exists). As CEST effect decreases the water signal intensity of bulk water , negative contrast is obtained (Figure 5).

The frequency offset of the solute proton is the most important parameter of a CEST agent when it is administered *in vivo*. During *in vivo* CEST imaging, large symmetrical background noise is generated owing to magnetization transfer (MT) between abundant water molecules and the labile protons of the endogenous biomacromolecules.[42] The MT effect is also present because of the semisolid nature of tissues, having very short T_2 value (< 1 ms).[43-46] The spillover of the signal intensity occurs in the region where the biological signal and the CA signal are mixed. There are two methods to overcome this spillover. First by increasing the number of exchangeable protons

of the CA, and second, by increasing the solute-solvent offset ($\Delta\omega$). The approach of increasing the concentration through naturally occurring diaCEST agents is useful; however, due to the small chemical shift difference ($\Delta\omega$) of the exchangeable protons, the CEST effect of the CA overlaps with strong endogenous MT effect, thereby, making it difficult to detect the signal of the CA. The second approach, that is, increasing $\Delta\omega$ to avoid the MT effect, is primarily achieved by introducing a paramagnetic center in the molecule that makes the exchangeable protons resonate at a frequency outside the region of the background tissue signal.
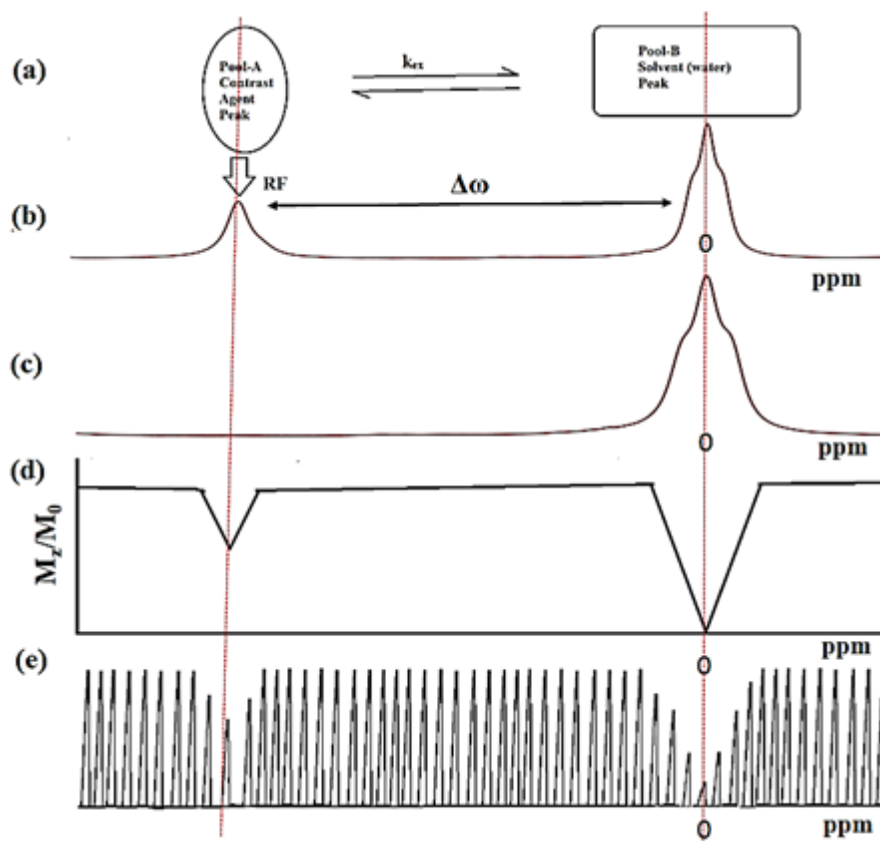
Figure 5. Schematic representation of a CEST experiment (a) Pool-B exchange with pool-A; (b) presaturation pulse is applied at pool-A; (c) signal at pool-A decreases with application of saturation pulse; (d) CEST spectrum: normalized (100 x Mz /M0) water signal intensities as a function of the presaturation pulse frequency offset from the bulk water; (e) representation of water signal intensity after the application of presaturation pulse as a function of saturation frequency. Image was taken from reference.[47]

The position of the solute exchangeable proton ($+\Delta\omega$) can be precisely obtained from a Z-spectrum. The frequency offset which is equal but on the other side of water (denoted as $-\Delta\omega$) gives the direct water saturation of $-\Delta\omega$ (as direct water saturation is symmetric). The CEST effect is then calculated from the asymmetric magnetization transfer ratio denoted by the following equation:

$$\text{CEST efficiency} = \frac{M(-\Delta\omega) - M(\Delta\omega)}{M(-\Delta\omega)} \times 100\% \tag{8}.$$

Where, $M(\pm\Delta\omega)$ is water intensity after saturation at $\pm\Delta\omega$

The estimation of CEST efficiency becomes erroneous for labile protons having high exchange rates. The widths of the direct saturation profile and the CEST peak are related to the lifetime of the exchangeable protons. When protons exchange between different pools, they can be present in both the pools during the acquisition time of the FID. This short lifetime in any particular pool, in turn, results in alteration of the position as well as the broadening of the width of the signal of the proton under consideration, according to the Heisenberg's uncertainty principle. For NMR spectroscopy, the uncertainty principle directly relates linewidth (LW) with transverse relaxation time constant T_2 as LW is inversely proportional to T_2. For finite T_2, the linewidth also becomes finite. Extra broadening of the resonance line occurs when a proton switches frequently between two pools, promoting rapid environment change. This causes an additional decrease in the transverse relaxation time constant. When the exchange rate is too fast, a single peak is observed at the average frequency of the solute and the solvent. When the exchange rate is faster in comparison to the NMR time scale, the coalescence of the two peaks starts. The disadvantage of the coalescing peak is that the frequency selective perturbation becomes problematic. On the other hand, the residence time should be shorter than T_1 of water to accommodate multiple exchange

event to increase saturation transfer. The exchange rate, that is optimum for CEST lies in the slow to medium exchange domain. With the increase in temperature exchange rate increases, which eventually leads to coalescence at a particular temperature where the exchange rate is higher than the difference in chemical shift. In such cases, as the CEST peak position is not well-defined, the magnetization transfer asymmetry is unable to produce the best CEST effect.

4. Type of CEST agents:

Depending upon the presence or absence of paramagnetic metal center, CEST agents are broadly classified into two categories. The next section is a detailed study of the already reported CEST agents

4.1 ParaCEST agents: The first paraCEST CA reported was Eu(III) tertaglycinate (EuDOTA-4AmC⁻) by Sherry and coworkers.[48] In Eu(III) complexes it is difficult to see the exchangeable amide protons signal, but in the case of other lanthanide complexes such as dysprosium (dy) or ytterbium (yb) they are easily detected in the spectrum.[49]The transition metal ions exhibit more covalent bond character compared to lanthanide ions, because the electrons of 4f orbitals are highly shielded by the filled 5s and 5p orbitals. This leads to greater covalent interactions causing a large contact contribution in addition to the pseudo contact interaction for transition metal ions. As a result, the exchangeable protons get highly shifted. The group of Prof. Dean Sherry and few other groups have used 1,4,7,10-tetraazacylododecane (CYCLEN), with four pendent groups with different exchangeable protons that coordinate with a lanthanide metal ion center, as a paraCEST CA.[48, 50-52]

4.2 DiaCEST agents: Balaban and coworkers have reported a large number of diamagnetic organic compounds as potential diaCEST MRI CAs,[33] including sugars, amino acids, nucleosides

and their purine and pyrimidine bases and barbituric acid and their derivatives. They also tested a few other classes of compounds like guanidine, hydantoin and imidazole derivatives. Although the CA concentration was quite high for most of these studies, almost all of them were able to produce appreciable CEST contrast at the physiological condition. Van zil and coworkers used CEST to detect the cationic polymers that exhibit great application in gene therapy.[53] For the cationic polymer the detection sensitivity was quite high due to the formation of polymeric chains. The polymers were termed as 'saturation amplifier' as the multiple numbers of protons having similar resonance frequency could be saturated simultaneously.Snoussi and coworkers investigated the CEST properties of RNA based polyuridylic acid having multiple units of uridine connected by phosphodiester bonds.[54] Zhou et. al. detected endogenous peptide and mobile proteins of very low concentration with the help of the water signal using CEST.[55-56] Van zjil and coworkers also detected glycogen (glycoCEST) through selective saturation of fast exchanging hydroxyl group resonating at 0.5-1.5 ppm frequency range with respect to bulk water.[57] Later, Chan and coworkers used D-glucose for detecting cancer.[31] The hydroxyl group of D-glucose exhibits favorable exchange rate to produce CEST contrast. They also established it's feasibility by applying it to two human breast cancer cell lines. Jin et. al. investigated the chemical exchange process between exchangeable protons of metabolite and water via spin lock and CEST method.[58] In order to compare between these two approaches, CEST and SL measurements were performed with concentrated amide, amine and hydroxyl protons at varying pH. Haris et. al investigated the concentration-dependent exchange effect of the exchangeable protons of the hydroxyl group of myo-inositol with bulk water.[59] Their work established the potential application of myo-inositol based CEST imaging for the early detection of Alzheimer's disease. The concentration and pH-dependent mapping of glutamate, an important neurotransmitter in the brain, through CEST was

previously demonstrated by Cai et. al.[60] Due to the presence of the exchangeable amine group, CEST signal appeared at ~3 ppm downfield with respect to water. The CEST effect along with the exchange rate of the major metabolites of creatine kinase namely ATP, creatine and phosphocreatine, was demonstrated by Haris et. al.[61] At physiological conditions, the exchange rate of creatine was found to be 7-8 times higher than that of ATP and phosphocreatine. Kogan and coworker measured the distribution of free creatine before and after plantar flexion exercise of the lower leg with the help of CEST.[62]Chan et. al. measured the decrease in CEST signal for L-arginine trapped in a liposomal vesicle in order to estimate the cell death. At a lower pH the exchange rate of base catalyzable amine protons, resonating at 2 ppm from bulk water, decreases and as a result the CEST effect also drops dramatically.[63] Ling and coworkers were able to measure the in-vivo concentration of glycosaminoglycan by studying the water exchange of both amide proton, resonating 3.2 ppm downfield with respect to water, and hydroxyl proton, resonating 0.9 to 1.9 ppm downfield with respect to water.[64] Bar-shir et. al. proposed a class of thymidine analogue as a probe to image the expression of herpes simplex virus type-1 thymidine kinase. The exchangeable imino protons resonate at 5-6 ppm downfield with respect to water and their identification is unperturbed by CEST contrast originating from endogenous agents.[65]

Aime et. al. proposed the use of iopamidol as a pH responsive diamagnetic CEST MRI CA.[66] The exchange rate of hydroxyl and amide functional groups shows excellent pH dependence. Iopamidol, conventionally used as a radiographic CA, was used as a ratiometric probe to investigate the pH of kidney where the agent is filtered. Although the exchange rate for hydroxyl proton was very high, the amide group resonating at ~5 ppm downfield with respect to water and having exchange rate in the range of slow to medium exchange regime with respect to NMR time scale, provided appreciable CEST contrast across the physiological pH. At all the examined values

of pH the amide proton having an offset of 4.2 ppm were shown to have lower exchange rate compared to the other proton having an offset of 5.5 ppm. Pagel et. al. compared the efficiency of pH mapping for iopromide and iopamidol.[67] Iopromide was shown to produce a high dynamic range measurement of pH for extracellular tissues compared to iopamidol. This observation was attributed to the precision difference that lies in the greater CEST effect produced by two equivalent amide protons of iopamidol resonating at an offset of 4.2 ppm. Ratiometric analysis based on RF power and therefore a novel ratiometric index was shown with iobitridol by Aime et. al.[68]

In spite of the wide applicability as was listed above, the inherent problem with any diaCEST CAs is the low chemical shift difference with respect to water. Because of the less chemical shift difference, water direct saturation profile has a tendency to mask the CEST peak. Moreover, low offset does not allow high exchanging protons to participate in CEST contrast generation. In presence of a macromolecule, due to the existence of NOE effect, the situation becomes even worse. In order to get rid of this problem McMahon et. al. proposed salicylic acid as an excellent candidate for diaCEST agent.[69] In case of salicylic acid, the carboxylic acid protons dissociate at the physiological pH due to its low pk_a, resulting in the formation of carboxylate anion. This carboxylate anion has a high tendency to work as hydrogen bond donor as the negative charge of the conjugate base becomes resonance stabilized. Due to the formation of this hydrogen bond,the exchange rate of the fast exchanging hydroxyl proton slows down to medium exchange regime necessary for producing CEST contrast. Banerjee et. al. developed salicylic acid based polymeric CA to exploit magnetic resonance imaging of prostate cancer treated with PSMA-targeted theranostics. Based on the above findings McMahon et. al. investigated the effect of electronic as well as steric factors in increasing the CEST efficiency of the hydroxyl proton of salicylic acid

analogues. It was observed that, as substitution can greatly affect the chemical shift of the exchangeable proton, it also plays a major role in enhancement of the CEST efficiency. They also investigated the role of water solvation in increasing the exchange rate as well as the CEST efficiency. Based on this study, a number of potential diaCEST agents using intra molecular shifted hydrogen bond have been reported. Imidazole based diaCEST agents were also reported by McMahon et. al. in which the exchange rate of the N-H proton of imidazole was reduced using intramolecular hydrogen bond.[70] McMahon et. al. proposed N-sulfonyl anthranilic acid based CEST agents where the exchange rate of amine protons resonating at an offset of 4-9 ppm from water were reduced by intramolecular hydrogen bonds. Based on this study they proposed flufenamic acid as a potential diamagnetic CEST MRI CA.[71]
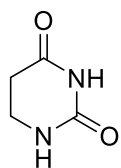
Dihydrouracil
(Balaban et al, 2000)
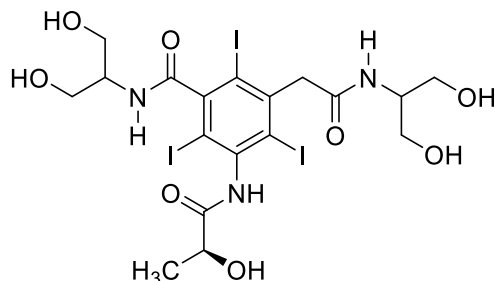
Iopamidol
(Aime et al, 2005)
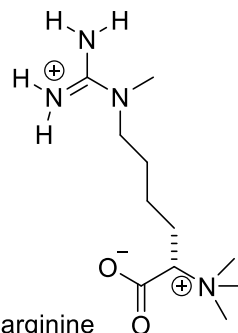
L-arginine
(McMahon et al, 2013)
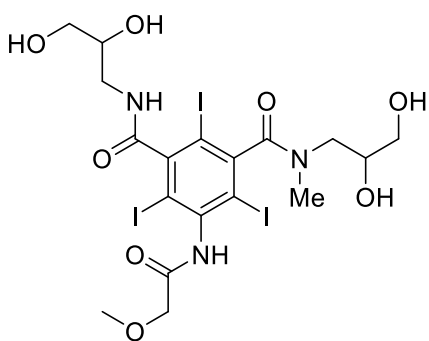
Iopromide
Pagel et al, 2013
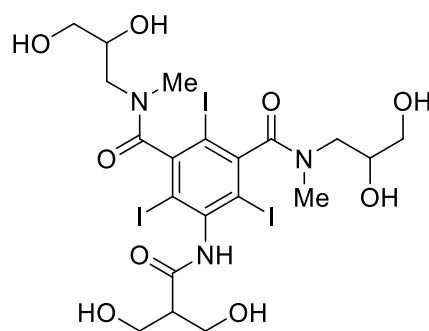
Iobitridol
Aime et al, 2014
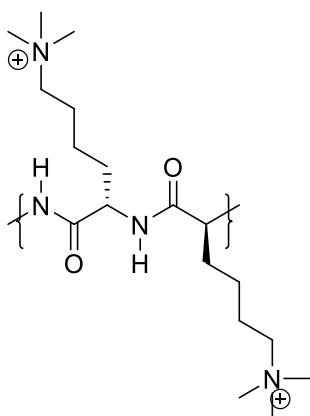
Poly-L-lysine
Van zjil and McMahon et al,2006
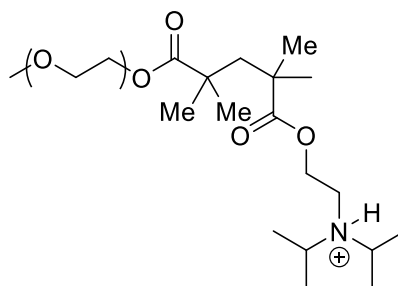
Block copolymers
Gao and Sherry et al, 2013

Chart 1: Few previously reported diaCEST agents.

2-hydroxybenzoic acid   2,5-dihydroxybenzoic acid   5-amino-2-hydroxybenzoic acid

McMahon et al, 2013

2,5-dihydroxyterephthalic acid   4,6-dihydroxyisophthalic acid   4,4'-methylenebis(3-hydroxy-2-naphthoic acid)
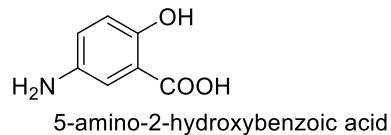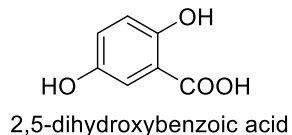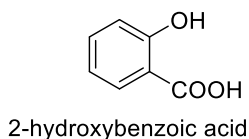
McMahon et al, 2014

2-(2,2,2-trifluoroacetamido)benzoic acid   2-(methylsulfonamido)benzoic acid   2-(phenylamino)benzoic acid

McMahon et al, 2014
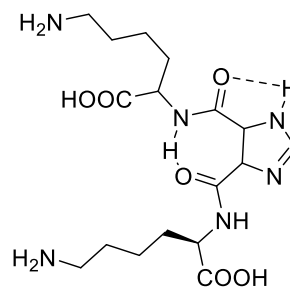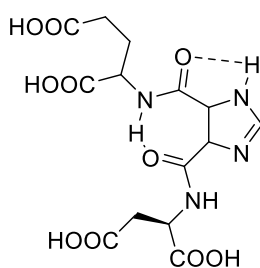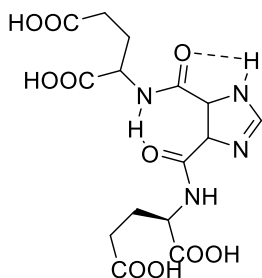
imidazole-4,5-dicarboxamide   4,5-bis[(Asp)carbonyl]-*1H* imidazole   4,5-bis[(Lys)carbonyl]-*1H*-imidazole

McMahon et al, 2016

4-oxo-4-(phenylamino)butanoic acid

N-(3-acetyl-4-(2-hydroxy-3-(isopropylamino)propoxy)phenyl)butyramide
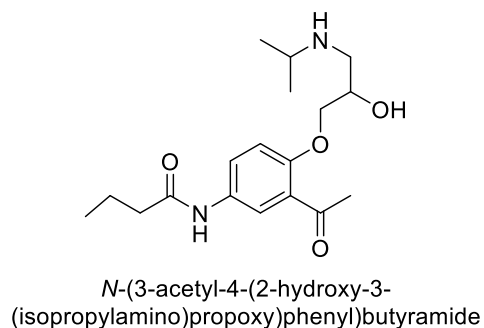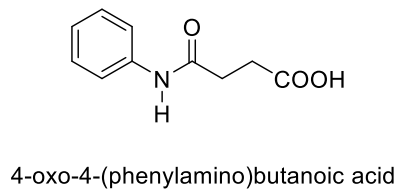
Liu et al, 2020

Chart 2: Few previously reported diaCEST agents based on intra-molecular hydrogen bond

In order to address the problem of low offset associated with diaCEST agents, McMahon et. al. proposed free base porphyrins as diaCEST agents. Due to the presence of diatropic ring current, the inner core N-H protons resonate at ~8-12 ppm up field with respect to the bulk water.[72]

TPPS$_4$

Uroporpyrin I

Hematoporphyrin

TCPP
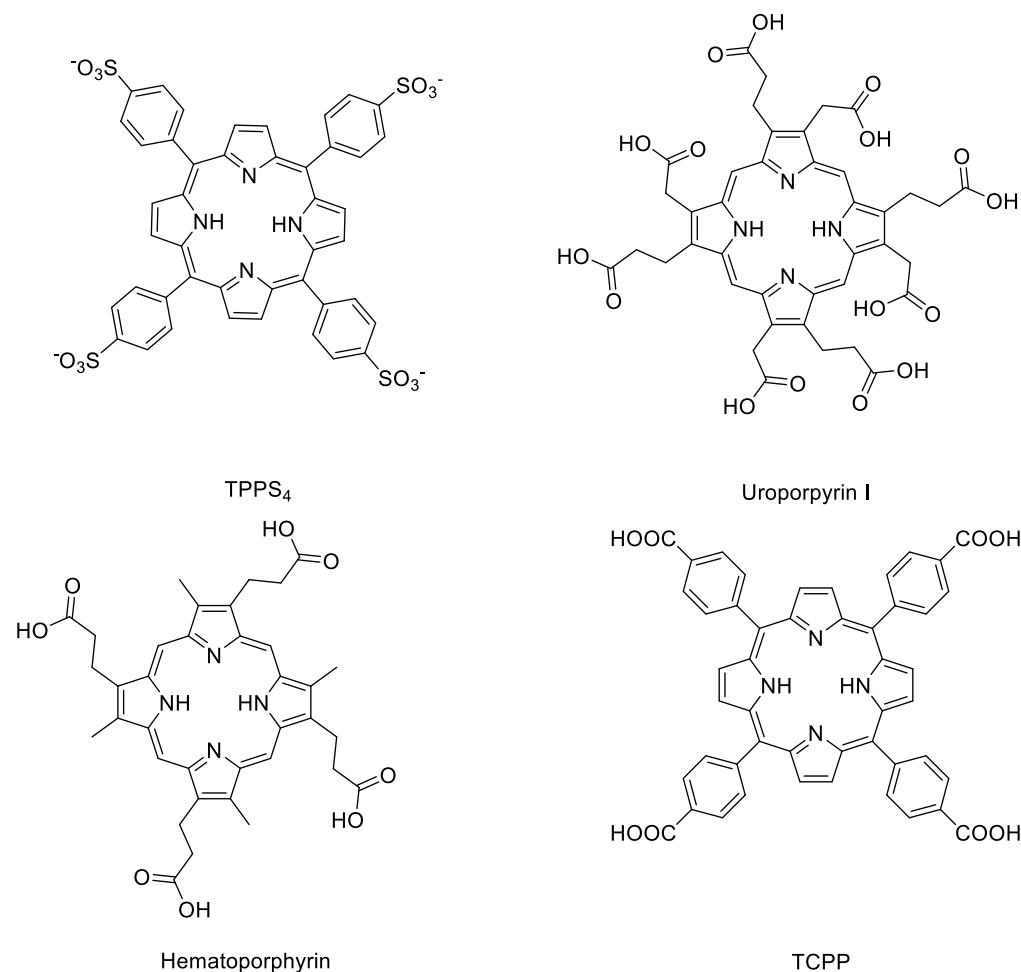
Chart 3: Few previously reported diaCEST agents based on porphyrins

NMR Validation of CEST contrast agents and *in-vitro* studies on NMR spectrometers

The basic components as well as the working principles of NMR and MRI are very similar. Structurally, both an NMR spectrometer and an MRI scanner contain a static magnetic field, an

RF coil, and a gradient coil (inside a probe) that are primarily necessary for imaging. The main magnet produces a static magnetic field that is used to align the spins to produce bulk magnetization. The RF perturbation is applied in order to tip the bulk magnetization from the equilibrium position and initiate Larmor precession. Finally, the response received is Fourier transformed to produce either a spectrum in case of NMR, or an image in case of MRI. In an NMR spectrometer gradient coils (known as shim coils) are generally used to remove spatial inhomogeneity of the magnetic field unless specially designed another gradient coil is used to produce controlled inhomogeneity. As a result the spatial information is not obtained without the special gradient coils. In case of MRI the gradients are placed parallel to the patients body and therefore protons residing in different body parts obtain slightly different resonance Larmor frequency, thereby providing spatial information. In case of NMR, similar spatial information is obtained when the sample is placed inside an NMR tube and experiments are conducted with gradient coils.

Due to this compatibility of NMR and MRI machines, any method development or *in-vitro* study based on MRI is often carried out on NMR spectrometers because of a higher availability of NMR systems compared to the MRI systems within the scientific community. In the present thesis also all development works were carried out on an NMR spectrometer.

It is therefore apt to discuss next the basic 'common' principle of NMR spectroscopy and MRI.

5. Basic principle of magnetic resonance spectroscopy

Nuclear Magnetic Resonance (NMR) spectroscopy is a non-invasive analytical tool to study the structure and dynamics of small (*viz.* organic molecules) as well as large molecules (*viz.* carbohydrates, proteins, and nucleic acids). It can also be used for kinetic studies to understand

several chemical and physical phenomena at the molecular level. The ability to design broad range of experiments (pulse programs) using different combinations of RF pulses and delays makes NMR a powerful technique that can yield a various types of information like angles and distances between atoms, coupling constants for adjacent nucleus as well as the overall chemical environment of the atoms inside a molecule.

Spin is an intrinsic property of elementary particles similar to other intrinsic properties such as, electrical charge or mass. Spins can be integral, half-integral or zero. Individual unpaired electrons, protons and neutrons possess a spin ½ each.

Nuclei with odd mass numbers posses half integral values of spin angular momentum (*I*), and those with even mass numbers have either zero (even atomic no.) or integral (odd atomic no.) values of *I*. Nuclei with non-zero spin angular momentum are NMR active.

The spin angular momentum, ***I***, is quantized (as is all angular momenta in the quantum world). The magnitude of the spin angular momentum is given as,

$$|\boldsymbol{I}| = \frac{h}{2\pi}\sqrt{I(I+1)} \tag{9},$$

Where, *I* corresponds to the nuclear spin angular momentum quantum number and $\hbar = h/2\pi$ (*h* is the Planck's constant). According to quantum mechanics, at any given time the magnitude of only one of the Cartesian components of ***I*** along with the magnitude can be determined. By convention, the *z*-component is specified as follows,

$$I_z = hm/2\pi \tag{10},$$

Where, m is the magnetic quantum number that can take values $m = \{-I, -I + 1, ..., 0, 1, ... I - 1, I\}$. The quantum states corresponding to these $2I + 1$ values of I_z are degenerate in the absence of an external field.

Nuclei with a non-zero spin angular momentum possess a nuclear magnetic moment $\boldsymbol{\mu}$, which is collinear with $\boldsymbol{I}$, Thus, $\boldsymbol{\mu}$ is given as:

$$\boldsymbol{\mu} = \gamma \boldsymbol{I} \tag{11},$$

and its z component is given by

$$\mu_z = \gamma I_z = \gamma h m / 2\pi \tag{12},$$

where, the gyromagnetic ratio, γ, is a characteristic constant for a given nucleus.

In the presence of an external magnetic field the nuclear spins having different values of m, lose their degeneracy as they try to align along or against the direction of the applied field. They cannot align exactly with the field but remain at an angle allowed by the theory of quantum mechanics. Since the spins experience a torque, they precess about the magnetic field. The torque (τ) experienced by the nuclear spin is given by:

$$\boldsymbol{\tau} = \boldsymbol{\mu} \times \boldsymbol{B} = \frac{d\boldsymbol{I}}{dt} \tag{13}.$$

Under the application of an external magnetic field, the spin states are no longer degenerate and possess energies given by:

$$E = -\boldsymbol{\mu} \cdot \boldsymbol{B} \tag{14},$$

Where, $\boldsymbol{B}$ is the magnetic field vector. For a constant magnetic field B_0, applied along the z direction, the above equation simplifies to:

$$E_m = -\gamma I_z B_0 = -m\,h\,\gamma B_0 / 2\pi \qquad (15).$$
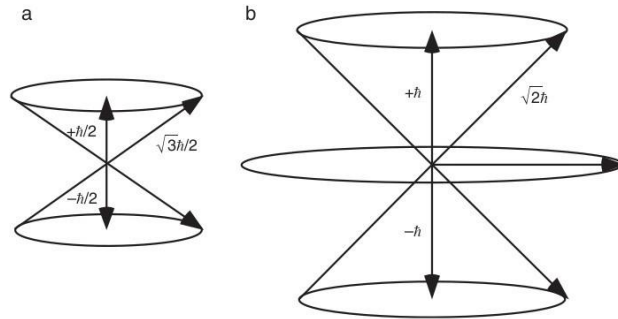
Figure 6: Nuclear Zeeman levels for (a) $I = 1/2$ and (b) $I = 1$

In the presence of an external magnetic field, the $2I + 1$ degenerate state are split into equally spaced Zeeman levels as depicted in figure 6. For $I = 1/2$, the ground or the lower energy state is referred to as α, corresponding to $m = +1/2$, and the excited or the higher energy state is referred to as β, corresponding to $m = -1/2$. The energies of the two states can be calculated from Eq. (15) as follows:

$$E_\alpha = \frac{-\gamma h B_0}{4\pi} \qquad (16),$$

and

$$E_\beta = \frac{+\gamma h B_0}{4\pi} \qquad (17).$$

The energy difference between the two states is easily computed as:

$$\Delta E = E_\beta - E_\alpha = \gamma h B_0 / 2\pi \qquad (18),$$

and using the relationship $E = \hbar\omega$ the above equation leads the well-known Larmor equation:

$$\omega_0 = -\gamma\,B_0 \qquad (19).$$

The population difference between the two Zeeman energy levels is very small, on the order of 1 part in 10^6. The actual population difference can be calculated from Boltzmann's relationship:

$$\frac{N_\beta}{N_\alpha} = e^{\frac{-\gamma h B_0}{2\pi k_B T}} \simeq 1 - \frac{\gamma h B_0}{2\pi k_B T}$$

(20),

Where, N_β and N_α refers to, respectively, the populations of the β and α states, k_B is the Boltzmann constant and T corresponds to the absolute temperature.

Between the two Zeeman states of a magnetic dipole, the α state possesses higher population compared to the other state (β) as the α state is energetically favorable. A transition between these two states can be achieved by a relatively small magnitude oscillating magnetic field, applied perpendicular to the static magnetic field B_0. If the frequency of oscillation of the smaller magnetic field satisfies the resonance or near-resonance condition w.r.t the Larmor frequency of the spins, then this field can induce a transition between the two states. The frequency of the transition inducing oscillating magnetic field generally lies in the radiofrequency region of the electromagnetic spectrum. The number of transitions between α and β states per unit time in either direction can be derived through multiplying the initial populations of the states by a transition probability given by Rabi's formula. The probability of transition in either direction is always same. If two energy levels have same initial population then the number of transitions per unit time in either direction will be the same, maintaining the equal population scenario. Such an equal population scenario is known as "saturation" in NMR or MRI terms.

At thermal equilibrium, larger population in lower energy state is predicted by the Boltzmann distribution. Thus, the net z-component of individual magnetic moments contributes towards the formation of bulk magnetization M, lying parallel to the external magnetic field B_0. In the realm of classical physics, the properties of the bulk magnetization can be derived from the Bloch

equations.[73] However, this classical description often fails to produce the correct results particularly for the case of coupled spins as the 'spin' itself is a quantum mechanical phenomenon. Despite this fact, the classical descriptions remain useful for the explanation of a single resonance line under the perturbation of RF pulse and the effect of the rf pulses can be well characterized by the classical description of the bulk magnetization derived from Bloch equations.

Mathematically, however, it is convenient to analyze these magnetic moment vectors in the rotating reference frame. According to the classical theory, the rate of change of angular momentum is equal to the torque applied:

$\frac{d\vec{I}}{dt} = \vec{\mu} \times \vec{B}$ as torque is given by $\vec{\tau} = \vec{\mu} \times \vec{B}$

Therefore, $\frac{d\vec{\mu}}{dt} = \vec{\mu} \times \gamma\vec{B}$ \qquad as, $\vec{\mu} = \gamma\vec{I}$ \hfill (21).

Transforming to rotating frame,

$$\frac{d\vec{\mu}}{dt} = \frac{\partial\vec{\mu}}{\partial t} + \vec{\Omega} \times \vec{\mu} \hspace{2cm} (22),$$

Where, $\frac{\partial\vec{\mu}}{\partial t}$ signifies the rate of change $\vec{\mu}$ in the rotating frame and $\vec{\Omega}$ corresponds to the frequency of rotation of the rotating reference frame, with respect to the lab frame.

Combining the above two equations, we get:

$$\frac{d\vec{\mu}}{dt} = \frac{\partial\vec{\mu}}{\partial t} + \vec{\Omega} \times \vec{\mu} = \vec{\mu} \times \gamma\vec{B}$$

$$\Rightarrow \frac{\partial\vec{\mu}}{\partial t} = \vec{\mu} \times (\gamma\vec{B} + \vec{\Omega}) \hspace{2cm} (23).$$

Thus, $\vec{\mu}$ will be static with respect to the rotating reference frame if $\dfrac{\partial \vec{\mu}}{\partial t}$ becomes equal to zero.

This condition is achieved if $(\gamma \vec{B} + \vec{\Omega})$ reduces to zero. That in turn gives

$$\vec{\Omega} = -\gamma\vec{B} = \gamma B_0(-\hat{z}) \quad \text{If } \vec{B} = B_0\hat{k}$$

leading to $\left|\vec{\Omega}\right| = \gamma B_0$ (24).

In other words, if the angular frequency of rotation of the rotating frame is same as the Larmor frequency, then the magnetic moment vector appears to be static in the rotating frame.

Transverse component of magnetization originates from the phase coherence of precessing spins. Such phase coherence remains absent at the thermal equilibrium, and the transverse component of individual spin cancels each other leading to zero transverse magnetization. Linearly polarized alternating magnetic field, at resonance, disturbs the thermal equilibrium and produces transverse component of the magnetization. The linearly polarized radiofrequency field can be thought of having two counter rotating circularly polarized magnetic field components,

$$B_{ac}(t) = \frac{B_1}{2}(\hat{i}\cos\omega_{ac}t + \hat{j}\sin\omega_{ac}t) + \frac{B_1}{2}(\hat{i}\cos\omega_{ac}t - \hat{j}\sin\omega_{ac}t)$$ (25),

where ω_{ac} represents the frequency of the RF perturbation. For a nucleus having a positive gyromagnetic ratio, the sense of rotation of the magnetization is anti-clockwise. This is the same direction as the rotation of the first component and hence only this component interacts with the magnetization.

Considering the static magnetic field along with the small RF perturbation, the motion of the magnetization in lab frame can be written as:

$$\frac{d\vec{\mu}}{dt} = \vec{\mu} \times \gamma (B_0 \hat{k} + \frac{B_1}{2} \cos\omega_{ac} t \, \hat{i} + \frac{B_1}{2} \sin\omega_{ac} t \, \hat{j}) \qquad (26).$$

Transforming to rotating reference frame, (where x axis of the rotating frame coincides with the rotating magnetic field) without any loss of generality the above equation becomes

$$\frac{\delta\vec{\mu}}{\delta t} = \vec{\mu} \times \gamma [(B_0 + \frac{\omega_{ac}}{\gamma}) \hat{k} + B_1 \hat{i}]$$

$$\Rightarrow \vec{\mu} \times \gamma \vec{B}_{eff} \qquad (27),$$

where the effective magnetic field in the rotating frame is represented by,

$$B_{eff} = (B_0 + \frac{\omega_{ac}}{\gamma}) \hat{k} + B_1 \hat{i} \qquad (28).$$

In resonance condition, ω_{ac} becomes equal to ω_0. Thus, the effective field reduces to B_1. In this scenario $\vec{\mu}$ precesses about B_1 with a precession rate ω_1 given by,

$$\omega_1 = \gamma B_{eff} = \gamma B_1 \qquad (29).$$

When the RF field is applied for a very short period, denoted by τ_p, the flip angle executed by the magnetization, β, is given by:

$$\beta = \gamma B_1 \tau_p \qquad (30).$$

For nuclei with a positive γ, radiofrequency field having a component along the x-axis of the rotating frame turns the bulk magnetization towards the negative y-axis. Similarly, when the B_1 field lies along the y-axis it tilts the bulk magnetization along the positive x-axis.[74] When the RF

field has a frequency component apart from ν_0, it shows a non-ideal behavior and is termed as the off-resonance effect.

The effect of the non-resonant field, given by the second part of eqn. 25, was calculated by Bloch and Siegert[75] and it was found that the frequency of the observed resonance line is shifted by a tiny amount, given by, $\nu_B = (\gamma B_1)^2 / 4\pi^2 \Delta\nu$, where $\Delta\nu$ is measured as twice the resonance frequency. This shift is immediately removed after the RF pulse is switched off. Similar to the Bloch-Siegert shift another effect takes place whenever an RF excitation pulse having a frequency $\Delta\nu$ off-resonance for the nuclear spins is applied. In order to separate from the effect produced by the counter-rotating field, it is termed as 'non-resonant effect'.[76] As this effect can be substantial and almost same as the resonance frequency, it is generally compensated by adequate means.[76]

Although the vector model, based upon the Bloch equations, provides a satisfactory explanation for single pulse NMR experiments, the elucidation of magnetization pathways during a multi-pulse NMR experiment using the concept of bulk magnetization shows profound constraints. On the other hand, the quantum mechanical calculations using density matrix that estimate the evolution of the states of a system with time and maps the probable magnetization pathway followed by a perturbation of an appropriate Hamiltonian, are accurate but tiresome. According to the quantum mechanical approach, a coherent superposition of Eigen states, whose magnetic quantum number differs by one unit, is created after the application of a radio frequency pulse. There also exist complicated pulse sequences where coherence is created between states for which the value of magnetic quantum number deviates from one. Although only the in-phase single quantum coherence is observed, such multiple quantum coherences can exist, and the information is relayed to an observable magnetization during the course of acquisition.

In order to understand a full quantum mechanical picture of the spin ½ nuclei, product operator formalism was introduced.[77] The formalism assumes that spins are not relaxing and that the resonance frequency is considerably higher compared to scalar coupling present among spins. This condition is referred to as a weak spin-spin coupling limit. With these assumptions, the transformation of the density operator can be calculated while experiencing perturbation from the chemical shift or scalar coupling Hamiltonian and under the application of the RF field. This formalism is a combination of quantum mechanical treatment and comparative classical understanding and forms the foundation of many NMR experiments. However, in the present thesis POF is not discussed in detailed as CEST experiments are rather simple two pulse (only one excitation pulse among those two) experiments and are easy to follow even without POF.

5.1 Relaxation

The return of the spins from a non-equilibrium state back to the equilibrium is termed as relaxation. This happens simultaneously through population re-distribution and through the decay of coherences (decoherence). The first one is termed as longitudinal relaxation while the other is referred to as transverse relaxation.

5.1.1 Longitudinal relaxation: Relaxation processes are responsible for bringing back the spins to the equilibrium following the application of a RF perturbation. After the RF field is switched off, the non-equilibrium spin states return to equilibrium by dissipating the extra energy to the surrounding, termed as the lattice. In general, the return of the z-component of the bulk magnetization to equilibrium follows an exponential pathway (provided more complex pathways such as cross-correlation is ignored) and the time required for complete recovery is approximately three to five times the longitudinal relaxation time constant or T_1. Microscopically some oscillating magnetic field is responsible for relaxation. Fluctuating dipolar interaction, produced by the

dynamic molecular motion, or anisotropy of electronic cloud (known as CSA or chemical shift anisotropy) around a nucleus produces that oscillating magnetic field. It should also be pointed out that only the x and y components of the oscillating local filed can influence the longitudinal relaxation. The degree of overlap between the resonance frequency and the motional frequency accounts for the contribution of the dipolar interaction and CSA towards relaxation. This overlap is given by the Spectral density function $J(\omega)$[78] . As $J(\omega)$ represents Fourier transformation of the motional correlational function, the mechanism behind the motion is highly influential in determining its functional form. As the fluctuating field that is responsible for spin-lattice relaxation is dependent upon the extent of thermal agitation, T_1 also becomes temperature dependent.

The time taken by a molecule to rotate in solution approximately 1 radian is termed as rotational correlational time. Only the rotational component of the molecular motion contributes towards relaxation as the frequency spectrum of this kind of molecular motion lies close to the resonance Larmor frequency. The rotational correlation time (τ_c) of a molecule becomes long in high viscosity solvents as well as in solids, and thus, overlap of motional frequency component and the resonance frequency drops. This results in a longer T_1 relaxation time. On the other hand, in case of very rapid tumbling motion, for the short τ_c, the spectral density does not possess much intensity at the resonance frequency thus making T_1 longer again. In the case of an intermediate situation where the condition $1/\tau_c \approx \omega_0$ holds true, the T_1 relaxation time becomes minimum.

The T_1 relaxation rate is also impacted by other factors. For a system having paramagnetic metal center, the presence of any unpaired electron makes the relaxation time much shorter due to the fluctuating field created by the spin flip of the electrons. The longitudinal relaxation time is pivotal

in optimizing the inter-pulse delay in any pulse sequence. Conventionally, the spin-lattice relaxation time or T_1 is measured via the inversion recovery method. In this method, at first an 180^0_x pulse tilts the equilibrium magnetization from +z axis to -z axis resulting in the formation of a non-equilibrium condition having no transverse component. After some delay (τ) a read-out 90^0_x pulse is applied to monitor the amount of z-magnetization recovered during the delay.

Quantitatively the exponential recovery of the magnetization towards equilibrium is characterized by the Bloch equation, and is given by:

$$\frac{dM_z}{dt} = \frac{M_0 - M_z}{T_1}$$

(31).

Integration of this equation with $M_z = -M_0$ at t=0 produces

$$M_z(t) = M_0[1 - 2\exp(-t/T_1)]$$

(32).

From the above equation the null point can be calculated where the intensity of the spectrum after the readout pulse becomes zero and from that null point the spin-lattice relaxation time can be roughly estimated. Alternatively for more precise determination, the equation can be fitted with a data of $M_Z(t)$ vs. t

5.1.2 Transverse relaxation: The process by which the magnetization components in the transverse plane decay is termed as spin-spin relaxation. After an RF perturbation, the newly generated coherent superposition between Zeeman states is gradually lost either due to direct interactions of the spins with the surrounding spins without any participation of the lattice or because of the field in-homogeneities. There are two components contributing to the transverse relaxation. The secular contribution comes from the variation of z component of the local field. As the local field is different for different spins inside the ensemble owing to their different chemical

environment, the free precession gradually losses the coherence state leading to a decay of the transverse magnetization. On the contrary, the non-secular contribution towards spin-spin relaxation is brought by the x and y components of the local field, oscillating close or near to the Larmor frequency and thus acting like a random low intensity electromagnetic radiation. Transverse relaxation depends also upon J(0), the spectral density at zero frequency, as the z component of the stochastic local magnetic field is instrumental in reducing the coherence of the transverse component of magnetization. However, two different molecules with equal molecular weight might show diverse relaxation pattern based on their different internal modes of molecular motion.

T_2 is related to the linewidth at half height of a lorentzian NMR peak in the frequency domain. As the dipolar mechanism, which is responsible for the creation of local field, is strong in case of solid compared to liquids the T_2 is relatively longer in case of liquids and very short in case of solids. This result in a broader NMR signals for solids compared to the liquids.

Transverse relaxation rate can be measured using a simple spin-echo pulse sequence. However, as the width of an NMR peak depends on both the spin-spin relaxation as well as field in-homogeneities, an improved CPMG pulse sequence is therefore employed that removes the contribution of field in-homogeneities from the signal decay. Bloch equation is used to quantitatively determine the spin-spin relaxation time.

According to Bloch equation:

$$\frac{dM_{x(y)}}{dt} = -\frac{M_{x(y)}}{T_2}$$

(33),

which upon integration gives $M_{x(y)} = M_0[exp(\text{-}t \, / \, T_2)]$, with the initial condition $M_{x(y)}(\infty) = 0$ and

$M_{x(y)}(0) = M_0$.

Fitting the above expression for $M_{x(y)}$ to the measured decay of a NMR peak as a function of the total decay time provides the value of spin-spin (T_2) relaxation time constant.

5.2 Radio-frequency Pulses:

An NMR pulse sequence is composed of several RF pulses and delays followed by the measurement of EMF induced in the RF coil by the Larmor precession of the bulk magnetization. A delay signifies a duration during which no RF perturbation is applied, and the corresponding spin state evolves under the influence of chemical shift, coupling (if any) and relaxation Hamiltonians. The duration during which a single RF perturbation is applied by the probe to the sample is termed as the pulse length. The four characteristics variables of a pulse are amplitude (power level), length, phase, and frequency. The frequency of an RF pulse is referred to as the carrier frequency. The amplitude of the RF field remains constant during the application of a rectangular pulse. The RF field strength is adjusted by the relationship among the flip angle (β), the pulse length (τ_p), and the field strength and is given by the equation:

$$\beta = \gamma B_1 \tau_p \tag{34}$$

For example, in case of a proton experiment, the field strength of a 15μs pulse resulting in a flip angle of 90^0 is amounted to be 390.83μT which is equivalent to 16.8 KHz. It is worthwhile to mention that "shape" of a pulse is also an important aspect of pulses, which will be discussed later in chapter five.

Upon the application of an RF perturbation all the spin vectors of a given nucleus type are expected to tilt exactly by the same angle ß about the axis defined by the pulse phase, irrespective of the resonance frequencies. The performance of the RF pulse, however, starts deviating from the ideal behavior as the resonance frequencies mismatch with the carrier frequency of the RF excitation. Although for a 90^0 pulse the excitation field remains constant for a large bandwidth, the performance of an 180^0 pulse deteriorates rather quickly. The best result is obtained when the carrier frequency is placed at the center of the desired bandwidth of excitation. As long as the offset frequency of a particular spin satisfies the criteria that the offset frequency ν_{off} is less than γB_1 ($\nu_{off} < \gamma B_1 / 2\pi$), application of a 90^0 pulse to z magnetization flips all the magnetization into the x-y plane nearly identically. However, to be very precise, the flipped magnetization makes an offset dependent angle with the desired direction it is supposed to point after an ideal 90^0 pulse.[78]

The non-ideal behavior of RF perturbation is positively exploited in selective excitation of spins where the RF pulse selectively excites a small set of frequencies. For a 90^0 rectangular pulse having pulse length τ_{90}, the mth null of the excitation profile at a frequency ν_{90} from the carrier frequency can be explicitly derived using the Bloch equation.

The equation describing the null point is given by

$$\nu_{90}(m) = \frac{\pm\sqrt{m^2 - 1/16}}{\tau_{90}} \tag{35}.$$

From this equation it can be derived that the first null for a 90^0 pulse is at $\nu_{90} = \pm 0.97 / \tau_{90}$.

Similarly the equation that derives the mth null of the excitation profile at a frequency ν_{180} from the carrier frequency for a 180^0 pulse having a pulse length τ_{180} is represented by,

$$\nu_{180}(m) = \frac{\pm\sqrt{m^2 - 1/4}}{\tau_{180}}$$ (36),

and accordingly, the first null for a 180^0 pulse is found to be at $\nu_{180} = \pm 0.87 / \tau_{180}$.

Excitation of a specific range of frequencies without exciting other frequencies can be obtained by tuning the amplitude of a shaped pulse. As the excitation profile of a shaped pulse cannot be derived directly from Fourier transformation due to their non-linear behavior,[78] a further intricate calculation must be in place to obtain the optimized pulse shape for a desired bandwidth of excitation. Accordingly, a wide range of shaped pulse has been characterized and developed. Integration of the Bloch equation is analyzed to obtain the excitation profile of a pulse shape. Bloch simulator is used in almost all commercial spectrometers to analyze the bandwidth of excitation and tune the parameters of a particular shape[79] profile to get the desired excitation bandwidth. The characteristic features of a good amplitude-modulated pulse include short pulse length, good frequency selectivity, uniform phase and uniform excitation amplitude across the bandwidth of excitation. Not all the features of a given pulse can be bettered at the same time though. For example, to gain a better selectivity the duration of a shaped pulse should be increased as these two are inversely related. The relationship is governed by the equation $\Delta\nu = F / \Delta\tau$, where, $\Delta\nu$ and $\Delta\tau$ correspond to the bandwidth of excitation and pulse length, respectively and F designates the bandwidth factor for the particular shape in use. However, the increasing pulse length brings in relaxation losses. Apart from that, an offset dependent phase error is picked up by the magnetization component when a shaped RF pulse is applied. Application of a hard 180^0 pulse, followed by the selective pulse, is generally used to refocus the linear phase errors.[citation]

Initial state of the magnetization also plays a significant role in the efficiency of amplitude-modulated pulses. A particular shaped pulse, which is efficient in inverting the Z magnetization, might not be as accurate in refocusing the transverse component of the magnetization and vice versa. The necessary requirement for obtaining a better efficiency of the amplitude modulated pulse is the linear behavior of the transmitter pathway of the spectrometer. Besides that, the amplitude modulated pulses are also sensitive towards RF in-homogeneities of the probe.

5.3 Signal Digitization

After the application of an RF pulse, the free induction decay of the observable transverse magnetization is measured, while considering the fact that the detection sensitivity is proportional to the gyromagnetic ratio of the nucleus. Although the difference in chemical shift of the nuclei under consideration lies in the range of few kilohertz, the resonance frequency is in hundreds of megahertz. RF signals lying in the range of zero to plus or minus few kilohertz is obtained when the carrier frequency is subtracted from the individual signal coming out of the nuclei. As digitizers are available for conversion of analog signal to digital signal with dynamic range only up to few kilohertz, frequency mixing methods are used by the spectrometer to convert higher resonance frequencies to lower frequency. In addition, the quadrature detection process produces two signals phase-shifted from each other by 90^0. As a result, the signals that are higher or lower than the carrier frequency are easily discriminated. The analog signals, having low frequency, are digitized at a regular interval, and stored in the computer.

According to the sampling theorem, to digitize an analog signal reliably, the sampling rate must be at least twice the highest frequency component present in the signal that is going to be digitized. In technical terminology the inverse of the sweep width 2ν (when the frequency lies between the range of $+\nu$ to $-\nu$) must be higher than or equal to the dwell time, that is, the interval between two

successive points in the time domain data. With the quadrature detection in place, the highest frequency in the spectrum is reduced to half the spectral width. If the sampling rate is slower than that required, then folding of signals at an erroneous frequency and phase difference with respect to their unfolded counterparts will occur.

5.4 Data Processing

The preccesing of magnetization in the transverse plane induces EMF in the RF coil, which can be expressed as

$$S(x) = S(0) \cos \Omega t \quad \text{And} \, S(y) = S(0) \sin \Omega t \tag{37}.$$

Where, $S(x)$ and $S(y)$ refers to the x and y component of magnetization after time t and $S(0)$ is the initial magnetization.

Considering the transverse relaxation is in place, the transverse magnetization is represented by

$$S(x) = S(0) \cos \Omega t \exp(\text{-}t / T_2) \text{ and } S(y) = S(0) \sin \Omega t \exp(\text{-}t / T_2) \tag{38}.$$

Considering a 90^0 phase shift between the x and y component of transverse magnetization, the resultant analytical expression for the precessing magnetization reduces to

$$S(t) = S_x + iS_y = S(0) \, (\cos \Omega t + i \sin \Omega t) \, \exp(\text{-}t / T_2)$$

$$S(t) = S(0) \exp(i \Omega t) \, \exp(\text{-}t / T_2) \tag{39}.$$

This analytical expression leads to the understanding that while precessing in the xy plane the transverse magnetization also decays with time due to the presence of the damping factor. If the spin-spin relaxation rate constant is denoted by R_2 in units of s^{-1} or Hz then the equation (39) takes the form:

$$S(t) = S(0) \exp(i\Omega t) \, \exp(-Rt) \qquad\qquad (40).$$

Fourier transformation of the complex FID S(t) is as follows:

$$S(\omega) = \int\limits_{0}^{\infty} S(t) e^{-i\omega t} dt = \int\limits_{0}^{\infty} S(0) \exp(i\Omega t) \, \exp(-R_2 t) e^{-i\omega t} dt \qquad\qquad (41),$$

$$\text{or } S(\omega) = \int\limits_{0}^{\infty} S_0 e^{[-i(\omega-\Omega)-R_2]t} dt \qquad\qquad (42).$$

Upon integration equation (42) leads to

$$S(\omega) = \frac{S_0 R}{(\omega-\Omega)^2 + R_2{}^2} + i \frac{-S_0(\omega-\Omega)}{(\omega-\Omega)^2 + R_2{}^2} \qquad\qquad (43).$$

The real part is termed as absorption mode or absorptive Lorentzian line shape whereas the imaginary part is referred to as dispersion mode or dispersive Lorentzian line shape. Absorptive line shapes are preferred because of their narrow linewidth and hence they are capable of producing a better-resolved spectrum. Hilbert transformation is used to segregate the real and imaginary parts from each other. Zero filling is the process of adding zero at the end of the FID to smooth the spectrum lines without any additional information. This is to diminish truncation error that are responsible for producing wiggles close to the signal, zero filled FID's should be multiplied by a proper weighing function that becomes zero when the FID ends and before the zeros start. Non-linear algorithm-based transformation methods are also available, but they are not frequently used for CEST processing as the result is significantly dependent on the settings of the appropriate parameter.

Scope and organization of the present thesis   In this thesis work we have shown that either by altering the electronic structure of certain molecules or by systematically tuning the NMR

experimental parameters, the CEST efficiency of diaCEST agents can be enhanced. In a different vein, we have also introduced CEST as a possible analytical tool to estimate the average power delivery associated with any shaped pulse. The details of the chapters are as follows:

In chapter 2, different components of a nuclear magnetic resonance spectrometer have been briefly discussed. All the experimental techniques involved in preparation of CEST spectra, exchange rate calculation, relaxivity measurements, diffusion measurements have been discussed with brief theoretical background.

In chapter 3, We show tetrakis-(*N*-methyl-4-pyridinium)-porphyrin (TmPyP) as a potential diaCEST MRI contrast agent that shows an appreciable 15% CEST effect at physiological condition both in buffer as well as biological media. Further it maintains a nearly constant contrast efficiency (average 18%) in the pH range of 6.6 to 8.3 in which different human body fluids are naturally found.

In chapter 4, We introduce a few amide (acetanilide, in particular) derivatives as a new class of diaCEST agents that utilizes intermolecular hydrogen bond (interMHB) and produces appreciable CEST contrast despite the fact that they do not show a large chemical shift. The interMHB helps to bring the exchange rate down to a favorable slow to medium exchange regime. In other words, the molecules act as a CEST contrast agent only as a group. We show this interesting behavior through a number of variable temperature experiments.

In chapter 5, We demonstrate the effect of pulse shapes on enhancement of CEST efficiency. A synergy between the experimental NMR parameters as well as electronic properties of a molecule is highly advocated in order to successfully screen or develop saturation transfer based contrast agents. We present our investigation of the effect of each individual component of the saturation

transfer experiments including pulse length, saturation duration, relaxation delay, and pulse shape. In the second part of the chapter we discuss a new role of CEST as a quick analytical tool to measure the average power associated with any newly defined pulse shape.

Reference:

1.   Damadian, R., Tumor Detection by Nuclear Magnetic Resonance. *Science* **1971,** *171* (3976), 1151.

2.   Lauterbur, P. C., Image Formation by Induced Local Interactions: Examples Employing Nuclear Magnetic Resonance. *Nature* **1973,** *242* (5394), 190-191.

3.   Lauterbur, P. C., Magnetic resonance zeugmatography. *Pure and Applied Chemistry* **1974,** *40* (1-2), 149-157.

4.   Mansfield, P., Multi-planar image formation using NMR spin echoes. *Journal of Physics C: Solid State Physics* **1977,** *10* (3), L55-L58.

5.   Kumar, A.; Welti, D.; Ernst, R. R., NMR Fourier zeugmatography. *Journal of Magnetic Resonance (1969)* **1975,** *18* (1), 69-83.

6.   Poustchi-Amin, M.; Mirowitz, S. A.; Brown, J. J.; McKinstry, R. C.; Li, T., Principles and Applications of Echo-planar Imaging: A Review for the General Radiologist. *RadioGraphics* **2001,** *21* (3), 767-779.

7.   Relaxivity of Gadolinium(III) Complexes: Theory and Mechanism. In *The Chemistry of Contrast Agents in Medical Magnetic Resonance Imaging*, 2013; pp 25-81.

8.   Aime, S.; Botta, M.; Fasano, M.; Terreno, E., Lanthanide(III) chelates for NMR biomedical applications. *Chemical Society Reviews* **1998,** *27* (1), 19-29.

9.   Carrier, D. A.; Ford, J. J.; Hayman, L. A., MR appearance of extravasated gadolinium contrast medium. *American Journal of Neuroradiology* **1993,** *14* (2), 363.

10.   Caravan, P.; Ellison, J. J.; McMurry, T. J.; Lauffer, R. B., Gadolinium(III) Chelates as MRI Contrast Agents: Structure, Dynamics, and Applications. *Chemical reviews* **1999,** *99* (9), 2293-352.

11.   Schmitt-Willich, H., Stability of linear and macrocyclic gadolinium based contrast agents. *The British journal of radiology* **2007,** *80* (955), 581-2; author reply 584-5.

12.   Wedeking, P.; Kumar, K.; Tweedle, M. F., Dissociation of gadolinium chelates in mice: Relationship to chemical characteristics. *Magnetic Resonance Imaging* **1992,** *10* (4), 641-648.

13.   Raymond, K. N.; Pierre, V. C., Next generation, high relaxivity gadolinium MRI agents. *Bioconjugate chemistry* **2005,** *16* (1), 3-8.

14.   Caravan, P.; Ellison, J. J.; McMurry, T. J.; Lauffer, R. B., Gadolinium(III) Chelates as MRI Contrast Agents: Structure, Dynamics, and Applications. *Chemical reviews* **1999,** *99* (9), 2293-2352.

15.   Lauffer, R. B., Paramagnetic metal complexes as water proton relaxation agents for NMR imaging: theory and design. *Chemical reviews* **1987,** *87* (5), 901-927.

16.   Carr, D. H.; Brown, J.; Bydder, G. M.; Steiner, R. E.; Weinmann, H. J.; Speck, U.; Hall, A. S.; Young, I. R., Gadolinium-DTPA as a contrast agent in MRI: initial clinical experience in 20 patients. *American Journal of Roentgenology* **1984,** *143* (2), 215-224.

17.   Carter, J. W., MRI: The Basics, 3rd ed. *American Journal of Roentgenology* **2011,** *197* (2), W361-W361.

18.   Brady, T. J.; Goldman, M. R.; Pykett, I. L.; Buonanno, F. S.; Kistler, J. P.; Newhouse, J. H.; Burt, C. T.; Hinshaw, W. S.; Pohost, G. M., Proton nuclear magnetic resonance imaging of regionally ischemic canine hearts: effect of paramagnetic proton signal enhancement. *Radiology* **1982,** *144* (2), 343-7.

19.   Goldman, M. R.; Brady, T. J.; Pykett, I. L.; Burt, C. T.; Buonanno, F. S.; Kistler, J. P.; Newhouse, J. H.; Hinshaw, W. S.; Pohost, G. M., Quantification of experimental myocardial infarction using nuclear magnetic resonance imaging and paramagnetic ion contrast enhancement in excised canine hearts. *Circulation* **1982,** *66* (5), 1012-1016.

20.   Zhu, S.; Das, A.; Bui, L.; Zhou, H.; Curran, D. P.; Rueping, M., Oxygen Switch in Visible-Light Photoredox Catalysis: Radical Additions and Cyclizations and Unexpected C–C-Bond Cleavage Reactions. *J. Am. Chem. Soc.* **2013,** *135* (5), 1823-1829.

21.   Soesbe, T. C.; Merritt, M. E.; Green, K. N.; Rojas-Quijano, F. A.; Sherry, A. D., T2 exchange agents: a new class of paramagnetic MRI contrast agent that shortens water T2 by chemical exchange rather than relaxation. *Magnetic resonance in medicine* **2011,** *66* (6), 1697-703.

22.   Woods, M.; Woessner, D. E.; Sherry, A. D., Paramagnetic lanthanide complexes as PARACEST agents for medical imaging. *Chemical Society Reviews* **2006,** *35* (6), 500-511.

23.   van Zijl, P. C.; Yadav, N. N., Chemical exchange saturation transfer (CEST): what is in a name and what isn't? *Magnetic resonance in medicine* **2011,** *65* (4), 927-48.

24.   Dorazio, S. J.; Olatunde, A. O.; Tsitovich, P. B.; Morrow, J. R., Comparison of divalent transition metal ion paraCEST MRI contrast agents. *Journal of biological inorganic chemistry : JBIC : a publication of the Society of Biological Inorganic Chemistry* **2014,** *19* (2), 191-205.

25.   Caravan, P., Strategies for increasing the sensitivity of gadolinium based MRI contrast agents. *Chemical Society Reviews* **2006,** *35* (6), 512-523.

26.   Gutierrez, J. E.; Rosenberg, M.; Seemann, J.; Breuer, J.; Haverstock, D.; Agris, J.; Balzer, T.; Anzalone, N., Safety and Efficacy of Gadobutrol for Contrast-enhanced Magnetic Resonance Imaging of the Central Nervous System: Results from a Multicenter, Double-blind, Randomized, Comparator Study. *Magn Reson Insights* **2015,** *8*, 1-10.

27.   Van Wagoner, M.; Worah, D., Gadodiamide injection. First human experience with the nonionic magnetic resonance imaging enhancement agent. *Investigative radiology* **1993,** *28 Suppl 1*, S44-8.

28.   Kanal, E.; Broome, D. R.; Martin, D. R.; Thomsen, H. S., Response to the FDA's May 23, 2007, nephrogenic systemic fibrosis update. *Radiology* **2008,** *246* (1), 11-14.

29.   Kang, H. W.; Josephson, L.; Petrovsky, A.; Weissleder, R.; Bogdanov, A., Jr., Magnetic resonance imaging of inducible E-selectin expression in human endothelial cell culture. *Bioconjugate chemistry* **2002,** *13* (1), 122-7.

30.   Milne, M.; Chicas, K.; Li, A.; Bartha, R.; Hudson, R. H. E., ParaCEST MRI contrast agents capable of derivatizationvia "click" chemistry. *Organic & Biomolecular Chemistry* **2012,** *10* (2), 287-292.

31.   Chen, Q.; Shang, W.; Zeng, C.; Wang, K.; Liang, X.; Chi, C.; Liang, X.; Yang, J.; Fang, C.; Tian, J., Theranostic imaging of liver cancer using targeted optical/MRI dual-modal probes. *Oncotarget* **2017,** *8* (20).

32.   Forsén, S.; Hoffman, R. A., Study of Moderately Rapid Chemical Exchange Reactions by Means of Nuclear Magnetic Double Resonance. *The Journal of Chemical Physics* **1963,** *39* (11), 2892-2901.

33.   Ward, K. M.; Aletras, A. H.; Balaban, R. S., A new class of contrast agents for MRI based on proton chemical exchange dependent saturation transfer (CEST). *Journal of magnetic resonance (San Diego, Calif. : 1997)* **2000,** *143* (1), 79-87.

34.   Cavanagh, J.; Fairbrother, W. J.; Palmer, A. G.; Rance, M.; Skelton, N. J., CHAPTER 5 - RELAXATION AND DYNAMIC PROCESSES. In *Protein NMR Spectroscopy (Second Edition)*, Cavanagh, J.; Fairbrother, W. J.; Palmer, A. G.; Rance, M.; Skelton, N. J., Eds. Academic Press: Burlington, 2007; pp 333-404.

35.   Pike, G. B.; Glover, G. H.; Hu, B. S.; Enzmann, D. R., Pulsed magnetization transfer spin-echo MR imaging. *Journal of magnetic resonance imaging : JMRI* **1993,** *3* (3), 531-9.

36.   Bloembergen, N.; Purcell, E. M.; Pound, R. V., Relaxation Effects in Nuclear Magnetic Resonance Absorption. *Physical Review* **1948,** *73* (7), 679-712.

37.   Kalk, A.; Berendsen, H. J. C., Proton magnetic relaxation and spin diffusion in proteins. *Journal of Magnetic Resonance (1969)* **1976,** *24* (3), 343-366.

38.   Li, A. X.; Wojciechowski, F.; Suchy, M.; Jones, C. K.; Hudson, R. H.; Menon, R. S.; Bartha, R., A sensitive PARACEST contrast agent for temperature MRI: Eu3+-DOTAM-glycine (Gly)-phenylalanine (Phe). *Magnetic resonance in medicine* **2008,** *59* (2), 374-81.

39.   Edzes, H. T.; Samulski, E. T., Cross relaxation and spin diffusion in the proton NMR or hydrated collagen. *Nature* **1977,** *265* (5594), 521-3.

40.   van Zijl, P. C.; Zhou, J.; Mori, N.; Payen, J. F.; Wilson, D.; Mori, S., Mechanism of magnetization transfer during on-resonance water saturation. A new approach to detect mobile proteins, peptides, and lipids. *Magnetic resonance in medicine* **2003,** *49* (3), 440-9.

41.   Mirau, P. A.; Bovey, F. A., The dipolar and exchange contributions to the spin-lattice relaxation of the imino protons in poly(rA)· poly(rU). *Journal of Magnetic Resonance* **1987,** *71*, 201.

42.   Henkelman, R. M.; Stanisz, G. J.; Graham, S. J., Magnetization transfer in MRI: a review. *NMR Biomed* **2001,** *14* (2), 57-64.

43.   Viswanathan, S.; Kovacs, Z.; Green, K. N.; Ratnakar, S. J.; Sherry, A. D., Alternatives to Gadolinium-Based Metal Chelates for Magnetic Resonance Imaging. *Chemical reviews* **2010,** *110* (5), 2960-3018.

44.   Li, A. X.; Hudson, R. H.; Barrett, J. W.; Jones, C. K.; Pasternak, S. H.; Bartha, R., Four-pool modeling of proton exchange processes in biological systems in the presence of MRI-paramagnetic chemical exchange saturation transfer (PARACEST) agents. *Magnetic resonance in medicine* **2008,** *60* (5), 1197-206.

45.   Wang, X.; Wu, Y.; Soesbe, T. C.; Yu, J.; Zhao, P.; Kiefer, G. E.; Sherry, A. D., A pH-Responsive MRI Agent that Can Be Activated Beyond the Tissue Magnetization Transfer Window. *Angew Chem Int Ed Engl* **2015,** *54* (30), 8662-8664.

46.   Soesbe, T. C.; Wu, Y.; Dean Sherry, A., Advantages of paramagnetic chemical exchange saturation transfer (CEST) complexes having slow to intermediate water exchange properties as responsive MRI agents. *NMR Biomed* **2013,** *26* (7), 829-38.

47.   Marckmann, P.; Skov, L.; Rossen, K.; Dupont, A.; Damholt, M. B.; Heaf, J. G.; Thomsen, H. S., Nephrogenic systemic fibrosis: suspected causative role of gadodiamide used for contrast-enhanced magnetic resonance imaging. *Journal of the American Society of Nephrology : JASN* **2006,** *17* (9), 2359-62.

48.   Zhang, S.; Winter, P.; Wu, K.; Sherry, A. D., A Novel Europium(III)-Based MRI Contrast Agent. *Journal of the American Chemical Society* **2001,** *123* (7), 1517-1518.

49.   Zhang, S.; Michaudet, L.; Burgess, S.; Sherry, A. D., The Amide Protons of an Ytterbium(III) dota Tetraamide Complex Act as Efficient Antennae for Transfer of Magnetization to Bulk Water. *Angewandte Chemie International Edition* **2002,** *41* (11), 1919-1921.

50.   Fernando, W. S.; Martins, A. F.; Zhao, P.; Wu, Y.; Kiefer, G. E.; Platas-Iglesias, C.; Sherry, A. D., Breaking the Barrier to Slow Water Exchange Rates for Optimal Magnetic Resonance Detection of paraCEST Agents. *Inorganic chemistry* **2016,** *55* (6), 3007-14.

51.   Ratnakar, S. J.; Viswanathan, S.; Kovacs, Z.; Jindal, A. K.; Green, K. N.; Sherry, A. D., Europium(III) DOTA-tetraamide complexes as redox-active MRI sensors. *J Am Chem Soc* **2012,** *134* (13), 5798-800.

52.   Song, B.; Wu, Y.; Yu, M.; Zhao, P.; Zhou, C.; Kiefer, G. E.; Sherry, A. D., A europium(iii)-based PARACEST agent for sensing singlet oxygen by MRI. *Dalton Transactions* **2013,** *42* (22), 8066-8069.

53.   Goffeney, N.; Bulte, J. W. M.; Duyn, J.; Bryant, L. H.; van Zijl, P. C. M., Sensitive NMR Detection of Cationic-Polymer-Based Gene Delivery Systems Using Saturation Transfer via Proton Exchange. *Journal of the American Chemical Society* **2001,** *123* (35), 8628-8629.

54.   Snoussi, K.; Bulte, J. W.; Guéron, M.; van Zijl, P. C., Sensitive CEST agents based on nucleic acid imino proton exchange: detection of poly(rU) and of a dendrimer-poly(rU) model for nucleic acid delivery and pharmacology. *Magnetic resonance in medicine* **2003,** *49* (6), 998-1005.

55.   Zhou, J.; Lal, B.; Wilson, D. A.; Laterra, J.; van Zijl, P. C., Amide proton transfer (APT) contrast for imaging of brain tumors. *Magnetic resonance in medicine* **2003,** *50* (6), 1120-6.

56. Zhou, J.; Payen, J. F.; Wilson, D. A.; Traystman, R. J.; van Zijl, P. C., Using the amide proton signals of intracellular proteins and peptides to detect pH effects in MRI. *Nat Med* **2003,** *9* (8), 1085-90.

57. van Zijl, P. C. M.; Jones, C. K.; Ren, J.; Malloy, C. R.; Sherry, A. D., MRI detection of glycogen in vivo by using chemical exchange saturation transfer imaging (glycoCEST). *Proceedings of the National Academy of Sciences* **2007,** *104* (11), 4359.

58. Kim, H. J.; Kim, J.; Cho, S. H.; Chang, S., Intermolecular Oxidative C–N Bond Formation under Metal-Free Conditions: Control of Chemoselectivity between Aryl sp2 and Benzylic sp3 C–H Bond Imidation. *J. Am. Chem. Soc.* **2011,** *133* (41), 16382-16385.

59. Haris, M.; Singh, A.; Cai, K.; Nath, K.; Crescenzi, R.; Kogan, F.; Hariharan, H.; Reddy, R., MICEST: A potential tool for non-invasive detection of molecular changes in Alzheimer's disease. *Journal of Neuroscience Methods* **2013,** *212* (1), 87-93.

60. Cai, K.; Haris, M.; Singh, A.; Kogan, F.; Greenberg, J. H.; Hariharan, H.; Detre, J. A.; Reddy, R., Magnetic resonance imaging of glutamate. *Nature Medicine* **2012,** *18* (2), 302-306.

61. Haris, M.; Nanga, R. P. R.; Singh, A.; Cai, K.; Kogan, F.; Hariharan, H.; Reddy, R., Exchange rates of creatine kinase metabolites: feasibility of imaging creatine by chemical exchange saturation transfer MRI. *NMR in Biomedicine* **2012,** *25* (11), 1305-1309.

62. Kogan, F.; Haris, M.; Singh, A.; Cai, K.; Debrosse, C.; Nanga, R. P. R.; Hariharan, H.; Reddy, R., Method for high-resolution imaging of creatine in vivo using chemical exchange saturation transfer. *Magnetic resonance in medicine* **2014,** *71* (1), 164-172.

63. Chan, K. W. Y.; Liu, G.; Song, X.; Kim, H.; Yu, T.; Arifin, D. R.; Gilad, A. A.; Hanes, J.; Walczak, P.; van Zijl, P. C. M.; Bulte, J. W. M.; McMahon, M. T., MRI-detectable pH nanosensors

incorporated into hydrogels for in vivo sensing of transplanted-cell viability. *Nature Materials* **2013,** *12* (3), 268-275.

64.   Ling, W.; Regatte, R. R.; Navon, G.; Jerschow, A., Assessment of glycosaminoglycan concentration in vivo by chemical exchange-dependent saturation transfer (gagCEST). *Proceedings of the National Academy of Sciences* **2008,** *105* (7), 2266.

65.   Bar-Shir, A.; Liu, G.; Liang, Y.; Yadav, N. N.; McMahon, M. T.; Walczak, P.; Nimmagadda, S.; Pomper, M. G.; Tallman, K. A.; Greenberg, M. M.; van Zijl, P. C. M.; Bulte, J. W. M.; Gilad, A. A., Transforming Thymidine into a Magnetic Resonance Imaging Probe for Monitoring Gene Expression. *Journal of the American Chemical Society* **2013,** *135* (4), 1617-1624.

66.   Longo, D. L.; Dastrù, W.; Digilio, G.; Keupp, J.; Langereis, S.; Lanzardo, S.; Prestigio, S.; Steinbach, O.; Terreno, E.; Uggeri, F.; Aime, S., Iopamidol as a responsive MRI-chemical exchange saturation transfer contrast agent for pH mapping of kidneys: In vivo studies in mice at 7 T. *Magnetic resonance in medicine* **2011,** *65* (1), 202-11.

67.   Moon, B. F.; Jones, K. M.; Chen, L. Q.; Liu, P.; Randtke, E. A.; Howison, C. M.; Pagel, M. D., A comparison of iopromide and iopamidol, two acidoCEST MRI contrast media that measure tumor extracellular pH. *Contrast media & molecular imaging* **2015,** *10* (6), 446-55.

68.   Longo, D. L.; Sun, P. Z.; Consolino, L.; Michelotti, F. C.; Uggeri, F.; Aime, S., A General MRI-CEST Ratiometric Approach for pH Imaging: Demonstration of in Vivo pH Mapping with Iobitridol. *Journal of the American Chemical Society* **2014,** *136* (41), 14333-14336.

69.   Yang, X.; Song, X.; Li, Y.; Liu, G.; Banerjee, S. R.; Pomper, M. G.; McMahon, M. T., Salicylic acid and analogues as diaCEST MRI contrast agents with highly shifted exchangeable proton frequencies. *Angew Chem Int Ed Engl* **2013,** *52* (31), 8116-8119.

70.   Yang, X.; Song, X.; Ray Banerjee, S.; Li, Y.; Byun, Y.; Liu, G.; Bhujwalla, Z. M.; Pomper, M. G.; McMahon, M. T., Developing imidazoles as CEST MRI pH sensors. *Contrast media & molecular imaging* **2016,** *11* (4), 304-12.

71.   Song, X.; Yang, X.; Ray Banerjee, S.; Pomper, M. G.; McMahon, M. T., Anthranilic acid analogs as diamagnetic CEST MRI contrast agents that feature an intramolecular-bond shifted hydrogen. *Contrast media & molecular imaging* **2015,** *10* (1), 74-80.

72.   Zhang, X.; Yuan, Y.; Li, S.; Zeng, Q.; Guo, Q.; Liu, N.; Yang, M.; Yang, Y.; Liu, M.; McMahon, M. T.; Zhou, X., Free-base porphyrins as CEST MRI contrast agents with highly upfield shifted labile protons. **2019,** *82* (2), 577-585.

73.   Bloch, F., Nuclear Induction. *Physical Review* **1946,** *70* (7-8), 460-474.

74.   Levitt, M. H., The Signs of Frequencies and Phases in NMR. *Journal of Magnetic Resonance* **1997,** *126* (2), 164-182.

75.   Bloch, F.; Siegert, A., Magnetic Resonance for Nonrotating Fields. *Physical Review* **1940,** *57* (6), 522-527.

76.   McCoy, M. A.; Mueller, L., Coherence quenching induced by frequency-selective homonuclear decoupling. *Journal of Magnetic Resonance (1969)* **1992,** *98* (3), 674-679.

77.   Sørensen, O. W.; Eich, G. W.; Levitt, M. H.; Bodenhausen, G.; Ernst, R. R., Product operator formalism for the description of NMR pulse experiments. *Progress in Nuclear Magnetic Resonance Spectroscopy* **1984,** *16*, 163-192.

78.   Cavanagh, J.; Fairbrother, W. J.; Palmer, A. G.; Rance, M.; Skelton, N. J., CHAPTER 3 - EXPERIMENTAL ASPECTS OF NMR SPECTROSCOPY. In *Protein NMR Spectroscopy (Second Edition)*, Cavanagh, J.; Fairbrother, W. J.; Palmer, A. G.; Rance, M.; Skelton, N. J., Eds. Academic Press: Burlington, 2007; pp 114-270.

79.   Kessler, H.; Oschkinat, H.; Griesinger, C.; Bermel, W., Transformation of homonuclear two-dimensional NMR techniques into one-dimensional techniques using Gaussian pulses. *Journal of Magnetic Resonance (1969)* **1986,** *70* (1), 106-133.

CHAPTER 2

Instrumentation and Methods

1. NMR instrumentation

The working principles and therefore the basic components of an MRI scanner and an NMR spectrometer are nearly identical. The only notable difference is the size of a typical sample. While a sample tube is used for analysis in case of NMR spectrometer, the whole body of a patient is examined in MRI.

In an NMR spectrometer, the sample is inserted into a probe, placed in a uniform magnetic field produced by a superconducting magnet. Liquid nitrogen and liquid helium are used to obtain and maintain the superconductivity. Once the polarization of the spin states is attained with the help of the magnetic field, radiofrequency pulses, designed and controlled by the electronic circuit of the console are applied using the probe coil. The response received by the same coil later is first amplified through the amplifier before feeding it to the user terminal via console for Fourier transformation and display cum analysis of the spectra.

This chapter describes, in brief, the basic components of an NMR spectrometer.
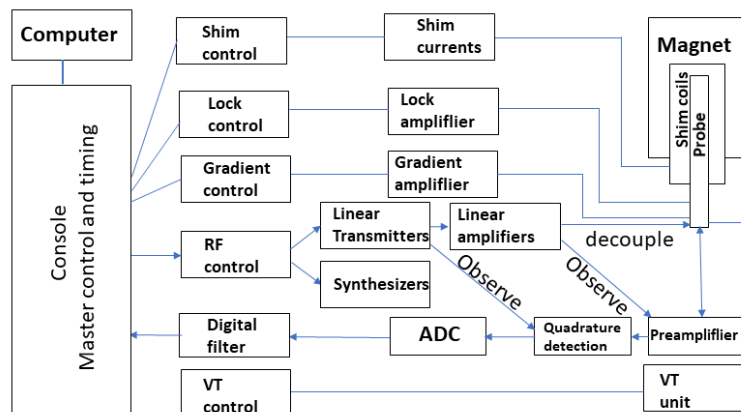
Figure 1: Block diagram of an NMR spectrometer. The three major components are the magnet, console and the computer.

1.1 Transmitting path: Starting from the synthesizer in the console, the transmitting path extends all the way to the radiofrequency coil inside the probe (figure 1). The transmitter basic frequency, responsible for determining the off-set frequency, phase, and duration of an RF pulse, is determined by the synthesizer. The frequency can be adjusted in steps of as small as 0.1 Hz whereas phase can be changed in steps of 1^0. Time dependent amplitude of a shaped pulse are modified based on different waveforms. The radiofrequency pulse is fed to an attenuator for setting up the power level before it finally enters the linear amplifier. The radiofrequency power can be attenuated over a wide range in steps of 0.1 dB or in few spectrometers even smaller. Upon exiting the amplifier, the pulse signal travels all the way to the probe to produce an oscillating magnetic field having linear polarization and with a maximum power of B_1 (RF field). In other words, the pulse generated by the electronics is a definite set of instructions (intensity modulations, phase modulation, duration) that the probe reads and produces the desired oscillations of the magnetic field. For a one pulse experiment, this pulse is delivered to the sample just before signal acquisition. A bandpass filter is placed in between the probe and the linear amplifier to optimize different channels with different frequencies (generally tuned to the Larmor frequencies of different nuclei types) when more than one channel is used. The bandpass filter blocks undesired frequencies from entering a specific channel. As explained in the previous chapter (section 1.2.1), only one of the two circular components of the linearly polarized rf filed interacts with the nuclei. Among the two counter rotating components which one would interact with the spins is governed by the sense of Larmor rotation given by the sign of the gyromagnetic ratio of the nuclei. Consequently, half of the power delivered by the transmitter are not utilized to excite the spins. In general, for protons, the power of the transmitter lies in the range of 50W to 100W. It is obvious that for nuclei having a smaller value of the gyromagnetic ratio (γ), a higher value of radio-

frequency power (B_1) would be required to achieve the same flip angle (α) for a given pulse length (τ_p) as $\gamma B_1 \tau_p = \alpha$. If the power is not set suitably high, then the pulse length of a given flip angle pulse becomes extremely long resulting in a narrower bandwidth of excitation. Consequently, for nuclei other than proton, the required transmitter power ranges between 300W and 400W. Irrespective of a specific transmitter channel, identical power is supposed to be produced at the probe for a particular power-level value set by the signal generation unit. This is termed as the linearity of transmission pathway. The linearity requirement is expected to be satisfied for all the components of the transmitter path including the power amplifier at the end. In absence of linearity, the efficiency of shaped pulses would have a detrimental effect and rigorous adjustment of phase would become mandatory for pulses with diverse power requirements. The linearity requirement should be in place for high powers also as for some shaped pulses the peak power requirement is quite high. The primary advantage of linearity is that the power of all pulse shapes can be estimated based on a rectangular pulse regardless of the wide variation in pulse phase, shape, power, and, pulse length.

The power of a transmitter is designated by its ratio to a reference power on a logarithmic scale of base 10.

$$P[dB] = 10\log(P_{ref}/P) = 20\log(V_{ref}/V) \qquad (1),$$

where, V is the applied voltage. The radiofrequency field is related to the applied voltage of the RF coil. To reduce any pulse length by a factor of 2 while maintaining the flip angle, the voltage needs to be doubled or in other words, the power needs to be quadrupled. In terms of logarithmic ratio, the power will change by 6dB to modify the pulse length by a factor of 2. Similarly, the required power of a shaped pulse can also be calculated from the pulse length of the corresponding 90^0 pulses.

In addition to dB, dBm is also used in few spectrometers to designate the power depending on the logarithm of magnitude of power expressed in milliwatts.

$$P[dBm] = 10\log(P[mW]) \hspace{4cm} (2).$$

The peak-to-peak voltage of a load, having the resistance of 50 ohm, is used to estimate the amplifier power with the help of the following expression:

$$P = V_{pp}^2 \,/400 \hspace{4cm} (3),$$

where, V_{pp} is the peak-to-peak voltage.

The amplitude of B_1 is often expressed in the unit of micro-Tesla (μT). For a probe having a pulse length of 8 μs for a 90^0 pulse for protons delivers 732.8 μT of radiofrequency field in case of a rectangular hard pulse.

Outcome of NMR experiments depends heavily on the stability of the amplitude and the phase of the radiofrequency pulses used. generally High precision is maintained for these parameters with the help of other hardware components of modern-day spectrometers. There exist test procedures like parameter optimization as well as pulse calibration, in order to rectify any possible degradation of the spectrometer performance.[1]

1.2 Receiving path: Starting from the radiofrequency coil of the probe, the receiving path extends all the way to the spectrometer computer where the digitized signal is stored in its memory. The response produced by the precessing nuclear spins are taken up by the probe as an oscillating voltage and is fed to the preamplifier. The voltage is generally of the order of μV or even smaller when received by the receiver coil. To minimize any major signal loss during the process of signal transmission from the probe to the amplifier, the amplifier is physically placed as close as possible

to the RF coil (short wiring). Quality of both the amplifier as well as the receiving coil in the probe is pivotal in obtaining a good signal to noise ratio. The electronic console receives the amplified signal from the preamplifier where it is converted to an intermediate frequency range with the help of a reference board.

Inside the console, the signal is divided into two channels by mixing the signal with a signal of a reference frequency having 90^0 phase shifts between the two channels. These two channels produce, respectively, the sine and the cosine modulations of the signal, required for quadrature detection. This way separation of positive and negative frequency with respect to the carrier frequency becomes possible. In presence of the quadrature detection, the bandwidth that is measured becomes half of the original and simultaneously the noise is reduced by a factor of $\sqrt{2}$. After digitization, the signal is fed to a digital filter that suppresses noise further and removes signal components lying outside the specific frequency range. The resultant digitized signal is stored in the memory of the computer. Narrowband analogue filters may also be used instead of a digital filter. The advantage of digital filtering has already been discussed. Resolution of at least 16 bit is necessary for the digitizer to have a suitably high dynamic range to digitize weak signals coming, for example, from nuclei of macromolecules.

To obtain a good signal to noise ratio, the components of the receiving path should be tuned properly. The receiving coil should be tuned to the Larmor frequency in question and matched to an impedance of 50 ohms. Insertion of a bandpass filter in-between the preamplifier and the probe are necessary while a heteronuclear decoupling sequence is used at the time of acquisition. These filters block the noise generated in the decoupling channel from getting into the receiving path. Apart from that, the analogue signal voltage amplitude should not transcend the dynamic range of the analogue to digital converter or the amplifier or the mixer.[2]

1.3 Lock system: The main magnetic field B_0 is in principle stable, but it drifts very slowly with time. Also, it changes by a tiny amount if the room temperature or the atmospheric pressure changes. If the magnetic field B_0 changes during long experiments, the Larmor frequencies of the studied spin assembly (I) will be statistically distributed around the Larmor frequency that they had at the beginning of the experiment. Under field drift Larmor frequency takes the form,

$$\omega_I(t) = [\omega_I + \gamma_I \Delta B_0(t)] = \gamma_I(1\text{-}\sigma)B_0 + \gamma_I \Delta B_0(t) \qquad (4),$$

where, γ_I is the gyromagnetic ratio of spin I.

In the same manner if the main magnetic field changes with time then the Larmor frequency of deuterium or fluorine also changes and become time dependent.

$$\omega_D(t) = [\omega_D + \gamma_D \Delta B_0(t)] = \gamma_D(1\text{-}\sigma)B_0 + \gamma_D \Delta B_0(t) \qquad (5).$$

The rule of the lock is to compensate the field drift in a way that

$$\frac{d(\gamma_D \Delta B_0(t))}{dt} = \frac{d(\omega_D(t)\text{-}\gamma_D(1\text{-}\sigma)B_0)}{dt} = 0 \qquad (6).$$

If this condition is fulfilled, the lock frequency becomes constant and we have,

$$\Delta B_0(t) = \frac{1}{\gamma_D} = C \qquad (7).$$

As a consequence of field locking, the resonance frequency of spin I changes into

$$\omega_I(t) = (1\text{-}\sigma)[\omega_I(0) + \frac{\gamma_I}{\gamma_D}] = (1\text{-}\sigma)[\omega_I(0) + \gamma_I C] \qquad (8).$$

If the field is locked, the Larmor frequency of spin I also becomes constant.

Frequency locking is done by a second permanent spectrometer, which contains an RF transmitter, a receiver, a preamplifier and a RF coil tuned to the deuterium or fluorine frequency. This spectrometer is simply called the lock.

The lock circuit continuously detects the resonance position and following any deviation, an appropriate current is passed to the Z_0 coil of the room temperature shim coil. A minuscule amount of homogeneous magnetic field is added or subtracted to the external magnetic field to restore the previous condition of field-frequency lock. The resonance deuterium signal is phased dispersive by suitably phasing the lock signal. This is done as a pure dispersive signal has a node at the middle of the shape and movement of that zero point is easy to follow. In case of improper tuning of the phase, the response of the lock system would be non-linear. As a result, an inappropriate deviation would be recorded which would, in turn, deliver incorrect magnetic field to the Z_0 coil and the field frequency lock would be disturbed.

The lock power is generally set slightly below saturation. Saturation is manifested by widely changing lock level. Alteration of the power setting effects the lock phase and hence phase recalibration is required. When experiments are done in the water sample, addition of up to 10% of D_2O is sufficient to generate an appreciable field frequency lock. At the time of shimming, the homogeneous nature of the main field can be estimated by the absorptive line of the deuterium signal. In unlocked situation, the field at the Z_0 coil is swept across a small range of frequencies to assist the system finding the lock frequency. In case of certain experiments where a spectrum is recorded without the lock, for example during deuterium experiments, the sweep should be switched off.

1.4 Magnet: The degeneracy of the Zeeman spin states is removed by the application of an external magnetic field, B_0. Larger magnetic field brings in wider dispersion of chemical shift along with increased sensitivity as sensitivity is proportional to $B_0^{3/2}$. To keep the solenoid, that produces the static high field, in the superconducting state, liquid nitrogen and liquid helium are filled in the spectrometer at regular interval. Superconducting magnets generally produce an appreciable stray field that has a spread of about a few meters from the magnet, although the extent of spread is dependent on the type of magnet. Any type of disturbance of the stray field disturbs in turn the main magnetic field homogeneity adversely affecting the quality of NMR measurements. Therefore, for a steady prolonged operation of the magnet, regulation in the fringe field area is mandatory. In an area surrounding the magnet where the stray field is higher than 1mT, movement of large ferrous objects (elevators, cars) must be restricted. The NMR laboratory itself should contain the 0.5mT (or 5 Gauss) stray field area for safety concerns. Recently, magnet system with active shielding is being developed to minimize the area of the stray field and thereby decreasing its detrimental consequences upon NMR measurements. Where a conventional magnet produces a stray field of 0.5mT in a horizontal distance of 3m from itself, for a magnet with ultra-shield, this distance reduces to 1.5m. Apart from the disturbance in the stray field, ground vibration also influences the quality of NMR measurements. Ground vibration is imparted to the magnet in general via the magnet stands, resulting in a fluctuation of the main magnetic field. This type of disturbances produces sidebands in the NMR spectrum.

Conventionally, magnetic fields are expressed in the unit of Tesla. In the case of NMR, the magnetic field is often expressed in terms of the Larmor frequency of isolated proton (without electron shielding effect) at the corresponding magnetic field (equal to $\gamma_H B_0$). For example, at a magnet strength of 9.3T, the resonance Larmor frequency of the proton becomes approximately

equal to 400 MHz. NMR systems having magnetic field higher than 100 MHz requires superconducting magnet or else, the power required for bringing the desired magnetic field becomes very high. Superconductivity is achieved at the liquid helium temperature of 4.2K at standard pressure. Solenoid winding made up of Niobium tin alloy ingrained in a copper wire is generally used to construct the coil of the magnet. At that low temperature, niobium alloys achieve superconductivity. In case of accidental disruption of the superconductivity, termed as "a magnet quench", the large current that passes through the copper wire generates a lot of heat facing the full resistance. The copper wires dissipate the heat efficiently by boiling off the liquid helium and thereby protecting the superconducting wire from melting. The protective resistors, embedded parallel to the main coil, dissipates maximum energy. It is possible that the solenoid be recharged back to superconductivity after a magnet quench, restoring the same performance. Superconductivity disappears at a critical value of magnetic field strength as well as current density and these factors are major constraints in designing magnets with higher field strengths. The endurance of superconducting magnets lies in its capacity of operating steadily without any further supply of power after the charging is complete. For such high stability, the junction resistance must be immensely low (theoretically zero) at the joints of superconducting wires to slow down the reduction in the circulating current and thus the magnetic field. The rate at which the magnetic field decays over time is termed as temporal stability. The field drift of a modern NMR spectrometer is so negligibly small that the resonance frequency of ^{1}H nuclei is shifted only by about few Hertzs per hour. At this rate, more than two decades would be needed for a reduction of the field strength by 1MHz.

Apart from the main superconducting coil, additional superconducting coils (known as cryo-shim coils) are introduced to the magnet to achieve better field homogeneities. These coils are

responsible for producing gradients across the length of the superconducting coil. To achieve further field homogeneity, essential for high-resolution NMR, some non-superconducting coils are placed as part of the room temperature components of the magnet bore. This is referred to as the room temperature shim coils. Approximately 25-30 types of shim coils are used to achieve a proton line width of approximately half a Hz at the full width at half maximum along with around 5 Hz and 8 Hz respectively at 0.55% and 0.11% of the maximum peak height without spinning with a suitable calibration sample such as 1% chloroform in acetone-d_6. Line shapes can further be improved by rotating the sample so that residual inhomogeneities along the transverse directions are removed. But spinning also brings in fluctuations that might impact the efficiency of multidimensional NMR in resolving peaks. Direct shimming on D_2O may not be useful in adjusting field homogeneities because of its insensitive and unresponsive nature towards the solvent-induced change in the magnetic field compared to that of the acetone-d_6 deuterium signal. Judicious use of multiple samples having different filling heights and comparative magnetic susceptibility with respect to water helps in achieving excellent homogeneity. Shimming using field gradients is possible now with most modern probes. This is highly effective for sample solutions containing water as solvent. It takes only a few minutes with gradients to achieve a good line shape form a set of standard shim values using the gradient shimming procedure.[3]

1.5 Probe: The probe is made-up of a resonance tank (RC) circuit having a coil (solenoid) that transfers the radiofrequency excitation to the nuclear spins of the sample and later receives the induced voltage produced by the precessional motion of nuclear bulk magnetization. Although use of two separate coils, one for receiving and the other for transmitting would be conceptually advantageous but two coils, tuned to similar frequencies, generates interference among them and as a result the performance deteriorates. This magnetic field, having a linear polarization, lies

perpendicular to the externally applied static magnetic field. The coil remains firmly fixed inside the probe. The coil materials are chosen carefully to prevent any background NMR signal generation from these materials. Tuning is referred to as the adjustment of the capacitance values of the RF circuit until the required frequency is reached. Whereas matching is referred to as adjustment of the impedance values of the RF circuit so that it matches the impedance of the sample for better power transfer between the coil and the sample. This is usually achieved by adjusting two variable capacitors in the circuit. Proper tuning reduces reflected power leading to shorter pulse widths and better sensitivity. At a time one coil can be tuned to three separate frequencies or can be tuned to frequency range having additional frequencies. Highest efficiency can be achieved if one coil is tuned to only one frequency instead of a range of frequencies. The receiver coil is placed very close to the sample to prevent signal loss. This proximity might induce problem when there is a considerable amount of difference in magnetic susceptibility of the coil to that of the air, used for stabilization of sample temperature. This results in distortion of static magnetic field making shimming (process of making magnetic field across the sample length homogeneous as previously discussed) cumbersome. Therefore, the use of coils having similar susceptibilities with respect to air or nitrogen is always advantageous. To work with more than one frequency, additional coils are mounted close to the receiving coil. These additional coils are used while experiments containing polarization transfer or decoupling are recorded.

One of the important parameters describing probe efficiency is termed as the Q factor or quality factor. This factor signifies the extent of damping in the circuit of the probe coil. Generally, increasing the value of the quality factor helps in achieving higher sensitivity as a higher radiofrequency field can be achieved with a given radiofrequency power. Apart from damping, Q values are also used to estimate the time lag associated with the change of power or phase of the

radiofrequency perturbations. Although, the quality factor of a commercial probe ranges from 300 to 400, higher values can be obtained with superconducting coils.[4] In spite of having a higher value of quality factors, low salt-tolerance prevents the potential application of superconducting probes towards measurement with biological macromolecules as with increasing salt concentration, the conductivity of the solution increases resulting in decreased efficiency of the tuning capacitor. The resonance circuit response of a probe is dependent on its electromagnetic properties. These characteristic properties get detuned during sample spinning either due to a sample tube which is not perfectly cylindrical or due to inconsistent spinning rate. Such modulations can generate sidebands leading to the spurious interpretation of the multidimensional experiments.

Another important property of the coil is the spatial uniformity of the radiofrequency perturbation during the application of a pulse.[5] Given a pulse length, with a non-uniform pulse, there would be difference in flip angles of the spins situated at different positions across the length of the sample. Although the effect is generally not so prominent while using a single 90^0 pulse, execution of multiple rf pulses during a multidimensional NMR experiment introduces considerable cumulative phase error along with considerable loss of signal. The conventional procedure to estimate the rf inhomogeneities is to measure the ratio of the signal after application of an 810^0 pulse to that of the signal after the application of a 90^0 pulse. For a well-designed probe, the ratio should be higher than 75%. The electric field of the RF pulse is also responsible for producing substantial inhomogeneities. Due to the presence of the electric field, a considerable amount of heat is generated after the application of multiple pulses or during the decoupling. Because of the absence of homogeneity in the electric fields, the heat produced is not uniform and as a result, temperature increases non-uniformly within the sample. If the sample length is comparable or slightly lesser than the size of the coil, then the RF, as well as temperature inhomogeneity, can be reduced.

Sample plugs having similar magnetic susceptibility with the solution can also be used to limit the volume of the sample and achieve superior homogeneity.

1.6 Magnetic field gradient coil: Magnetic field gradients are employed to produce controlled linearly varying field inhomogeneities of certain strength. Pulsed field gradients are extensively used to examine the translational diffusion property of a molecule undergoing Brownian motion in solution. After the introduction of gradient coils having active shielding, it is routinely used in NMR spectroscopy because of it's very short recovery times. The short recovery time helps in attaining the homogeneous magnetic field very quickly after the gradient is applied. The spatial location of a nuclei in a gradient field determines its resonance frequency. Under the application of a magnetic field gradient directed along the z-axis and having gradient strength G Gauss per unit length, the spatially dependent resonance frequency of a nucleus is given by:

$$\omega(z) = \omega_0 + \gamma Gz \tag{9}$$

The resonance frequency in the absence of gradient is designated by ω_0. The time evolution of the operators needed to characterize an NMR experiment is dependent on their spatial orientation with respect to the vertical direction. The operators attain a phase while the pulsed field gradient is applied for a duration τ.

$$I^+(\tau) = I^+(0) e^{i\gamma Gz\tau}$$

$$I^-(\tau) = I^-(0) e^{-i\gamma Gz\tau} \tag{10}$$

The phase dispersion of the operator is dependent upon the gyromagnetic ratio of the nuclei under the gradient field and as a result, nuclei having a smaller value of gyromagnetic ratio would

undergo lesser spread of resonance frequencies. The net magnitude of magnetization across the sample length L is governed by the following relationship.

$$M = \frac{\sin(\gamma G\tau L/2)}{\gamma G\tau L/2} = \text{sinc}(\gamma G\tau L/2) \tag{11}.$$

The sinc function having damped oscillation produces a considerable amount of signal in between the zero-crossings and thus the quantity $\gamma G\tau L$ should be tuned properly to prevent possible interference affecting the experiment. It is generally done by taking sufficiently long τ.

The two major applications of pulsed-field gradients are (i) encoding of the spatial parameters to the coherences, and (ii) selection of coherence pathways and elimination of undesired magnetizations. While the first one is used for measurement of the translational diffusion coefficient of a molecule, the second one replaces the cumbersome requirement of long phase cycles for the selection of a desired coherence transfer pathways. Gradients have the potential to select the desired magnetization in one scan compared to phase cycle schemes where multiple transients should be recorded for the addition and subtraction of undesired coherences, thereby increasing the experimental time. For the desired magnetization, the summation of all the phase factors associated with the coherences should converge to zero. The other coherence pathways are unable to produce a significant amount of signal when ample strength of gradient is used. Incidentally only half of the signal, dephased by the gradient can be refocused by placing a 90^0 pulse in between the two gradients. Apart from this a considerable amount of signal is lost via dephasing introduced by diffusion. This severely affects the small molecule magnetization as for example the solvent magnetization.

Radiofrequency pulses having spatial inhomogeneity can also produce the effects of field gradients. This can be achieved either by the fundamental non-uniformity of the transmitter or by the application of a different RF coil specially calibrated to produce non-uniform radiofrequency field. The advantage of radio-frequency gradients compared to pulsed-field gradients lie in their frequency selectivity. However, heat is produced while radiofrequency gradients are applied and that limit their application when high gradient strength is used.

New generation probes contain actively shielded coils, in addition to conventional RF coils, for application of magnetic field gradients. Currents close to 10A is passed through these coils to achieve a gradient strength of up to 50 G/cm. When this large amount of current is either switched on or switched off, the gradient coil vibrates and additionally induces eddy current in the surrounding metallic components of the probe. These factors hinder speedy recovery of the homogeneity of the magnetic field after a gradient is applied. The recovery time for a present day probe, fitted with a z-gradient, is around 100 µs after the application of a 2 ms long gradient pulse. With the use of sine or sine square-shaped gradient, even shorter recovery times can be achieved.[6] In case of a triple-axis gradient coil, the interference of individual eddy currents elongates the recovery time. Contrary to this, triple-axis gradients are less cumbersome to implement in avoiding accidental refocusing of undesired magnetization during an experiment. Moreover, gradients may be utilized for all the shims. The non-axial fields in absence of triple axis gradient can be shimmed with the help of room-temperature shim coils, but the result is almost never adequate. Information about the absolute strength of a gradient may be obtained approximately by using an easy calibration method. When the gradient is used at the time of acquiring the water signal of an H_2O sample, the peak width may be correlated to the approximate gradient strength, G_i along the "ith" axis by using the following analytical expression:

$$G_i = 2\pi\Delta v /(\gamma d) \tag{12},$$

where, Δv is the resonance linewidth and d is the length of the radiofrequency coil. Measurement of the diffusion coefficient of water at a particular temperature can also be used for the estimation of the gradient strength. The ratio of the reported diffusion coefficient with properly calibrated gradient strengths to that of the observed diffusion coefficient gives the gradient strength. Even though the knowledge of absolute gradient strength is generally not required, for experiments where gradients are used to select coherence pathways, the relative strength of two or more gradients needs to be calculated. Wrong setting of relative gradient strengths leads to a significant amount of signal loss and phase errors.

1.7 Variable temperature operations: To prevent temperature-induced change of chemical shift, the sample temperature is kept as stable as possible. This becomes particularly important for samples with D_2O as the lock solvent, as water chemical shift is highly sensitive to change in temperature (in the order of 0.01ppm/Kelvin). When the sample temperature is not sufficiently stable, the lock system tries to compensate the water resonance shift, resulting in a shift for other resonances which might have other temperature dependences. For two or higher dimensional NMR measurements, such shift hinders the full alignment of resonances between indirect dimension increments resulting in the appearance of axial peak or t_1 noise. Additionally, fluctuation in temperature brings in a substantial amount of subtraction errors for experiments that use phase cycles or the principle of difference spectroscopy.

In order to regulate the temperature, air is flown around the sample after passing through a heating component. A feedback mechanism is used to control the air temperature by regulating the heater power. To achieve optimum temperature control, the inflow gas temperature is generally set at 10

K lower than the temperature required at the probe. As long radiofrequency perturbation produces heat during, say, decoupling sequences, the target temperature is set even lower during such experiments to make use of the produced heat. Generally, the airflow takes the heat out from the probe. The lowering of temperature through airflow can be experimentally determined by comparing the resonance frequency of a methyl group under the application of a single 90^0 pulse to the resonance achieved by the application of complicated pulse sequences. The rate of rise of temperature during an experiment should not be steep enough so that it induces coil movement through high airflow or convection of solution within the NMR tube. Sidebands produced by the vibrating coil are in general broad and are placed thousands of hertz apart from the strong solvent signal. These sidebands are easily identified based upon their sensitive nature towards the rate of airflow.

In case of a temperature regulation failure, in-built circuits and carefully selected regulation parameters protect the sample from possible damage due to overheating or freezing. The heater current is set to a lower value to maintain the temperature when the gas in-flow is stopped. When the inflow is settled a heatwave may enter the probe causing damage to the sample. These factors are carefully considered when regulation parameters are chosen.

2. Acquisition of CEST experiment

2.1 Deuterium Exchange To understand the exchange characteristics of the labile proton(s) of a CEST contrast agent, the solute is first dissolved in a deuterated solvent which does not contain any exchangeable or labile deuterium, and hence is incapable of replacing the proton of the solute through chemical exchange. Among the commonly used organic solvents, $CDCl_3$ generally contains an appreciable amount of dissolved DCl which exchanges with the protons of interest. As deuterium is not observed during a proton experiment, the intensity of the exchangeable peak

diminishes post deuterium exchange. To prevent such unwanted deuterium exchange, $CDCl_3$ is generally used after passing it through K_2CO_3 as then the dissolved DCl gets removed. DMSO-d_6 is a useful alternative for two reasons. First, it does not contain any exchangeable deuterium and secondly, due to the presence of a highly electronegative oxygen atom, DMSO produces a hydrogen bond type of interaction with the solute exchangeable proton through that oxygen. Thus, the resonance frequency of the exchangeable proton can be easily identified by the downfield shift resulting out of hydrogen bond type of interaction. After recording the proton NMR spectrum with DMSO-d_6 as a solvent, a very little amount of D_2O (~10-20 μL) is added to the solution in the NMR tube. Because of the exchange of proton with deuterium in D_2O, the exchangeable proton resonance suffers a significant loss of intensity. This way the exchangeable proton is identified.

After the temperature calibration is done, a sample tube having a solution (either in buffer or biological media) of the contrast agent along with one D_2O filled capillary (placed co-axially with the NMR tube) is inserted into the magnet. After locking, tuning, matching and shimming an ^1H spectrum is recorded. This serves two purposes. First, it verifies whether proper line shape has been achieved for the water resonance or not and second, it gives the exact resonance frequency of the bulk water. The resonance frequency of bulk water is dependent on sample temperature as well as the pH of the solution.

Although the resonance frequency of the exchangeable proton can be precisely known from the ^1H NMR spectrum recorded with DMSO, a solvent-induced change in frequency remains always a possibility. When the contrast agent is dissolved in buffer, the labile proton peak disappears due to exchange with the bulk water. Thus, the exact frequency of the exchangeable proton in water is never directly determined. To find the resonance frequency of the exchangeable proton in buffer and to apply saturation RF power on resonance or nearly on resonance to the labile protons, the

RF irradiation is first scanned through a range of frequencies. The irradiation frequency list having a defined resolution (difference between two consecutive irradiation frequencies) is created taking bulk water resonance in the middle of the range. In the present thesis this has always been done with the help of an in-house MATLAB code. The bulk water resonance frequency is prcisely obtained from the ^{1}H NMR spectrum of the solution containing the agent and the buffer.

The inputs required to make the frequency list are (i) the basic frequency of the spectrometer in MHz (ii) resonance frequency of water in Hz (iii) minimum and maximum ppm with respect to water. The saturation radiofrequency pulse is scanned across the ppm range. (iv)the resonance frequency in ppm which is far away from the resonance frequency of the water as well as the exchangeable proton. The intensity of water signal that is obtained when RF saturation is applied at this ppm is considered as standard for normalization of water intensity obtained at different frequency offset, and (v) resolution in ppm.

All the research work included in this thesis has been done using a Bruker Spectrometer. As a consequence, the discussion below on the specific steps of the experiments are presented using Bruker terminologies. However, this is rather obvious that these experiments can be performed on any spectrometer.

Once the offset frequency list is created it is exported to C\Bruker\topspin 3.2\exp\stan\nmr\list\fq2list.

The pulse program that we used for acquiring data for constructing all the z-spectra for this thesis, '*stddiff*', is shown in figure 2
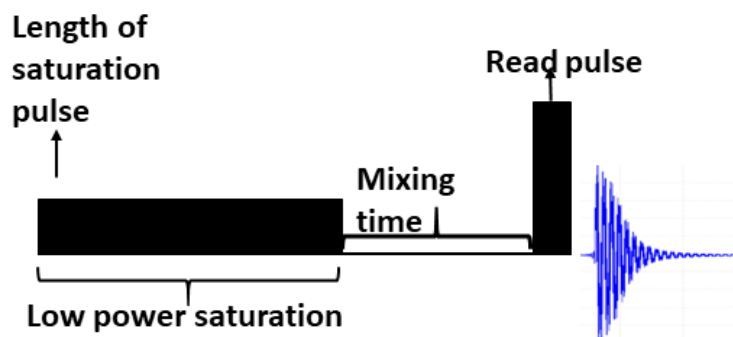
Figure 2: Pulse sequence diagram for saturation transfer experiment. Shaped pulse is indicated below.

In this pulse sequence, a long train of low power shaped pulse each of a few milliseconds is applied at a given frequency. To construct a z-spectrum, the pulse program is repeated for each frequency from the prepared frequency list. When the selective pulse train is applied on-resonance or close to the on-resonance frequency of the exchangeable solute proton, the labile proton gets saturated. During the long pulse train, this saturation gets transferred from the solute to the solvent (bulk water) through chemical exchange. After the application of this frequency selective pulse train and saturation transfer, a non-selective 90^0 read pulse is applied to measure the signal intensity of the bulk water. Upon chemical exchange of the saturated solute spins with water protons, the signal intensity of bulk water decreases resulting in the formation of CEST contrast.

Details of the experimental parameters of a typical CEST experiment and their impact on CEST profile and contrast are discussed below.

2.2 Effect of B₁: CEST contrast is produced when saturation is transferred from the solute, resonating away from the solvent (bulk water) to the bulk water. As discussed earlier, in order to produce the contrast, the solute to solvent exchange rate should lie in the slow to medium exchange regime with respect to the NMR time scale. Saturation is attained using a radiofrequency pulse train on resonance, with the total duration of saturation being sufficient for multiple exchanges to

happen. Although several mathematical models are available for the estimation of CEST efficiency, one of the most convenient models is the two-pool model.[7-9] In case of CEST, the solute pool (having concentration in millimolar range) and the solvent pool (concentration in 55M range) exist with high concentration difference and thus the exchange rate is governed by a pseudo-first-order rate equation. Such a two-pool model proves often to be sufficient for analysing in-vitro[7] as well as in-vivo[10] data. While all exchange rate in this thesis have been estimated using the two-pool method, other alternatives such as numerically solving the modified Bloch equations do exist.[8, 11] The mathematical equation, governing the CEST contrast after the application of a frequency selective RF irradiation, is given by

$$\text{PTR} = \frac{S_{0w} - S_w(t_{sat}, \alpha)}{S_{0w}} \tag{13},$$

$$= \frac{k_{sw} \cdot \alpha \cdot X_{CA}}{R_{1w} + k_{sw} \cdot X_{CA}} [1 - e^{-(R_{1w} + k_{sw} \cdot X_{CA})t_{sat}}] \tag{14}$$

where, PTR designates the proton transfer ratio, X_{CA} is the fractional ratio of solute protons to that of the bulk water protons. t_{sat} and α designate the saturation duration and saturation efficiency respectively and k_{SW} is the solute-water exchange rate. S_{0w} and S_w represents the water signal intensity respectively when saturation is incurred far away from the exchangeable solute and on the solute itself.

The saturation efficiency is defined as:

$$\alpha = \frac{\omega_1^2}{\omega_1^2 + pq} \tag{15},$$

Where, p and q are given by:

$$p = R_{2s} + k_{sw} - k_{sw}^2 \cdot X_{CA} / (R_{2w} + k_{sw} \cdot X_{CA})$$
$$q = R_{1s} + k_{sw} - k_{sw}^2 \cdot X_{CA} / (R_{1w} + k_{sw} \cdot X_{CA})$$

$$(16).$$

Extensive mathematical calculation based on three-pool model or higher, has also been reported.[8, 12-13] These theories consider more than one exchangeable proton pools along with semi-solid pool of solute protons.

Experimentally, CEST z-spectrum is constructed by plotting the normalized (w.r.t equilibrium intensity) water intensity as a function of frequency offset. When irradiation is applied at the resonance frequency of the solute having an exchangeable proton, a considerable amount of water signal intensity is reduced because of the transfer of saturation. Additionally, a large valley of direct saturation (DS) is produced resulting from the direct water saturation when the saturation offset frequency covers the bulk water resonance frequency. This is termed as a spill over of water. For a considerably long saturation duration, the saturation transfer attains a steady-state and Eq. 13 is reduced to

$$S_w^{ss} = S_{0w} \frac{R_{1w} + k_{sw}(1-\alpha)x_{CA}}{R_{1w} + k_{sw}x_{CA}}$$

$$(17).$$

Where, S_w^{ss} is the water signal intensity at steady state.

which after rearrangement reduces to: $\quad 1 - \dfrac{S_w^{ss}}{S_{0w}} = \dfrac{k_{sw}\alpha x_{CA}}{R_{1w} + k_{sw}x_{CA}}$

$$(18).$$

Considering $R_{1w} \gg k_{sw}x_{CA}$ and for a complete saturation the above equation can be further simplified[14] to

$$1 - \frac{S_w{}^{ss}}{S_{0w}} = \frac{k_{sw} X_{CA}}{R_{1w}} \qquad (19).$$

For a CEST agent, having concentration of 20mM, and exchange rate of 200 rad/s the factor at the numerator of Eq. 19 becomes approximately equal to 0.018 s^{-1}. This is significantly lesser than the longitudinal relaxation rate of water (4 s^{-1} at 310 K). Hence the above approximation can be used to estimate the CEST contrast *in vitro*.

Another metric that is often used to quantify conventional magnetization transfer contrast is the proton transfer efficiency (PTE), given by

$$PTE = \frac{k_{sw} \alpha}{R_{1w} + k_{sw} X_{CA}} [1 - e^{-(R_{1w} + k_{sw} X_{CA}) t_{sat}}] = PTR / X_{CA} \qquad (20).$$

PTE can be used to compare the proton transfer efficiency of different contrast agents per unit concentration.

Conventionally the total water saturation is denoted by:

$$\frac{S_w(\Delta\omega)^{total}}{S_{0w}} = PTR^{exo}(\Delta\omega) + PTR^{endo}(\Delta\omega) + MTC(\Delta\omega) + DS(\Delta\omega) \qquad (21),$$

where, endogenous and exogenous proton transfer ratio is referred by PTR^{exo} and PTR^{endo} and MTC refers to magnetization transfer contrast resulting from the cross-relaxation between macromolecules and bulk water.

Because both the direct saturation as well as magnetization transfer contrast are symmetric with respect to the resonance frequency of water, by separating the CEST effect from DS and MT, MTR_{assym} can be defined as:

$$MTR_{assym} = MTR^{total}(\Delta\omega) - MTR^{total}(-\Delta\omega)$$

$$= \frac{S_{sat}(-\Delta\omega) - S_{sat}(\Delta\omega)}{S_{0w}} \tag{22}.$$

Although in the case of paraCEST agents, having large offset for the exchangeable protons with respect to water, the MTC is symmetric, this condition might not be always true for diaCEST agents having smaller offsets lying in the range of a few KHz.[15] Hence the asymmetry of MTR will be contaminated by MTC which is no more symmetric.

The proton transfer efficiency increases with increasing saturation radiofrequency power when the frequency difference is substantially higher compared to the RF field strength. When the frequency difference is comparable to saturation power then along with the effect of saturation transfer, a considerable amount of water spill over also starts happening. With the increase of saturation power, the proton transfer efficiency starts saturating but the water direct saturation continues to increase. Therefore, the RF power should be optimized in order to get the maximum proton transfer ratio, considering both saturation transfer and spillover effect.[16-17]

Baguet and Roby analysed the Bloch equations considering a two-pool model following a double base transformation approach[17-18] When the RF saturation is sufficiently strong the situation becomes simpler as all the magnetization components lying parallel to the effective field become negligible. Hence, this transformation is proved to be an efficient approach when the spillover effect is considered.

Thus, considering the increasingly asymmetric nature of MTC as well as the spillover effect, the saturation power used to study the contrast produced by diaCEST agent is comperatively lower compared to that of their paramagnetic counterparts.

2.3 Processing of z-spectra: The stddiff pulse program produces a pseudo-2D spectrum where the indirect dimension contains the series of resonance frequencies across which the RF saturation pulse is applied. This pseudo-2D spectrum is split into a number of 1Ds by the command '*splitser*'. Each of the 1Ds correspond to each of the irradiation frequency offset. The intensity of the water signal of each 1D is normalized with respect to the intensity of water signal obtained when the saturation RF pulse is applied at a resonance frequency which is far away from the frequency of the solute. The ratio of signal intensities is plotted against the corresponding irradiation offsets to get the z-spectrum. The spectral refererence is set to the frequency of water resonance in order to plot the water direct saturation at zero frequency.

2.4 Exchange rate measurement: Knowledge of the exchange rate is extremely important to estimate the potential of the contrast agent for *in vivo* applications and to tune it physically or chemically according to the need. MTR_{assym} calculation is not adequate to determine the exchange rate as the contrast produced is dependent on the concentration of the agent.

For a solute of high concentration having the exchange rate in the slow exchange regime, the exchange rate can be estimated through measurement of the line width (LW). This seems plausible as the linewidth is correlated with the spin-spin relaxation rate(R_{2s}) of the solute and the exchange rate[25-26] via the equation:

$$k_{sw} = \pi LW_s - R_{2s} \tag{23}.$$

This way of measuring the exchange rate is limited to *in vitro* samples as the information of transverse relaxation rate and the high concentration requirement is difficult to satisfy in-vivo. Another drawback of this approach is that the effect of field inhomogeneity is completely ignored.

Exchange rate can also be measured by the help of water exchange spectroscopy.[27-29] In this exchange rate measurement process, the inverted water magnetization is transferred to the solute within a duration termed as mixing time (t_m). In order to calculate the exchange rate the exchangeable solute signal is measured as a function of the mixing time and fitted using the analytical expression.[9, 28]

$$S_s(t_m) = \frac{k_{sw}S_{0s}}{k_{sw} + R_{1s} - R_{1w}}(e^{-R_{1w}t_m} - e^{-(k_{sw}+R_{1s})t_m}) \tag{24},$$

where, S_{0s} denotes the magnetization of solute protons at equilibrium. The rest of the terms have been introduced earlier. The convenience of this method lies in the fact that in the limit when the exchange rate is much higher than the longitudinal relaxation rates of the solute protons and bulk water, any error in the measurement of longitudinal relaxation rate does not influence the measurement of solute-solvent exchange rate. However, the method is not that efficient in determining fast exchange rates as then within a very short mixing time the maximum intensity is reached.

An extensive calculation of exchange rate, based upon the dependence of contrast on saturation duration and saturation power during a saturation transfer experiment, was performed by Mcmohan et. al. and the methods were termed, respectively, as quantification of exchange rate as a function of saturation time (QUEST) and saturation power (QUESP).[7] When a continuous wave saturation pulse is used, the water z magnetization can be fitted as a function of saturation duration using the Eq. 14 with the assumptions $k_{sw} = \Delta\omega$ and arctan $(\omega 1/\Delta\omega) < 30^0$, where $\Delta\omega$ denotes the chemical shift offset of the exchangeable solute and $\omega 1$ represents the RF field strength. However, the fitting parameters should be carefully optimized as they substantially influence the efficiency of the experiment. For instances, if the transverse relaxation rate of water is higher than

the exchange rate then the exchange rate might be miscalculated due to the presence of water direct saturation. The accuracy of the fitting is also determined by the choice of saturation power during QUEST or QUESP measurements. Moreover, in order to choose the appropriate irradiation power, prior knowledge of the approximate exchange rate is required. Best estimation of the exchange rate is provided by the numerical solution when the above-mentioned conditions are fully satisfied.

In a different approach, ratio-metric analysis on the QUEST data were performed to remove the dependency of the choice of saturation field strength.[30] Normalization of the asymmetric magnetic transfer ratio is generally done with respect to some reference frequency to reduce the influence of the longitudinal and transverse relaxation rate constants and saturation field strength on fitting.

Relatively newer method has been proposed to determine the exchange rate that utilizes pulsed saturation transfer.[31] This approach is based on multiple flip angles and can be implemented on a clinical scanner to estimate the exchange rate in an unbiased manner.

Other alternatives to these techniques have also been proposed to improve the exchange rate measurement. Omega plot method is one such method that estimates the exchange rate of the solute protons without having prior knowledge of the solute concentration.[20] In this method, the intensity of water signal in steady state is described by the form $S_s^{ss} / (S_0 - S_s^{ss})$ and is linearly fitted and plotted against $1/\omega_1^2$. Using the two-pool exchange model of the Bloch equation and under the conditions of negligible water direct saturation as well as faster exchange rate compared to the longitudinal relaxation rate of water, the value of $-1/k_{sw}^2$ becomes equal to the x-axis intercept of the fitting curve. This method is highly advantageous in measuring *in vivo* exchange rates, where the information about the concentration of the agent is not known. As the method assumes that the water direct saturation is negligible, this method is better suited for measuring exchange rate of

paraCEST agents having large frequency offsets. This way the contrast produced does not get contaminated by the effect of water spillover. In order to implement the omega plot method in determining the exchange rate of diaCEST agents, saturation power should be properly optimized. To achieve the condition of steady state the saturation duration should be sufficiently high. CEST experiments are generally performed first with varying saturation duration to choose the saturation duration at which the steady state is reached. That saturation duration is used for exchange rate calculation.

3 Relaxivity experiments: The relaxivity of a contrast agent is defined as the change in relaxation rate of water per unit concentration of the contrast agent. Given two different mechanisms for relaxation, the two different relaxivities namely the longitudinal relaxivity and the transverse relaxivity are given by

$$r_1 = \frac{R_{1,mix} - R_{1,wat}}{C} \qquad \text{And} \quad r_2 = \frac{R_{2,mix} - R_{2,wat}}{C} \tag{25}.$$

where, $R_{1,wat}$ and $R_{2,wat}$ are longitudinal and transverse relaxation rate constants of water in absence of the contrast agent. $R_{1,mix}$, $R_{2,mix}$ are, on the other hand, the corresponding relaxation rate constants in presence of the agent. C represents the concentration of the contrast agent which generally lies in the milimolar range. The spin-lattice relaxation time constant is routinely obtained using the inversion recovery method by plotting the recovered signal intensity after the application of an 180^0 pulse that inverts the z-magnetization followed by a variable delay and a read pulse. The spin-spin relaxation time constant, on the other hand, is obtained by the CPMG method in which the decay of transverse components of magnetization with time is measured. Relaxivity is dependent on the field strength as well as sample temperature.

In case of CEST contrast agent, the saturation incurred upon the exchangeable protons is transferred to the bulk water and the resultant drop in water signal intensity is measured. Hence, if the relaxivity of a CEST contrast agent is high then it would shorten the spin-lattice relaxation time of the bulk water appreciably and as a result the saturation transferred to the bulk water would not survive long enough for detection and the water magnetization will return back to the equilibrium very quickly. In such a situation even after efficient saturation of the exchangeable proton and consequent transfer to the bulk water, the produced contrast will be significantly lower. The relaxation time as well as the corresponding relaxivities values are highly dependent on the field strength of the main magnet. In general, with the increase of field strength the longitudinal relaxation time constant increases for smaller molecules which results in producing higher CEST contrast.

A particle in an excited quantum state returns to the ground state via two distinct pathways: radiative and non-radiative pathways. The relaxation process proceeds through a non-radiative pathway for NMR spectroscopy. On the other hand, radiation damping is a radiative pathway of relaxation. After the application of the radiofrequency perturbation, the transverse component of the magnetization induces a current in the receiver coil. This is termed as free induction decay (FID). Simultaneously the magnetic component of the produced radiofrequency field applies torque to the spin system and therefore force them in getting back to the equilibrium. This phenomenon is referred to as radiation damping. In the case of an aqueous solution, as the concentration of water is much higher compared to that of the solute, the magnetic field created by the water transverse magnetization is large enough to produce a high radiation damping. Due to the effect of radiation damping the relaxation time becomes substantially shorter.[32]

Although it has been stated that with the increase in the magnetic field the CEST contrast increases because of longer relaxation time constant, with higher magnetic field, generally comes probes with very high quality (Q) factor. With a properly tuned probe having a high Q factor, the effect of radiation damping becomes even stronger, leading to a decrease in the relaxation time constant of bulk water. As discussed earlier a shorter solvent relaxation time hampers the CEST contrast generation. In order to measure the longitudinal relaxation time correctly in presence of radiation damping, either the probe is slightly detuned or T_1 is calculated using the saturation recovery method instead of inversion recovery method.

In the present thesis, the spin-lattice relaxation time constants were obtained via inversion recovery method with a 9.3T magnet equipped with a BBO probe having negligible radiation damping. The data were processed using the Bruker Topspin software. Corresponding relaxivities were then calculated by using the equation described above.

4 Diffusion measurements: Diffusion NMR spectroscopy is a technique that is generally used to resolve a mixture of compounds according to their varying translational diffusion coefficient. The diffusion coefficient of a molecule depends on the radius and shape of the molecule. Thus, diffusion NMR spectroscopy is also used to determine molecular aggregates as well as the solvation cell size. The diffusion coefficient of a molecule undergoing Brownian motion can be estimated based on the Stokes-Einstein equation[33-34]

$$D = \frac{k_B T}{f_r} \tag{26},$$

where, f_r represents the drag produced by the solvent and is represented as $f_r = 6\pi\eta r_h$. The hydrodynamic radius of the solute is designated by r_h and the viscosity of the solvent is denoted by

η. It is assumed that the solution is infinitely diluted (very diluted in reality). In order to measure the diffusion coefficient through NMR, several methods were proposed.[35-36]

After the application of a radiofrequency perturbation, the transverse component of the magnetization starts decaying due to the transverse relaxation and magnetic field inhomogeneity. In the presence of a gradient, the decay becomes much faster. The ribbon of transverse magnetization forms a helix after the application of a single gradient of sufficient strength. If the pitch of the helix is lesser compared to the sample length, then the helix integral of the isochromats reduces to zero. In case of diffusion experiments, two gradient pulses having equal strength, but opposite polarity are used to unwind the helix. The second gradient rephases the magnetization that has been dephased by the first gradient, resulting in the formation of an echo. However, diffusion causes incomplete rephasing and from the diminished intensity, diffusion coefficient is calculated.

In case of a spin-echo diffusion pulse sequence the transverse component of the magnetization is dephased by using a gradient, which is later refocused by an 180^0 pulse followed by a gradient of same strength. The 180^0 pulse is used to change the coherence order from +1 to -1. The amplitude of the echo becomes equal to:

$$S(2\tau) = M_0 \exp(-2\tau/T_2)\exp[-Dq^2(\Delta-\delta/3)] \tag{27},$$

where, M_0 represents the bulk magnetization at equilibrium. The first exponential term accounts for the transverse relaxation and the term q^2 is equal to $\gamma^2 g^2 \delta^2$, where the gradient strength and duration are represented by g and δ respectively. D represents the translational diffusion coefficient of the system under investigation. The correction term $\delta/3$ has been introduced due to the rectangular shape of the gradients. Different shape of the gradient can also be used.

Although the CPMG echo sequence can recover the maximum signal in absence of relaxation and additionally chemical shifts are also be refocused, there are nonetheless some disadvantages. In this sequence, the transverse component of the magnetization is allowed to diffuse which brings the effect of J -modulation and T_2 relaxation. Because of the J evolution, the signal becomes distorted for spins having strong coupling interaction with other spins.

In order to reduce the contribution of transverse relaxation and J-modulation, stimulated echo pulse sequence having two or three 90^0 radiofrequency pulse was proposed.[37] The influence of diffusion on stimulated echo at steady state and the effect of pulse field gradients have been calculated .[38] In case of a stimulated echo pulse sequence the second 90^0 pulse rotates the x component of magnetization to the z-axis. The spin is then allowed to diffuse. As the longitudinal relaxation rate is comparatively smaller, relaxation-based artefacts are not introduced into the spectrum. The method, however, suffers a 50% intensity loss.

However, as for stimulated echo sequence $2\tau<<T$ and $\tau<<1/J$, this is more advantageous compared to the classical spin echo sequence.

The amplitude of pulsed-field gradient stimulated echo can be mathematically expressed as:

$$S(T+2\tau) = (M_0 / 2)\exp(-2\tau / T_2 - T / T_1)\exp[-Dq^2(\Delta - \delta / 3)] \tag{28}.$$

If the delay in the bipolar gradient (having equal strength but opposite polarity) block is smaller than the length of the gradient pulse, then the echo gets distorted due to the introduction of eddy currents. The most effective way to avoid the detrimental effect of eddy current is to prevent the formation of eddy current. This can be achieved by designing a special RF coil or by using a shaped gradient pulse.

To calculate the diffusion coefficient, gradient calibration was done. To calibrate the gradient strength, the diffusion coefficient of water was measured at a particular temperature (298K). Gradient strength was calculated by comparing the experimental and reported diffusion coefficient of water with the help of the following equation:

$$GCC_{new} = GCC_{old} \sqrt{\frac{D}{D_{literature}}} \qquad (29),$$

where, GCC refers to the gradient calibration constant and D is the diffusion co-efficient of water.

In this work stimulated echo pulse sequence was applied to measure all the diffusion coefficients. Two separate one-dimensional (1d) experiments were recorded with the lowest and highest gradient strengths for optimizing the value of the gradient pulse length and the diffusion time. With the properly adjusted value of the two parameters mentioned above, the intensity ratio between the two 1d spectra with highest and lowest gradient strength was kept approximately equal to 0.1. Later a pseudo-2D data was acquired by varying the gradient strength linearly between the highest and lowest strength. The number of transients was adjusted according to the number of steps of the phase cycle. The 2D data set was analysed using the Bruker Topspin software.

5 Temperature calibration: All the parameters that are used to characterize the efficiency of a CEST contrast agent like the exchange rate, relaxivity, and the contrast efficiency are dependent on temperature. With the increase of temperature, the exchange rate increases resulting in most situations an increase of the CEST contrast. However, at some point the exchange rate reaches its optimum value being in the slow to medium exchange regime with respect to the NMR time scale. With further increase of temperature, the CEST contrast decreases as the exchange rate exceeds the offset of the exchangeable proton. The relaxation rate constant of a nucleus also depends on

temperature. With the increase of temperature, the viscosity of the solvent decreases resulting in the reduction of rotational correlation time which in turn increases the relaxation time constants.

For temperature calibration in the range of 282 K to 330 K, 99.99% Methanol-d_4 was used as a reference. The difference of chemical shift of the methyl and hydroxyl protons of methanol is highly sensitive to temperature and follows the relationship[39]:

$$T(K) = 409.0 - 36.54\Delta\delta - 21.85(\Delta\delta)^2 \tag{30},$$

where, the difference in chemical shift is represented by $\Delta\delta$ and T represents the absolute temperature in Kelvin. The Bruker Au program '*calctemp*' was used for temperature calibration. As the chemical shift difference is calculated from the highest intensity point of a spectral line, sufficiently large number of data points should be used to avoid any digital resolution problem. However, high digital resolution makes the coupling resolved. To avoid that, the line broadening factor should be kept significantly high. The temperature correction (if any) can be included in the temperature window for reference. Importantly, the room temp, flow rate of the compressed air should not fluctuate during data collection.

Reference:

1.   Morris, G. A., Assessment of spectrometer pulse reproducibility. *Journal of Magnetic Resonance (1969)* **1988,** *78* (2), 281-291.

2.   Hoult, D. I., The NMR receiver: A description and analysis of design. *Progress in Nuclear Magnetic Resonance Spectroscopy* **1978,** *12* (1), 41-77.

3.   Wen, H.; Jaffer, F. A., An in vivo automated shimming method taking into account shim current constraints. *Magnetic resonance in medicine* **1995,** *34* (6), 898-904.

4.   Black, R. D.; Early, T. A.; Roemer, P. B.; Mueller, O. M.; Mogro-Campero, A.; Turner, L. G.; Johnson, G. A., A high-temperature superconducting receiver for nuclear magnetic resonance microscopy. *Science (New York, N.Y.)* **1993,** *259* (5096), 793-5.

5.   Crozier, S.; Brereton, I. M.; Zelaya, F. O.; Roffmann, W. U.; Doddrell, D. M., Sample-Induced RF Perturbations in High-Field, High-Resolution NMR Spectroscopy. *Journal of magnetic resonance (San Diego, Calif. : 1997)* **1997,** *126* (1), 39-47.

6.   Wider, G.; Dotsch, V.; Wuthrich, K., Self-Compensating Pulsed Magnetic-Field Gradients for Short Recovery Times. *Journal of Magnetic Resonance, Series A* **1994,** *108* (2), 255-258.

7.   McMahon, M. T.; Gilad, A. A.; Zhou, J.; Sun, P. Z.; Bulte, J. W.; van Zijl, P. C., Quantifying exchange rates in chemical exchange saturation transfer agents using the saturation time and saturation power dependencies of the magnetization transfer effect on the magnetic resonance imaging signal (QUEST and QUESP): Ph calibration for poly-L-lysine and a starburst dendrimer. *Magnetic resonance in medicine* **2006,** *55* (4), 836-47.

8.   Woessner, D. E.; Zhang, S.; Merritt, M. E.; Sherry, A. D., Numerical solution of the Bloch equations provides insights into the optimum design of PARACEST agents for MRI. *Magnetic resonance in medicine* **2005,** *53* (4), 790-9.

9.   Zhou, J.; Wilson, D. A.; Sun, P. Z.; Klaus, J. A.; Van Zijl, P. C., Quantitative description of proton exchange processes between water and endogenous and exogenous agents for WEX, CEST, and APT experiments. *Magnetic resonance in medicine* **2004,** *51* (5), 945-52.

10.   Sun, P. Z.; Zhou, J.; Huang, J.; van Zijl, P., Simplified quantitative description of amide proton transfer (APT) imaging during acute ischemia. *Magnetic resonance in medicine* **2007,** *57* (2), 405-10.

11.   Sun, P. Z.; van Zijl, P. C.; Zhou, J., Optimization of the irradiation power in chemical exchange dependent saturation transfer experiments. *Journal of magnetic resonance (San Diego, Calif. : 1997)* **2005,** *175* (2), 193-200.

12.   Li, A. X.; Hudson, R. H.; Barrett, J. W.; Jones, C. K.; Pasternak, S. H.; Bartha, R., Four-pool modeling of proton exchange processes in biological systems in the presence of MRI-paramagnetic chemical exchange saturation transfer (PARACEST) agents. *Magnetic resonance in medicine* **2008,** *60* (5), 1197-206.

13.   Sun, P. Z., Simplified and scalable numerical solution for describing multi-pool chemical exchange saturation transfer (CEST) MRI contrast. *Journal of magnetic resonance (San Diego, Calif. : 1997)* **2010,** *205* (2), 235-241.

14.   Guivel-Scharen, V.; Sinnwell, T.; Wolff, S. D.; Balaban, R. S., Detection of proton chemical exchange between metabolites and water in biological tissues. *Journal of magnetic resonance (San Diego, Calif. : 1997)* **1998,** *133* (1), 36-45.

15.   Hua, J.; Jones, C. K.; Blakeley, J.; Smith, S. A.; van Zijl, P. C. M.; Zhou, J., Quantitative description of the asymmetry in magnetization transfer effects around the water resonance in the human brain. *Magnetic resonance in medicine* **2007,** *58* (4), 786-793.

16.   Horská, A.; Spencer, G. S., Correctly accounting for radiofrequency spillover in saturation transfer experiments: application to measurement of the creatine kinase reaction rate in human forearm muscle. *Magnetic Resonance Materials in Physics, Biology and Medicine* **1997,** *5* (2), 159-163.

17.   Baguet, E.; Roby, C., Off-resonance irradiation effect in steady-state NMR saturation transfer. *Journal of magnetic resonance (San Diego, Calif. : 1997)* **1997,** *128* (2), 149-60.

18.   Baguet, E.; Roby, C., Fast Inversion-Recovery Measurements in the Presence of a Saturating Field for a Two-Spin System in Chemical Exchange. *Journal of Magnetic Resonance, Series A* **1994,** *108* (2), 189-195.

19.   Schneider, E.; Prost, R. W.; Glover, G. H., Pulsed magnetization transfer versus continuous wave irradiation for tissue contrast enhancement. *Journal of magnetic resonance imaging : JMRI* **1993,** *3* (2), 417-23.

20.   Dixon, W. T.; Ren, J.; Lubag, A. J. M.; Ratnakar, J.; Vinogradov, E.; Hancu, I.; Lenkinski, R. E.; Sherry, A. D., A concentration-independent method to measure exchange rates in PARACEST agents. *Magnetic resonance in medicine* **2010,** *63* (3), 625-632.

21.   Zhang, S.; Merritt, M.; Woessner, D. E.; Lenkinski, R. E.; Sherry, A. D., PARACEST agents: modulating MRI contrast via water proton exchange. *Acc Chem Res* **2003,** *36* (10), 783-790.

22.   Zhou, J.; Payen, J. F.; Wilson, D. A.; Traystman, R. J.; van Zijl, P. C., Using the amide proton signals of intracellular proteins and peptides to detect pH effects in MRI. *Nat Med* **2003,** *9* (8), 1085-90.

23.   Meldrum, T.; Bajaj, V. S.; Wemmer, D. E.; Pines, A., Band-selective chemical exchange saturation transfer imaging with hyperpolarized xenon-based molecular sensors. *Journal of magnetic resonance (San Diego, Calif. : 1997)* **2011,** *213* (1), 14-21.

24.   Sun, P. Z.; Benner, T.; Kumar, A.; Sorensen, A. G., Investigation of optimizing and translating pH-sensitive pulsed-chemical exchange saturation transfer (CEST) imaging to a 3T clinical scanner. *Magnetic resonance in medicine* **2008,** *60* (4), 834-41.

25.   Gutowsky, H. S.; McCall, D. W.; Slichter, C. P., Nuclear Magnetic Resonance Multiplets in Liquids. *The Journal of Chemical Physics* **1953,** *21* (2), 279-292.

26.   Gutowsky, H. S.; Saika, A., Dissociation, Chemical Exchange, and the Proton Magnetic Resonance in Some Aqueous Electrolytes. *The Journal of Chemical Physics* **1953,** *21* (10), 1688-1694.

27.   van Zijl, P. C.; Zhou, J.; Mori, N.; Payen, J. F.; Wilson, D.; Mori, S., Mechanism of magnetization transfer during on-resonance water saturation. A new approach to detect mobile proteins, peptides, and lipids. *Magnetic resonance in medicine* **2003,** *49* (3), 440-9.

28.   Mori, S.; Abeygunawardana, C.; van Zijl, P. C.; Berg, J. M., Water exchange filter with improved sensitivity (WEX II) to study solvent-exchangeable protons. Application to the consensus zinc finger peptide CP-1. *Journal of magnetic resonance. Series B* **1996,** *110* (1), 96-101.

29.   Mori, S.; Berg, J. M.; van Zijl, P. C. M., Separation of intramolecular NOE and exchange peaks in water exchange spectroscopy using spin-echo filters. *Journal of Biomolecular NMR* **1996,** *7* (1), 77-82.

30.   Sun, P. Z., Simplified quantification of labile proton concentration-weighted chemical exchange rate (k(ws)) with RF saturation time dependent ratiometric analysis (QUESTRA):

normalization of relaxation and RF irradiation spillover effects for improved quantitative chemical exchange saturation transfer (CEST) MRI. *Magnetic resonance in medicine* **2012,** *67* (4), 936-942.

31.   Zu, Z.; Janve, V. A.; Li, K.; Does, M. D.; Gore, J. C.; Gochberg, D. F., Multi-angle ratiometric approach to measure chemical exchange in amide proton transfer imaging. *Magnetic resonance in medicine* **2012,** *68* (3), 711-9.

32.   Krishnan, V. V.; Murali, N., Radiation damping in modern NMR experiments: Progress and challenges. *Progress in Nuclear Magnetic Resonance Spectroscopy* **2013,** *68*, 41-57.

33.   Schlögl, R., H. J. Tyrell, K. R. Harris: Diffusion in Liquids, A Theoretical and Experimental Study, Butterworth, London, Boston, Durban, Singapore, Sydney, Toronto, Wellington 1984. 448 Seiten, Preis: £ 40. *Berichte der Bunsengesellschaft für physikalische Chemie* **1985,** *89* (2), 209-210.

34.   Knowles, P., Biophysical Chemistry: Part II@ Techniques for the study of Biological Structure and FunctioŽ : by CR Cantor and PR Schimmel. pp 503. WH Freeman and Co, Oxford. 1980. £20.70/£10.60 (paperback). *Biochemical Education* **1981,** *9*, 157.

35.   Morris, K. F.; Johnson, C. S., Diffusion-ordered two-dimensional nuclear magnetic resonance spectroscopy. *J. Am. Chem. Soc.* **1992,** *114* (8), 3139-3141.

36.   Morris, K. F.; Johnson, C. S., Mobility ordered 2D-NMR spectroscopy. *J. Am. Chem. Soc.* **1992,** *114* (2), 776-777.

37.   Hahn, E. L., Spin Echoes. *Physical Review* **1950,** *80* (4), 580-594.

38.   Canet, D., Radiofrequency field gradient experiments. *Progress in Nuclear Magnetic Resonance Spectroscopy* **1997,** *30* (1), 101-135.

39.   Ammann, C.; Meier, P.; Merbach, A., A simple multinuclear NMR thermometer. *Journal of Magnetic Resonance (1969)* **1982,** *46* (2), 319-321.

CHAPTER 3

Tetrakis-(*N*-methyl-4-pyridinium)-porphyrin as a potential diaCEST agent

The widespread popularity of Magnetic resonance imaging (MRI) as a non-invasive tool for localized imaging technique can be attributed to a large extent to the invention of MRI contrast agents.[1] These agents are classified based on their working principle behind generating the contrast. The most common of them is the relaxation-based contrast agents[2] that shorten either longitudinal or transverse relaxation time of the solvent water. This results in contrast through enhanced intensity in T_1-weighted images[3] and reduced intensity in T_2-weighted images.[4] However, the use of lanthanide elements such as gadolinium in most of these contrast agents is a matter of grave concern. In 2008, a direct link was reported between nephrogenic systemic fibrosis in patients with renal failure and gadolinium containing MRI contrast agents.[5] Years before this report, however, the search for alternative contrast agents began leading to the introduction of Chemical Exchange Saturation Transfer (CEST) based contrast agents.[6] CEST contrast agents contain one or more exchangeable protons preferably resonating far from the bulk water and having moderate solvent exchange rates. Saturation incurred upon these protons when transferred to the bulk water through exchange, causes a reduction in effective water proton density creating contrast. This class of contrast agents is again broadly divided into two categories based on the presence (paraCEST)[7] or absence (diaCEST)[8] of a metal center. Due to the presence of a paramagnetic metal center ligated with multi-dentate ligands[9], paraCEST agents show large offset for the exchangeable peaks with respect to water necessary for good contrast efficiency.[10] The advantage of the large offset in paraCEST agents is, however, countered partly due to the fact that they still administer metal into body fluids, even though few of the recent ones contain much safer transition block metals.[11]

The diaCEST agents, on the other hand, are considered much safer as they come with no metal. Finding a diaCEST agent with efficiency comparable to their paraCEST counterparts is, however, a challenge. In the pursuit of better-performing diaCEST agents, a wide variety of compounds have already been reported over the past few years, following the first reports of barbituric acid,[12] iopamidol,[13] and several compounds belonging to Thymidine analogs.[14]

The safety aspect of CEST contrast agents prompted many to look for possible contrast agents within the large repertoire of already known 'safe' molecules. Some of them are even found in the human body in some form or the other. Important examples in this category of diaCEST agents include glucose (glucoCEST[15]), glycogens (glycoCEST),[16] glycosaminoglycan's (gag-CEST),[17] protamine,[18] and saturation transfer involving compartmentalized water of lypozomal vesicles (lipo-CEST).[19] Apart from these, myo-inositol,[20] glutamate,[21] and L-arginine[22] have also shown appreciable CEST contrast. The primary reason behind the comparatively low efficiency of diaCEST agents is the low offsets of the exchangeable protons with respect to the water. The role of the chemical shift offset is two-fold. First, an exchangeable proton resonating very close to water cannot be selectively saturated without partial direct saturation (DS) of water. Even at a low saturation RF field that creates a very narrow DS profile of water, CEST contrast efficiency drops drastically within ± 3 ppm offset range about the water resonance. Second, a large number of metabolites possessing labile protons that resonate within 1 to 3 ppm with respect to water, get co-saturated along with the contrast agent affecting the efficiency. Very recently, significant progress has been made in creating larger offsets for the exchangeable protons utilizing intramolecular hydrogen bonds in molecules such as salicylic acid,[23] phenols,[24] and imidazole.[25]

1. Porphyrins as diaCEST agents

Porphyrin is a tetra pyrrolic macrocycle that contains 16 (C/N) atoms in the inner core with 18 p-electrons in their shortest conjugated pathway and follows Hückel aromatic character.[26] The porphyrin analogs are abundant in many biological systems such as hemoglobin, chlorophyll etc. and hence is naturally considered safe. Due to this ubiquity, it is even termed as "pigments of life".[27] The four pyrrolic units are connected by four sp^2 hybridized *meso* carbon bridges and to gratify the p conjugation avenue, two pyrroles exist as imine (N) whereas, another two in the amine (NH) form. The inner core amine NHs are labile in nature and appear in the shielded region of an NMR spectrum due to diamagnetic ring current. This automatically makes free-base porphyrin a possible candidate for CEST contrast agent, provided it can be made water soluble at physiological conditions. Surprisingly, even after two decades of the introduction of CEST[6] and a plethora of other biological applications of porphyrin derivatives[28] including relaxation based MRI contrast agents,[29] only one report[30] is available in the literature where porphyrin analogs have been proposed as CEST MRI contrast agents. In that solitary report it has been shown that ionic *meso* group substituted porphyrin derivatives such as **1** in Chart 1 are well suited as diaCEST agents.[30] However, presence of the sulfonate group in the *meso* substitution makes the exchange rate (k_{ex}) of the inner core amine protons and therefore the CEST contrast efficiency of **1** highly dependent on the pH of the medium. The pH dependency is also reflected in the CEST efficiency as it drops from 25% at the acidic pH of 6.2 to less than 5% at the important physiological pH of 7.4.[30]

Here we present a different strategy for the *meso* substitution to remove such dependency of k_{ex} and hence of CEST efficiency on pH in order to prepare a diaCEST agent that works with high efficiency not only at the physiological serum pH of 7.4 at 37 °C but also in the range of pH in which most of the other human body-fluids are found.[31] The strategy involves the use of counter

anions to stabilize the positive charge on the pyridile substitutions. This way the solvent protons would interact with the counter anion, rather than with the core porphyrin moiety, making the exchange rate of the labile inner core amine protons less susceptible to changes in the medium pH. The strategy ensures, (i) good solubility both at the physiological serum pH as well as at the acidic pH below 6.5, (ii) minimal pH dependence of k_{ex} and hence appreciable CEST efficiency across a wide range of pH and finally, (iii) an easily synthesizable compound with good yield.

The compound **2** (Chart 1), prepared following the above strategy, shows appreciable nearly pH-invariant CEST contrast when the labile protons at 8 ppm upfield from bulk water are saturated. The upfield position is particularly very convenient as labile protons of other metabolites generally do not appear in that region. Additionally, the synthesis of **2** is relatively simple as all the reaction steps are established and are well-documented in the literature.[32] With an inherent safety tag, synthetic advantages, highly upfield shifted labile protons and good solubility and contrast in a wide range of pH, **2** is expected to make 'porphyrin' a biologically viable CEST MRI contrasting agent.
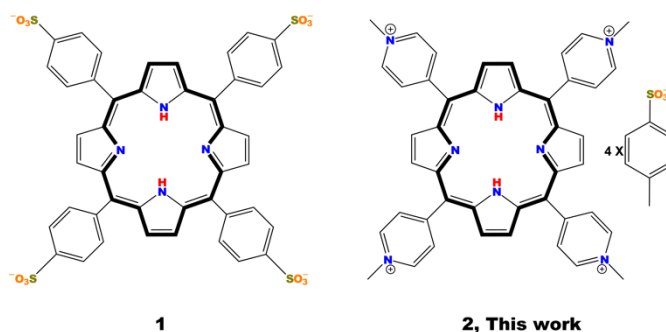
Chart 1. Chemical structures of Tetraphenylporphine sulfonate (**1**) and tetrakis-(N-methyl-4-pyridinium)-porphyrin (**2**, TmPyP). **1** has recently been proposed as a possible diaCEST agent.[30]

2. Experiments and Methods

2.1 Synthesis and characterization The compound **2** was synthesized by preparing a quaternery salt of tetrapyridylporphine, in which the *meso* pyridyl groups are N-methylated and four methyl *p*-toluenesulfonate anions act as counteranions.[32] The electronic absorption spectra of **2** acquired in DMSO is shown in Figure 1.
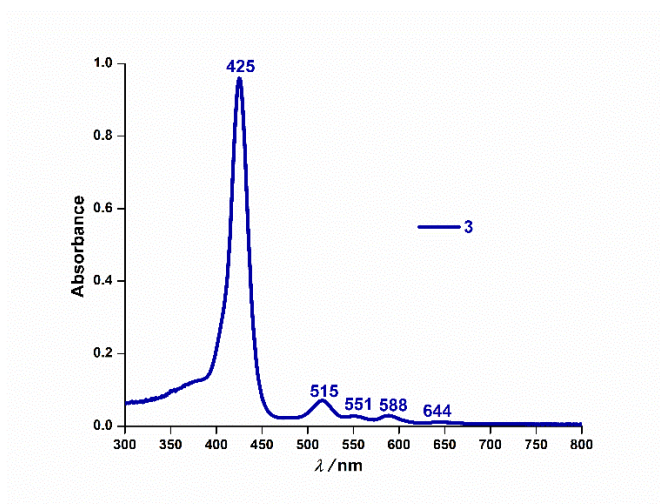
Figure 1: UV absorption spectrum of **TmPyP** in DMSO. The characteristic sharp soret band appears at 425 nm along with four weak Q bands at 515nm, 551nm, 588nm and 644nm.

Compound **2** displays one sharp Soret absorption band at 425 nm and four weak Q bands between 515 nm and 644 nm. Figures 2 and 3, respectively, show the ^{1}H and ^{13}C NMR spectra of **2** (Figure 2a). Due to the Hückel aromatic nature and high symmetry of **2**, the outer pyrrolic protons appear as a singlet at 8.79 ppm (Figure 2b, 2b-A). The *meso*-pyridyl CH protons appear as doublets at 9.025 ppm and 8.52 ppm (Figure 2b, 2b-A) and the N-methylated protons are observed at 4.70 ppm (Figure 2b, 2b-C). The phenylene protons of the counter anions appear as another set of doublets at 7.125 ppm and 6.57 ppm (Figure 2b, 2b-B), while the methyl protons are observed at 1.59 ppm (Figure 2b). All the assignments were confirmed by analyzing an ^{1}H-^{1}H 2D COSY

spectrum (Figure 2c). In general, the NH protons of heterocycles such as pyrrole resonate about 5 ppm downfield with respect to water due to the de-shielding effect of the aromatic ring current. However, in **2**, due to diatropic ring current inside the macrocyclic core, the inner NH protons shift upfield to –3.1 ppm (observed in DMSO-D6, Figure 4). This highly upfield shift can also be rationalized by the high pKa of the inner core NH protons of free-base porphyrin. The exchangeable nature of the inner-core NH was confirmed by D_2O titration (Figure 4). As deuterium is not observed in proton experiment, the intensity of the exchangeable peak reduces to a great extent upon addition of D_2O and irreversible deuterium exchange with proton.
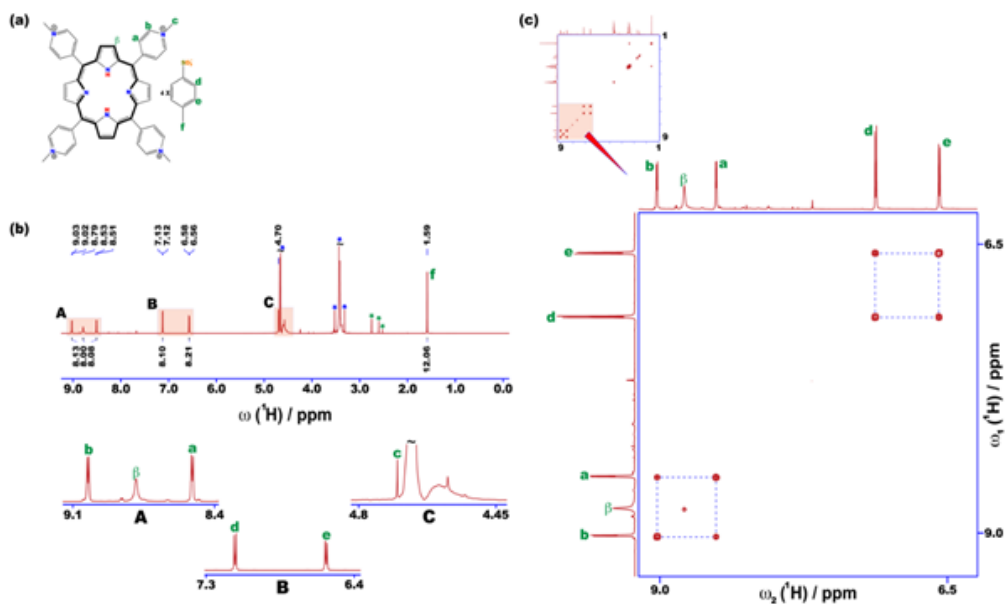
Figure 2: ^1H NMR spectra of TmPyP (a). The different non-equivalent protons of the molecule are identified in (a). (b) One dimensional (1D) ^1H spectrum of TmPyP. The peak positions in ppm and peak integration values are provided, respectively, on the top and bottom of the spectrum. Three portions of the spectrum (shaded in light pink and denoted by **A, B,** and **C**) are expanded for clarity at the bottom of the spectrum. Peaks marked by green asterisks belong to the buffer whereas those marked by blue asterisks belong to residual water after suppression and impurity grease. Peaks in (a) are assigned using the correlations provided by ^1H-^1H 2D COSY spectrum given in (b). The small portion of the 2D spectrum (shaded in light pink) containing the correlations is shown expanded for clarity. The COSY spectrum was acquired with 128 indirect and 2048 direct dimension complex points and 8 transients per indirect data point.
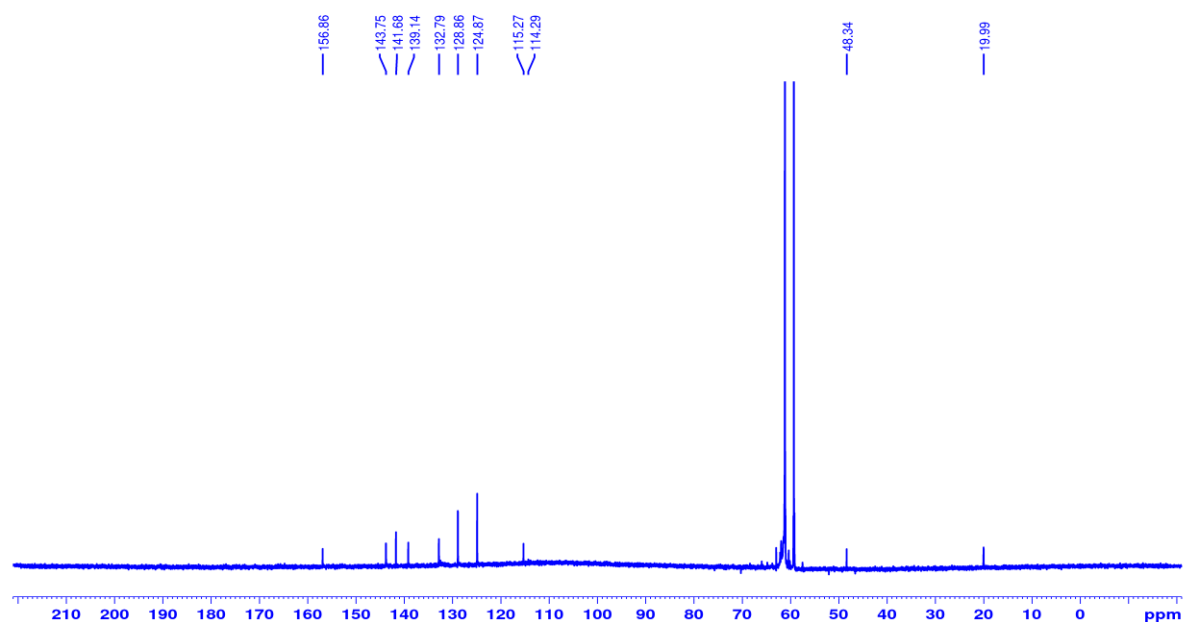
Figure 3: ^{13}C-NMR spectrum of TmPyP in DMSO-d$_6$ recorded on 700 MHz. δ 19.99, 48.34, 114.29, 115.27, 124.87, 128.86, 132.79, 139.14, 141.68, 143.75 and 156.86.
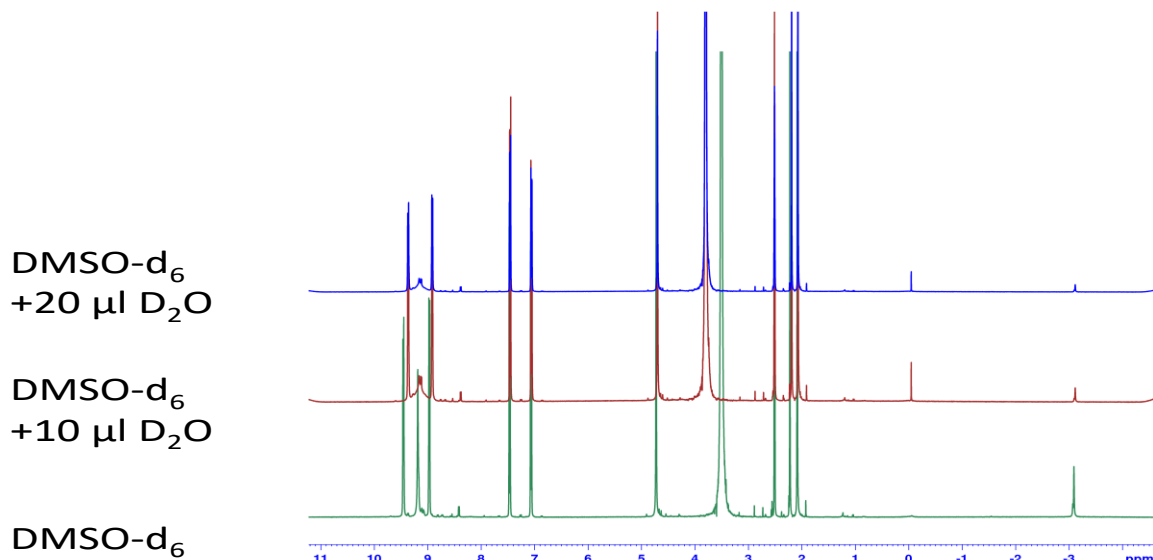
Figure 4: 1H NMR of TmPyP in DMSO-d$_6$. The inner core amine NH proton resonates at -3 ppm. Upon addition of 10µl of D$_2$O the intensity of this proton reduces and almost vanishes after the addition of another 10 µl of D$_2$O. This shows the exchangeable behavior of this inner core NH protons that are highly upfield shifted.

2.2 Sample preparation and instrumentation 12.5 mM solution of the purified compound **2** was prepared using 100 mM TRIS-HCl buffer. The pH was adjusted to eight different values ranging from 6.7 to 8.3 by using HCl (0.5 M) and NaOH (0.5 M). pH measurements prior to each NMR experiment were performed using an Eutech pH-meter at the physiological temperature of 37 °C. To confirm the efficiency of the proposed contrast agent in biological media, 12.5 mM solution of 2 was prepared by dissolving the compound in 1 ml of Foetal Bovine Serum (FBS) solution. Later the pH was adjusted to 7.4. All NMR experiments were performed at 37 °C on a 9.4 T Bruker AVANCE-III Nanobay NMR spectrometer equipped with a BBFO broadband probe. Lock was achieved by placing an external capillary filled with D_2O coaxially inside the NMR tube. Temperature Calibration was performed prior to each experiment using Methanol-D_4 standard temperature calibration sample.

2.3 Preparation of CEST z-spectra CEST experiments were carried out with 3 s saturation at a saturation RF field of 5 mT. CEST z-spectra were obtained by plotting normalized water signal $100 \times M_Z/M_0$ as a function of presaturation pulse frequency offset with respect to water. CEST effect or efficiency was calculated using the formula for asymmetric magnetization transfer ratio (MTR$_{assym}$) including the effect of any direct saturation (DS) of water given by,[33]

$$\text{CEST effect} = \frac{I(-\Delta\omega) - I(\Delta\omega)}{I(-\Delta\omega)} \times 100\% \tag{1},$$

where, $I(\Delta\omega)$ and $I(-\Delta\omega)$ are, respectively, intensities of the water peak after on-resonance saturation (at the site of the exchangeable peak, offset $\Delta\omega$ from water resonance frequency) and off-resonance saturation at the mirrored position $-\Delta\omega$. All post-acquisition processing were performed using in-house Matlab (R2014b) scripts.

2.4 Exchange rate calculation Two well-established methods[10, 34] are available for exchange rate constant determination and the choice of method depends entirely on the contrast agent and

instrument used. The first method, named QUEST[34] (or QUESP) uses exchange modified Bloch equations to non-linearly fit MTR$_{assym}$ data as a function of either saturation time or saturation power. This method inherently takes care of any non-zero DS. The other method that uses a simpler linear regression instead, was proposed by Dixon *et al.*[10] The method is, however, applicable only if DS is negligible, the offset $\Delta\omega$ is more than the RF powers (in Hz) used for the experiments and complete saturation of the contrast agent is achieved. To ensure that these conditions are satisfied, the experiments for exchange rate measurement were performed using long saturation duration with carefully chosen RF powers taking the offset into consideration and opting for a sinc shaped pulse for irradiation to achieve low DS.

The procedure goes by measuring two water signal intensities immediately after long irradiations once on-resonance (M_Z) and once off-resonance (M_0) at varied irradiation RF field strength (B_1). According to the theory, a linear plot of the quantity $M_Z/(M_0 - M_Z)$ as a function of $1/\omega_1^2 = 1/(\gamma B_1)^2$ gives the exchange constant (k_{ex}) from the intercept on the x-axis as $[1/\omega_1^2]_{intercept} = -1/(k_{ex})^2$. For the measurement of k_{ex} for **2**, long 6 s saturation was used at variable RF field strengths between 5 µT to 15 µT. The data was plotted and fitted (linear) in Microsoft Excel with high correlation coefficient $R^2 > 0.999$.

2.5 Relaxivity measurements. Longitudinal (R$_1$) and transverse (R$_2$) relaxation rate constants of water were determined in presence and absence of the contrast agent. R$_1$ was measured using the inversion recovery method[35] with 12 variable delays ranging from 10 ms to 6 s. CPMG[35] was employed to determine R$_2$ with 14 variable delays ranging between 80 ms and 1.44 s. The relaxivities were calculated as the concentration normalized change in R$_1$ or R$_2$ of water due to the presence of the contrast agent.

3. Results and discussion

Figure 5a shows the overlaid CEST z-spectra of **2** at the physiological condition in the buffer and in Foetal Bovine Serum (FBS) titrated to physiological pH. In both media, **2** shows an appreciable CEST efficiency of ~15%. Figure 5b shows the CEST efficiency as a function of saturation duration. As expected the efficiency increases with saturation period first and then saturates (around 6 s at 18%). It is interesting to note that with even 2 s saturation **2** shows over 13% CEST efficiency.
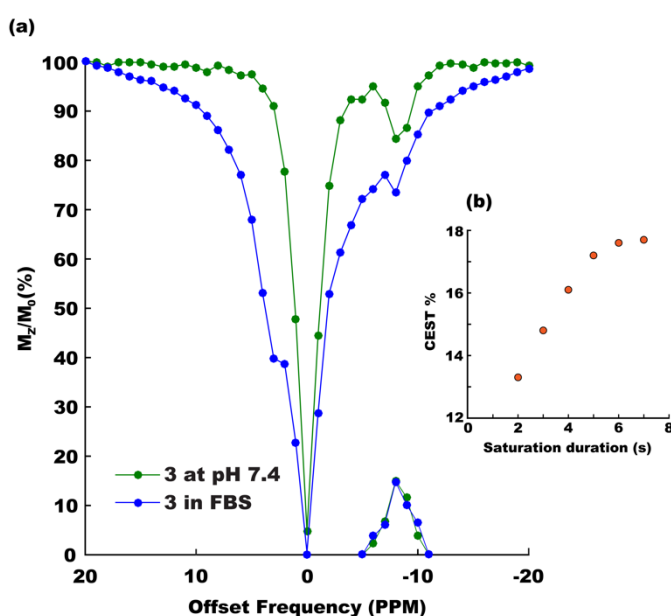
Figure 5 (a) Overlaid CEST spectra of 12.5 mM solution of Tetrakis-(N-methyl-4-pyridinium)-Porphyrin (**2** in Chart 1) in 100 mM TRIS-HCl buffer (green) and FBS (blue) at the physiological pH (7.4) and temperature (37 °C). The experiments were performed using 3 s saturation at 5 mT RF field strength. The corresponding DS subtracted CEST peaks are plotted on the x-axis. (b) CEST efficiency (MTR$_{assym}$, Eq. 1) of **2** as a function of saturation duration (RF field 5 mT) at the physiological condition.

Considering a two pool exchange model where the concentration of the solvent is several orders higher than that of the solute, the effective exchange rate is governed by the rate at which the protons escape the solute pool instead of the other way round.[36] The interrelationship between the frequency offset of the exchangeable protons ($\Delta\omega$) and the exchange rate (k_{ex}) is pivotal in

determining the CEST efficiency. Moreover, the bound water lifetime that is directly related to k_{ex} plays a crucial role in determining the optimum saturation power and duration for maximizing CEST efficiency.[10] For good CEST contrast, the exchange rate should not ideally be greater than the offset ($k_{ex} \leq \Delta\omega$).[33, 37] The exchange rate was measured using the method proposed by Dixon *et al.* with long 6 s saturation to ensure complete saturation (taking a cue from Figure 5b), maximum RF strength of 639 Hz (15 µT) which is lower than the chemical shift offset of 3202.4 Hz at 9.3 T. DS was measured to be less than 2% with this setup. Figure 6a shows the z-spectra recorded for different RF strengths (5 µT to 15 µT) at pH 7.4.
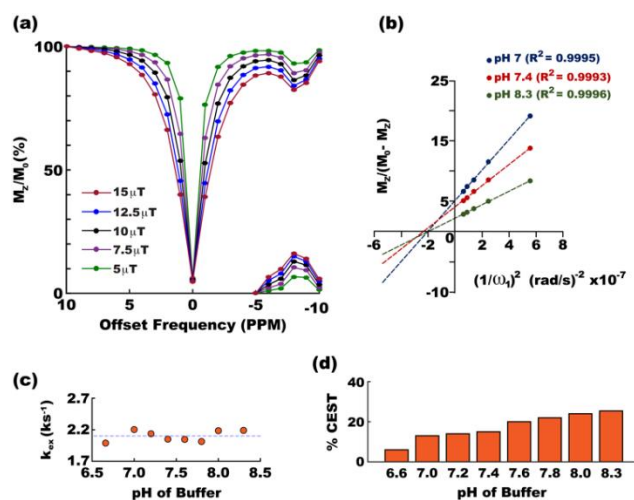
Figure 6: Calculation of exchange rate constant (k_{ex}) and CEST contrast of **2** as a function of buffer pH. (a) Overlaid CEST spectra and corresponding DS subtracted CEST peaks at pH 7.4 for five different RF field strengths ranging from 5 µT to 15 µT. (b) The linear fit for $M_Z/(M_0 - M_Z)$ as a function of $1/\omega_1^2$ for three pH values, 7, 7.4, and 8.3. For the other pH values please refer to Figures. 7-11. (c) k_{ex} as a function of pH. The dotted line indicates the average k_{ex}. (d) CEST effect as a function of buffer pH with 3 s saturation at 5 µT RF field. (see Figure. 12 for corresponding z-spectra).

The linear relationship expected for $M_Z/(M_0 - M_Z)$ as a function of $1/\omega_1^2$ is shown in Figure 6b for three pH values of 7, 7.4 and 8.3. k_{ex} of **2** at the physiological pH and temperature was measured to be 2.05± 0.23 ks⁻¹, which is smaller than the chemical shift offset as desired. Additionally, the slow to medium exchange regime in the NMR time scale makes **2** a perfect candidate as CEST agent.

The pH dependence of the exchange rate was also studied and is shown in Figure. 6c. The exchange rate did not show any particular increasing or decreasing pattern with increasing pH, but rather fluctuated around an average value of 2.1 ks^{-1}.

The fact that the exchange rate constant is nearly independent of pH is reflected also in the CEST percentage profile which showed only a gentle positive ramp against the change of pH (Figure. 6d).

Dependence of CEST percentage on saturation field strength and the CEST profile of TmPyp with varying pH is shown in figure 7-12.

Figure 7: Dependence of CEST percentage on saturation field strength ranging from 5 µT to 15 µT for (a) pH =7.0 and (b) pH=7.2.In order to have complete saturation of the exchangeable proton Radiofrequency saturation was applied for 6s .water direct saturation profile was less then 2% with the highest radiofrequency saturation power.
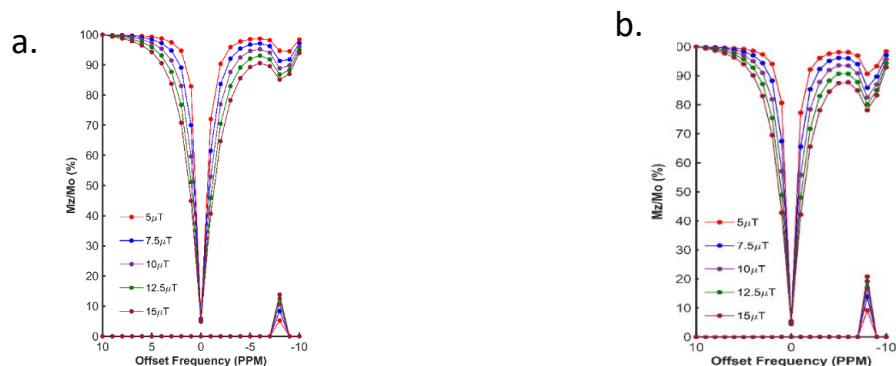
Figure 8: Dependence of CEST percentage on saturation field strength ranging from 5 µT to 15 µT for (a) pH =7.4 and (b) pH=7.6 saturation was applied for 6s ensuring complete saturation of exchangeable proton. Water direct saturation was less than 2% with the highest radiofrequency saturation power.
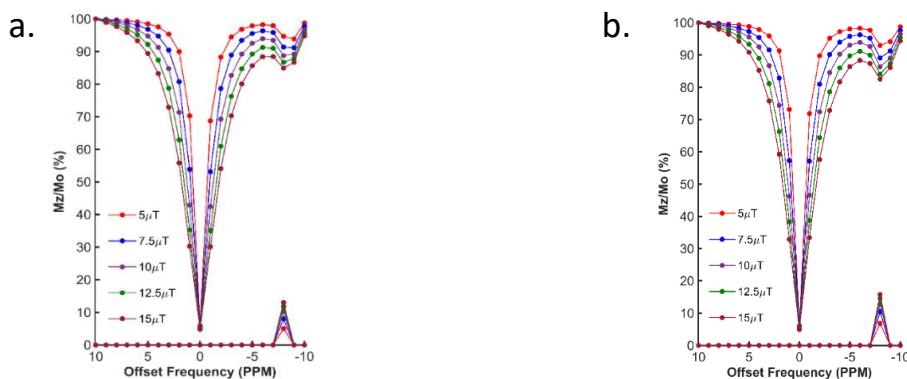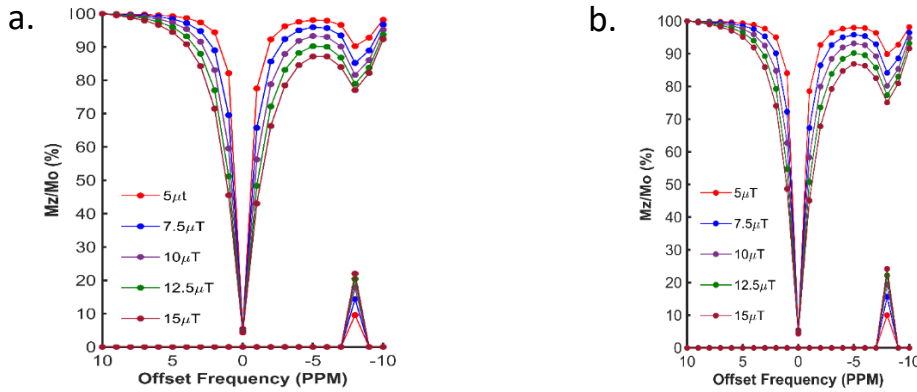
Figure 9: Dependence of CEST percentage on saturation field strength ranging from 5 µT to 15 µT for (a) pH =7.8 and (b) pH=8 RF saturation was applied for 3s with saturation RF field varying from 5 µT to 15 µT.
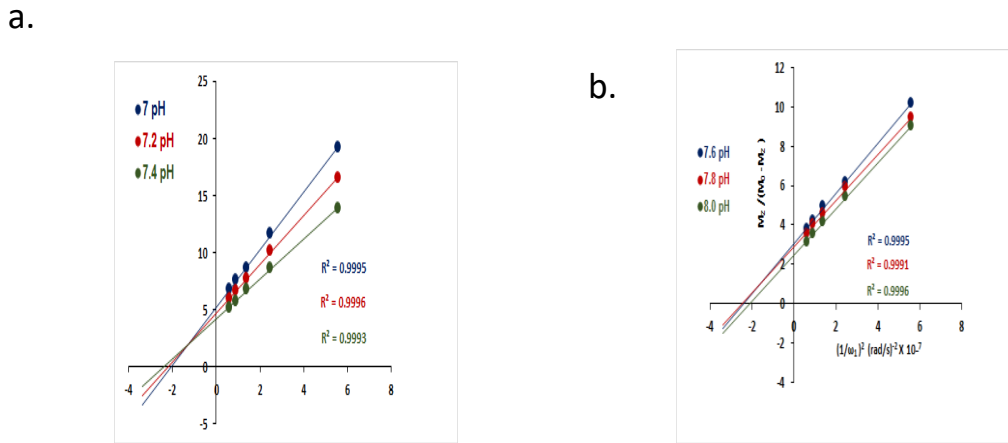
Figure 10: Omega plot for exchange rate measurement of **TmPyP** in buffered medium at (a) pH 7.0 to pH 7.4 and (b) pH 7.6 to pH 8.0. The desired linear relationship of $M_z/(M_0-M_z)$ as a function of $1/\omega_1^2$ (rad/sec)$^{-2}$ x 10^{-7} was obtained.

Figure 11 : (a) Dependence of CEST percentage on saturation field strength ranging from 5 µT to 15 µT for 8.3 pH (b) Omega plot for exchange rate measurement for pH 8.3. The expected linear relationship of $M_z/(M_0-M_z)$ as a function of $1/\omega_1^2$ (rad/sec)$^{-2}$ x 10^{-7} was obtained at 9.4 T of 12.5 mM compound in 0.1M Tris-HCl buffer. RF presaturation pulse was applied for 6 s ensuring complete saturation.

a.

b.
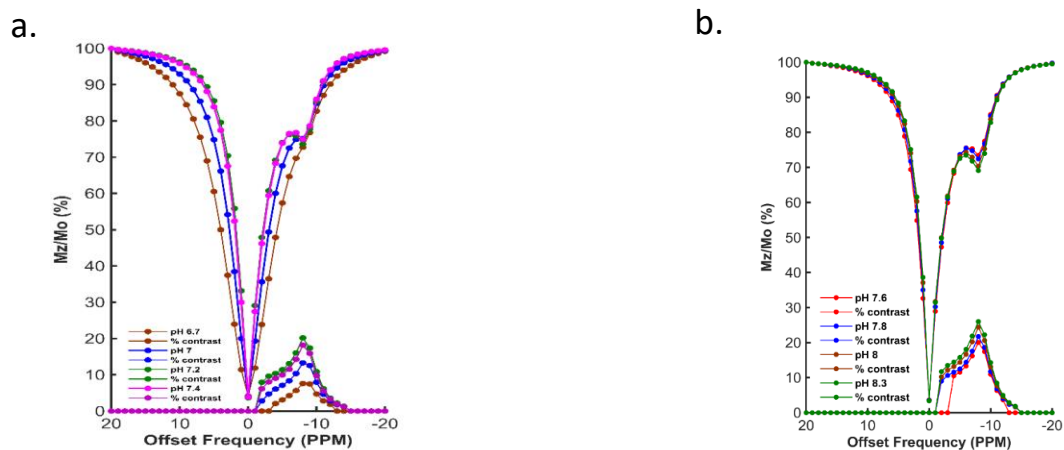
Figure 12: Dependence of CEST effect of TmPyP on pH. (a) Overlaid Z-spectra with pH ranging from 6.7 to 7.4. (b) Overlaid Z-spectra with pH ranging from 7.6 to 8.3. Radiofrequency saturation was applied for 3s with a saturation radiofrequency of 5 μT.

Moreover, the favorable exchange rate at the physiological condition (pH 7.4 and 37 °C) resulted in an appreciable CEST effect of 15% with 3 s saturation. To further test the potential of **2** as a contrast agent in biological media, k_{ex} was measured also in FBS. The exchange rate constant in FBS was measured as 1.49 ± 0.19 ks^{-1}, which is again in the favorable regime (Figure.13).

The primary advantage of any diaCEST agents is the absence of a metal center, but in **2** a possible occurrence of metal binding at the axial site of free-base porphyrin when injected into the body fluid cannot be overruled. The tetrapyrrole macrocyclic core of the porphyrin unit is an ideal
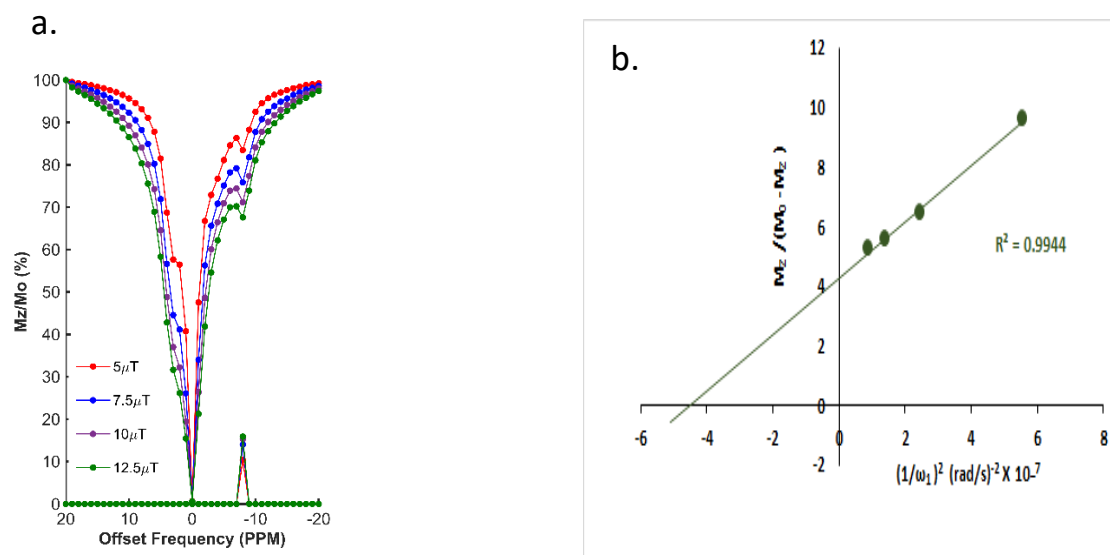
Figure 13 : (a) Dependence of CEST percentage on saturation field strength ranging from 5 µT to 12.5 µT for FBS at 7.4 pH (b) Omega plot for exchange rate measurement. The expected linear relationship of $M_z/(M_0-M_z)$ as a function of $1/\omega_1^2$ (rad/sec)$^{-2}$ x 10^{-7} recorded at 9.4 T of 12.5 mM TmPyP in Foetal bovine serum at pH 7.4. RF presaturation pulse was applied for 6 s ensuring complete saturation.

 In such cases, the exchangeable protons responsible for showing the CEST contrast get displaced by the metal ion and the CEST peak simply disappear. In order to be assured that such metal ligation does not happen with **2**, we have performed CEST experiments by adding 1eq of $ZnCl_2$ to the buffer solution of **2** and monitored for any possible quench of the CEST peaks. Considering the fact that the metal ligation might be thermodynamically favorable in a base catalyzed situation, we performed the experiments with the mixture at basic as well as at neutral pH. After the addition of the metal salt with a 12.5 mM solution of **2**, pH was maintained using a strong acid/base without disturbing the molar equivalence of the free base porphyrin as well as the metal salt. The experiment with basic pH was recorded twice, first after 4 h and then after 12 h of incubation at 37 °C. For the neutral pH, 12 h incubation was employed. In none of the cases, quench in the CEST effect was observed (Figure 14a-b).
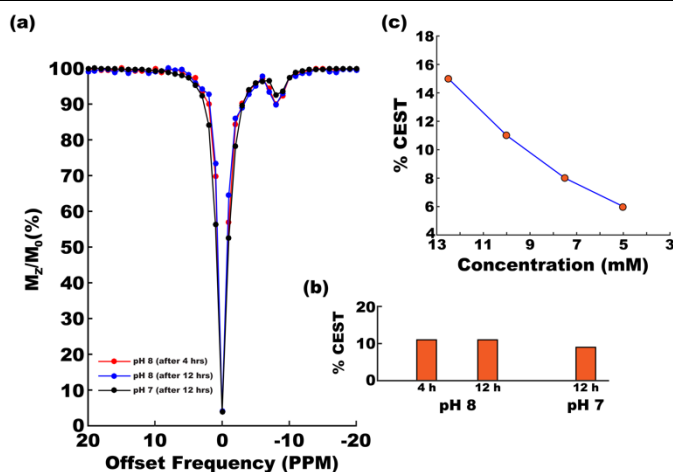
Figure 14: Titration of 12.5 mM of **2** in buffer with 1eq of $ZnCl_2$. (a) Overlaid z-spectra of **2** acquired after 12 h incubation at pH 7 (black), 4 h (orange), and 12 h (blue) incubation at pH 8 and (b) corresponding CEST efficiencies. (c) CEST efficiency as a function of concentration in the range of 5 mM to 12.5 mM with 5 μT RF field and 3 s saturation duration.

Although porphyrin moieties are products of physiological metabolism, administration of any contrast agent beyond a certain concentration level is not advisable. CEST experiment was, therefore, carried out at 4 different concentrations to check the drop in the CEST effect with the decreasing concentration (Figure. 14c). At the minimum concentration of study (5 mM) the CEST percentage was recorded to be 6% at 5 mT saturation field strength with 3 s saturation duration.

Finally, CEST contrast agents are expected to show very negligible relaxivity. **2** showed, as desired, nominal relaxivities of 0.03 $Hz.mmol^{-1}$ (R_1 relaxivity) and 0.01 $Hz.mmol^{-1}$ (R_2 relaxivity). These small relaxivities along with the fact that **2** remains fairly water soluble also at the acidic pH of 6.5 and lower suggest **2** a potential candidate for *in-vivo* applications as a diaCEST agent.

4. Conclusions

In summary, we have shown that tetrakis-(*N*-methyl-4-pyridinium)-porphyrin (**2**, TmPyP in Chart 1) as a potential diaCEST MRI contrast agent that shows an appreciable 15% CEST effect at physiological condition both in the buffer and in the FBS. Further, it maintains a nearly constant

contrast efficiency (average 18%) in the pH range of 6.6 to 8.3 in which different human body fluids are naturally found. Also, the compound remains soluble in water both at the physiological as well as at the acidic pH and hence is suitable for *in-vivo* applications. Although there is a class of paramagnetic molecules that contain upfield shifted labile protons, in general, their very high exchange rate makes them unsuitable for CEST.[38] The fact that the exchange rate of TmPyP lies in a favorable range and is nearly independent of pH near the physiological pH makes it a nice system as a CEST contrast agent. We believe this study would make porphyrin a step closer to be used as a potential diaCEST agent.

References

1. Y.-D. Xiao, R. Paudel, J. Liu, C. Ma, Z.-S. Zhang and S.-K. Zhou, *Int. J. Mol. Med.*, 2016, **38**, 1319-1326.

2. P. Caravan, J. J. Ellison, T. J. McMurry and R. B. Lauffer, *Chem. Rev.*, 1999, **99**, 2293-2352.

3. J. B. Livramento, L. Helm, A. Sour, C. O'Neil, A. E. Merbach and É. Tóth, *Dalton Trans.*, 2008, DOI: 10.1039/B717390C, 1195-1202.

4. F. Ye, S. Laurent, A. Fornara, L. Astolfi, J. Qin, A. Roch, A. Martini, M. S. Toprak, R. N. Muller and M. Muhammed, *Contrast Media Mol. Imaging*, 2012, **7**, 460-468.

5. C. Rydahl, H. S. Thomsen and P. Marckmann, *Invest. Radiol.*, 2008, **43**, 141-144.

6. K. M. Ward, A. H. Aletras and R. S. Balaban, *J. Magn. Reson.*, 2000, **143**, 79-87.

7. (a) M. Woods, D. E. Woessner and A. D. Sherry, *Chem. Soc. Rev.*, 2006, **35**, 500-511; (b) S. Viswanathan, Z. Kovacs, K. N. Green, S. J. Ratnakar and A. D. Sherry, *Chem. Rev.*, 2010, **110**, 2960-3018.

8.   K. W. Y. Chan, J. W. M. Bulte and M. T. McMahon, *WIREs Nanomed. and Nanobiotechnol.*, 2014, **6**, 111-124.

9.   (a) P. B. Tsitovich, J. M. Cox, J. A. Spernyak and J. R. Morrow, *Inorg. Chem.*, 2016, **55**, 12001-12010; (b) P. J. Burns, J. M. Cox and J. R. Morrow, *Inorg. Chem.*, 2017, **56**, 4545-4554.

10. W. T. Dixon, J. Ren, A. J. M. Lubag, J. Ratnakar, E. Vinogradov, I. Hancu, R. E. Lenkinski and A. D. Sherry, *Magn. Reson. Med.*, 2010, **63**, 625-632.

11.   (a) R. N. Pradhan, S. Chakraborty, P. Bharti, J. Kumar, A. Ghosh and A. K. Singh, *Dalton Trans.*, 2019, **48**, 8899-8910; (b) P. B. Tsitovich, J. M. Cox, J. B. Benedict and J. R. Morrow, *Inorg. Chem.*, 2016, **55**, 700-716.

12. K. W. Chan, T. Yu, Y. Qiao, Q. Liu, M. Yang, H. Patel, G. Liu, K. W. Kinzler, B. Vogelstein, J. W. Bulte, P. C. van Zijl, J. Hanes, S. Zhou and M. T. McMahon, *J. Control. Release*, 2014, **180**, 51-59.

13.   (a) S. Aime, L. Calabi, L. Biondi, M. De Miranda, S. Ghelli, L. Paleari, C. Rebaudengo and E. Terreno, *Magn. Reson. Med.*, 2005, **53**, 830-834; (b) D. L. Longo, W. Dastrù, G. Digilio, J. Keupp, S. Langereis, S. Lanzardo, S. Prestigio, O. Steinbach, E. Terreno, F. Uggeri and S. Aime, *Magn. Reson. Med.*, 2011, **65**, 202-211; (c) D. L. Longo, P. Z. Sun, L. Consolino, F. C. Michelotti, F. Uggeri and S. Aime, *J. Am. Chem. Soc.*, 2014, **136**, 14333-14336.

14.   (a) A. Bar-Shir, G. Liu, Y. Liang, N. N. Yadav, M. T. McMahon, P. Walczak, S. Nimmagadda, M. G. Pomper, K. A. Tallman, M. M. Greenberg, P. C. M. van Zijl, J. W. M. Bulte and A. A. Gilad, *J. Am. Chem. Soc.*, 2013, **135**, 1617-1624; (b) A. Bar-Shir, G. Liu, M. M. Greenberg, J. W. M. Bulte and A. A. Gilad, *Nat. Protoc.*, 2013, **8**, 2380-2391.

15. (a) K. W. Y. Chan, M. T. McMahon, Y. Kato, G. Liu, J. W. M. Bulte, Z. M. Bhujwalla, D. Artemov and P. C. M. van Zijl, *Magn. Reson. Med.*, 2012, **68**, 1764-1773; (b) S. Walker-Samuel, R. Ramasawmy, F. Torrealdea, M. Rega, V. Rajkumar, S. P. Johnson, S. Richardson, M. Gonçalves, H. G. Parkes, E. Arstad, D. L. Thomas, R. B. Pedley, M. F. Lythgoe and X. Golay, *Nat. Med.*, 2013, **19**, 1067-1072.

16. P. C. van Zijl, C. K. Jones, J. Ren, C. R. Malloy and A. D. Sherry, *Proc. Natl. Acad. Sci. U. S. A.*, 2007, **104**, 4359-4364.

17. W. Ling, R. R. Regatte, G. Navon and A. Jerschow, *Proc. Natl. Acad. Sci. U. S. A.*, 2008, **105**, 2266.

18. A. Bar-Shir, G. Liu, K. W. Y. Chan, N. Oskolkov, X. Song, N. N. Yadav, P. Walczak, M. T. McMahon, P. C. M. van Zijl, J. W. M. Bulte and A. A. Gilad, *ACS Chem. Biol.*, 2014, **9**, 134-138.

19. (a) S. Maruyama, J. Ueda, A. Kimura and K. Murase, *Magn. Reson. Med. Sci.*, 2016, **15**, 324-334; (b) G. Liu, M. Moake, Y.-e. Har-el, C. M. Long, K. W. Y. Chan, A. Cardona, M. Jamil, P. Walczak, A. A. Gilad, G. Sgouros, P. C. M. van Zijl, J. W. M. Bulte and M. T. McMahon, *Magn. Reson. Med.*, 2012, **67**, 1106-1113.

20. (a) M. Haris, K. Cai, A. Singh, H. Hariharan and R. Reddy, *Neuroimage*, 2011, **54**, 2079-2085; (b) M. Haris, A. Singh, K. Cai, K. Nath, R. Crescenzi, F. Kogan, H. Hariharan and R. Reddy, *J. Neurosci. Methods*, 2013, **212**, 87-93.

21. K. Cai, M. Haris, A. Singh, F. Kogan, J. H. Greenberg, H. Hariharan, J. A. Detre and R. Reddy, *Nat. Med.*, 2012, **18**, 302-306.

22. K. W. Y. Chan, G. Liu, X. Song, H. Kim, T. Yu, D. R. Arifin, A. A. Gilad, J. Hanes, P. Walczak, P. C. M. van Zijl, J. W. M. Bulte and M. T. McMahon, *Nat. Mater.*, 2013, **12**, 268-275.

23. X. Yang, X. Song, Y. Li, G. Liu, S. Ray Banerjee, M. G. Pomper and M. T. McMahon, *Angew. Chem. Int. Ed.*, 2013, **52**, 8116-8119.

24. X. Yang, N. N. Yadav, X. Song, S. Ray Banerjee, H. Edelman, I. Minn, P. C. M. van Zijl, M. G. Pomper and M. T. McMahon, *Chem. Eur. J.*, 2014, **20**, 15824-15832.

25. X. Yang, X. Song, S. Ray Banerjee, Y. Li, Y. Byun, G. Liu, Z. M. Bhujwalla, M. G. Pomper and M. T. McMahon, *Contrast Media Mol. Imaging*, 2016, **11**, 304-312.

26. J. I. Wu, I. Fernández and P. v. R. Schleyer, *J. Am. Chem. Soc.*, 2013, **135**, 315-321.

27. A. R. Battersby, C. J. R. Fookes, G. W. J. Matcham and E. McDonald, *Nature*, 1980, **285**, 17-21.

28.   (a) J. Králová, Z. Kejík, T. Bříza, P. Poučková, A. Král, P. Martásek and V. Král, *J. Med. Chem.*, 2010, **53**, 128-138; (b) B. Babu, R. C. Soy, J. Mack and T. Nyokong, *New J. Chem.*, 2020, **44**, 11006-11012; (c) B. Hou, Z. Li, Q. Zhang, P. Chen and J. Liu, *New J. Chem.*, 2020, **44**, 15387-15395; (d) M. Managa, B. P. Ngoy and T. Nyokong, *New J. Chem.*, 2019, **43**, 4518-4524.

29. W. Cheng, I. E. Haedicke, J. Nofiele, F. Martinez, K. Beera, T. J. Scholl, H.-L. M. Cheng and X.-a. Zhang, *J. Med. Chem.*, 2014, **57**, 516-520.

30. X. Zhang, Y. Yuan, S. Li, Q. Zeng, Q. Guo, N. Liu, M. Yang, Y. Yang, M. Liu, M. T. McMahon and X. Zhou, *Magn. Reson. Med.*, 2019, **82**, 577-585.

31. G. K. Schwalfenberg, *J. Environ. Public Health*, 2012, **2012**, 727630-727630.

32. R. F. Pasternack, P. R. Huber, P. Boyd, G. Engasser, L. Francesconi, E. Gibbs, P. Fasella, G. Cerio Venturo and L. d. Hinds, *Journal of the American Chemical Society*, 1972, **94**, 4511-4517.

33. G. Liu, X. Song, K. W. Y. Chan and M. T. McMahon, *NMR Biomed.*, 2013, **26**, 810-828.

34. M. T. McMahon, A. A. Gilad, J. Zhou, P. Z. Sun, J. W. M. Bulte and P. C. M. van Zijl, *Magn. Reson. Med.*, 2006, **55**, 836-847.

35. C. J. Cavanagh, W. J. Fairbrother, A. G. Palmer III, M. Rance and N. J. Skelton, *Protein NMR spectroscopy : principles and practice*, Academic Press, Amsterdam ; Boston, 2nd edn., 2007.

36. I. Hancu, W. T. Dixon, M. Woods, E. Vinogradov, A. D. Sherry and R. E. Lenkinski, *Acta Radiol.*, 2010, **51**, 910-923.

37. D. D. Castelli, E. Terreno, D. Longo and S. Aime, *NMR Biomed.*, 2013, **26**, 839-849.

38. S. Aime, A. Barge, D. Delli Castelli, F. Fedeli, A. Mortillaro, F. U. Nielsen and E. Terreno, *Magn. Reson. Med.*, 2002, **47**, 639-648.

CHAPTER 4

Paracetamol and other acetanilide analogs as intermolecular hydrogen bonding assisted diaCEST agent

In any diagnostic imaging technique such as Magnetic Resonance Imaging (MRI)[1] or Computed Tomography (CT)[2] scan it is always desired that the region of interest remains at a different contrast level than the surroundings. In MRI, differential water proton density or water content is the source of natural contrast that becomes useful in studying, for example, bones embedded in soft tissues. Also, in T_1 or T_2 weighted MRI imaging, the relaxation time constants of water produce natural contrast. However, in absence of such natural contrast due to similar water content of the study region and the surroundings or due to unfavorable relaxation rates, artificial contrast is achieved through chemical MRI contrast agents[3] following the seminal work by Young *et al.[4]* Traditional paramagnetic metal-containing contrast agents bring contrast by altering either the longitudinal or the transverse relaxation rate constants of the water molecules.[3a, 5] In the year 2000, Ward *et al.* introduced a new class of compounds, that produces contrast by partially saturating the water through Chemical Exchange Saturation Transfer (CEST).[6] In particular, the CEST contrast agents contain one or more labile protons that are saturated using a low power continuous irradiation immediately prior to the MRI signal detection. The saturated labile protons then, in turn, transfer the saturation through multiple exchange events with the solvent during the long continuous irradiation. It is quite obvious that the CEST efficiency improves with increasing exchange rate (k_{ex}) of a labile proton.[7] However, if the exchange becomes too fast on the NMR time scale, that is if k_{ex} becomes larger than the offset ($\Delta\omega$) of resonance frequency of a labile proton from the bulk water, then the CEST efficiency starts dropping again. For optimum CEST effect, the exchange rate should be as high as possible as long as it remains in the slow to medium exchange regime ($k_{ex} \leq \Delta\omega$) to avoid coalescence.[7a] Naturally, constant efforts are being made in the search of molecules having labile protons with

$\Delta\omega$ as large as possible, so that faster-exchanging protons can take part in the CEST to improve the CEST efficiency.

A class of CEST agents known as the paraCEST[8] agents, achieves $\Delta\omega$ of the order of several kilohertz through paramagnetic downfield shift in the presence of a metal center. However, the presence of a metal center raises safety concerns.[9] Diamagnetic CEST agents[10] (diaCEST), on the other hand, are considered comparatively safer in absence of any metal center but produces a much lower $\Delta\omega$ (typically less than 5 ppm) and hence inferior CEST efficiency. Recently, two classes of diaCEST agents were reported that produce comparatively larger offsets and hence much higher CEST contrast by utilizing, respectively, intramolecular hydrogen bonding and diatropic ring currents. Some benzoic acid derivatives (salicylic[11] and anthranilic[12] acids, in particular), phenols[13] and modified imidazole[14] compounds belong to the first class of molecules in which intramolecular hydrogen bonding (will be referred as intraMHB hereon for brevity) shifts the labile proton responsible for CEST contrast downfield (as large as 9.3 ppm for salicylic acid). Certain *meso*-substituted porphyrin derivatives, on the other hand, form the second class of diaCEST agents in which the diatropic ring current produced by the conjugated π-electrons brings a large upfield shift (~ 8 ppm) to the labile inner-core amine protons.[15]

1. Amides as diaCEST agent

We introduce in this chapter a few amide (acetanilide, in particular) derivatives as a new class of diaCEST agents, that produces comparable contrast as the previous two classes in spite of the fact that they do not show a similar large shift. Amide is already a popular choice[12, 16] for diaCEST agents as amides are found in various natural products, drugs and biomolecules and hence is considered in general non-toxic.[17] The amide moiety however plays an additional role as the core structural motif for the contrast agents presented here. Amides are known from a long time to form

intra as well inter-molecular hydrogen bonds.[18] The compounds we present here as diaCEST agents do not exhibit contrast as an individual entity due to very fast exchange of their labile protons but do so only when they form 'intermolecular hydrogen bonding (interMHB for brevity)' mediated molecular chains or sheets. The interMHB helps to bring the exchange rate down to a favorable slow to medium exchange regime. In other words, the molecules act as a CEST contrast agent only as a group. We show this interesting behavior through a number of variable temperature experiments. We demonstrate that under mild heating above the physiological temperature when the interMHB chains start breaking, the isolated molecules cease to contribute to observable contrast as then the exchange rate breaches the slow to medium exchange regime ($k_{ex} \leq \Delta\omega$). Although the weaker intrerMHB cannot produce as spectacular $\Delta\omega$ as is produced by the much stronger intraMHB or the intense diatropic ring current, it slows down the exchange rate very optimally. For example, paracetamol (acetaminophen), a well-known analgesic drug[19] and a notable member of this proposed class of CEST agents shows $\Delta\omega$ of only 4.68 ppm, but yet it produces nearly similar contrast efficiency as compared to that shown by salicylic acid. The interMHB plays here the crucial role of optimizing the interplay between $\Delta\omega$ and k_{ex} which is pivotal for any good CEST MRI contrast agent.

2. Experiments and Methods

2.1 Synthesis and characterization. Acetanilide and substituted anilines were purchased from Sigma-Aldrich and were used without further purification. Other acetanilide derivatives (Table 1) were synthesized from the respective commercially available substituted aniline precursors following literature procedure.[20] Acetic anhydride (12.7 mmol) was added to the aniline precursors (10 mmol) suspended in water (3 mL). The mixture was vigorously stirred in a warm water bath.

Once the solid particles got dissolved, the reaction mixture was cooled. The solid product was then filtered and washed with cold water. The solid acetyl derivatives were finally recrystallized from hot water and dried at ambient conditions. All the synthesized compounds were characterized using ^1H and ^{13}C 1D NMR spectra acquired in DMSO-d_6 as the solvent.

2.2 Sample preparation and instrumentation: 15 mM solutions of acetanilide and its derivatives were prepared using 10 mM (1X) PBS buffer. For the pH dependent studies seven samples were prepared with pH values ranging between 6.8 and 8.1 by using 0.5 M HCl and 0.5 M NaOH solutions. pH measurements were performed using a Hanna HI2210 pH-meter. All experiments were performed at the physiological temperature of 37 °C unless mentioned otherwise. For CEST studies in the biological media, 15 mM solutions at pH 7.4 were prepared by dissolving the necessary compounds in 1 ml of either 4% Fetal Bovine Serum (FBS) or 4% Horse Serum (HS) solution. All NMR experiments were performed on a 9.4 T Bruker AVANCE-III Nanobay NMR spectrometer equipped with a BBFO broadband probe, except for the exchange constant determination experiments. Exchange constants were calculated from experiments acquired on a 16.4 T Bruker AVANCE-III AV700 Ascend spectrometer equipped with a triple resonance room temperature probe. D$_2$O filled capillaries were placed coaxially inside the NMR tube for deuterium lock. Methanol-D$_4$ was used for temperature calibration using standard procedure.

2.3 Preparation of CEST z-spectra. CEST experiments were carried out with r.f. irradiation at 213 Hz (5mT) field strength for 3 s. Data were collected at 1 ppm interval and normalized water peak intensity ($100 \times M_Z/M_0$) was plotted against irradiation offset frequency to obtain the CEST z-spectra. M_Z and M_0 denote the water peak intensities, respectively, with and without on-

resonance (on the solute exchangable peak) saturation. CEST contrast or efficiency was calculated from the asymmetric magnetization transfer ratio (MTR$_{assym}$) given by,[7c]

$$\text{CEST efficiency} = \frac{M(-\Delta\omega) - M(\Delta\omega)}{M(-\Delta\omega)} \times 100\% \tag{1},$$

$M(\Delta\omega)$ and $M(-\Delta\omega)$ being, respectively, intensities of the water peak after on-resonance saturation (at the site of the exchangeable peak, offset $\Delta\boldsymbol{\omega}$ from water resonance frequency) and off-resonance

saturation (equal offset on the other side of water peak, $-\Delta\omega$). In-house MATLAB (R2014b) scripts were used for post-acquisition processing and plotting.

2.4 Exchange rate calculation. Exchange rates were calculated using the method proposed by Dixon *et al.*[21] The method uses a computationally simple linear regression method where the quantity $M_Z/(M_0 - M_Z)$ is fitted linearly against $1/\omega_1^2$. ω_1 is related to the r.f. power B_1 as $\omega_1 = \gamma B_1$, γ being the gyromagnetic ratio of proton. The negative x-axis intercept of the linear fit gives the exchange rate as $[1/\omega_1^2]_{intercept} = -1/(k_{ex})^2$. The method gives the best result under the condition that direct saturation (DS) of water is negligible, saturation powers (in Hz) used are not larger than the offset $\Delta\omega$ and saturation time is long enough to ensure complete saturation. To satisfy these conditions, exchange rates were measured at the highest magnetic field available in the laboratory, with long saturation duration and using a sinc pulse-train that produces low DS. In the pulse train, 50 ms sinc pulses were used with 4 ms inter-pulse delay. Maximum saturation power was adjusted by taking the chemical shift offset of the compound under study. All fittings were performed in Microsoft Excel.

2.5 Diffusion measurements. Pulse field Gradient Stimulated Echo (PGSE)[22] method was employed to determine the translational diffusion coefficient. To reduce the effect of Eddy current bipolar gradients were used. Attenuation of all ^{1}H NMR signals with a reasonable signal to noise was measured as a function of gradient strength. Gradient strength was varied between 2% and 95% of the peak gradient value of 48.15 Gauss/cm. The normalized peak intensity (I/I_0) for any particular gradient strength (g) follows a relationship $I/I_0=\exp(-D\zeta g^2)$, I_0 being the equilibrium intensity and ζ is a constant that depends on a number of experimental parameters and can readily be calculated.[22] Translational diffusion coefficient, D, was calculated from the negative slope (equal to $D\zeta$) of the linear fit of $\ln(I/I_0)$ plotted against g^2.

2.6 Relaxivity measurements. Relaxivity of a solute molecule is defined as the concentration (expressed in mM in most situations) normalized change in either longitudinal (R_1) or transverse (R_2) relaxation rate constants of water in presence of the solute. Inversion recovery method was used with 12 variable delays between 10 ms to 6 s to measure R_1. R_2 was measured using Carr−Purcell−Meiboom−Gill spin−echo sequence with 14 delays between 80 ms and 1.44 s. Sufficiently long recycle delay of 10 s was used for accurate measurement of the relaxation rate constants. Relaxivities were calculated from the measured R_1 and R_2 values.

3. Results and discussion

3.1 Role of inter-molecular hydrogen bonding in producing CEST contrast. At ambient temperatures, acetanilide (**1**) is known[18] to form molecular chains through interMHB as shown schematically in Figure. 1a. The hydrogen bond removes the partial double bond character of the C-N bond thereby facilitating a stable configuration that relieves the steric interaction between the ortho and the amine hydrogen atoms.[18] We hypothesize that it is this chain formation that makes

acetanilide a diaCEST agent as the interMHB lowers the exchange rate to the slow to medium exchange window. At physiological serum condition of pH 7.4 at 37 °C, acetanilide shows a significant 12.4% contrast with 15 mM concentration (Figure. 1b). To confirm our hypothesis that without the interMHB mediated molecular chains an individual acetanilide would not show appreciable CEST, we performed a series of variable temperature experiments. Assuming our hypothesis true, we anticipated that at some temperature when the interMHB chain would break, the CEST contrast would simply disappear. Figure. 1c shows the stack-plot of the labile amine proton of acetanilide acquired in DMSO-d_6 as a function of temperature. The gradual upfield shift of the NH proton with temperature supports the fact of slow reappearance of the electron density that was originally withdrawn due to the formation of the interMHB. When we plotted the peak shift (Δv) from the position at 298 K, we found an interesting behavior (Figure. 1d). Up to 313 K (40 °C) the shift followed the expected linear relationship with temperature as generally is observed for many solutes. However, beyond 313 K, the shift deviated from the linear relationship which strongly indicates the onset of an event, possibly the breaking up of the interMHB chain. The observed change in linewidth (LW) with temperature was found to be even more interesting (Figure. 1e). For small molecules, the transverse relaxation rate constant generally drops with a decrease in rotational correlation time (with an increase in temperature). As a consequence, the linewidth should also drop as the sample heats up. Contrary to this expected behaviour the linewidth was found to be monotonically increasing with temperature. Moreover, the linewidth also deviated from the expected linear behaviour (R_2 changes nearly linearly with temperature for small molecules) beyond 313 K. This could only be explained if we assume that the acetanilide molecules jump between the free and the chain configurations causing exchange broadening. With an increase in temperature, the exchange broadening should naturally increase. The amine proton

of acetanilide in water shows expected non-linear increase in solute-solvent exchange rate with temperature (Figure. 1f, Figures. 2 – 10, for corresponding z-spectra). At 333 K the increase in exchange rate shows an avalanche which takes the exchange rate beyond the slow to medium exchange regime as can be seen from the plot of $(\Delta\omega - k_{ex})$ as function of temperature (Figure. 1g). When we tried to check if the non-linear variation followed an Arrhenius type exponential equation and plotted ln (k_{ex}) as a function of 1/T, we found that the plot deviated from the expected linear behaviour beyond 313 K just like the peak shift and the peak linewidth did (Figure. 1h). The departure from the linear behaviour clearly indicates that the rise of the exchange rate was not entirely due to the rise of the solvent temperature but also due to the gradual breaking of the interMHB chain. Without the partial locking imposed by interMHB, the labile proton exchanged too fast. The sudden increase of k_{ex} at 333 K is possibly due to the complete disruption of the interMHB mediated molecular chain network. The discussion so far has picked up on a number of occasions the temperature 313 K as the onset temperature of an event. To further confirm that the event indeed was the breaking up of the molecular chain, we estimated at different temperatures the effective hydrodynamic radius (r_T) of the molecules in the solution from the measured translational diffusion coefficient as per the following relationship,[23]

$$r_T = \frac{k_B T}{6\pi\eta D}$$
(2),

where, k_B, T, η and D denote, respectively, the Boltzmann constant, absolute solvent temperature, solvent viscosity at temperature T and translational diffusion coefficient of acetanilide. In absence of any structural changes of the molecules, the effective hydrodynamic radius should remain unchanged and hence the ratio $r_T/r_{T'}$ for any two temperatures T and T' should be equal to 1. Figure. 1i shows for different temperatures the ratio r_{298}/r_T, which deviates from the expected value of 1 beyond 313 K as has been seen previously with other experimental parameters. The fact

that beyond 313 K, r_T becomes smaller than r_{298} confirms the breaking of the longer molecular

chains into smaller fragments. Finally, Figure. 1j shows CEST contrast efficiency of acetanilide as

a function of the exchange constant and the temperature (Figure. 1j inset). Figure. 1j shows a

smooth initial increase in the CEST contrast as a function of increasing k_{ex} (and also temperature)

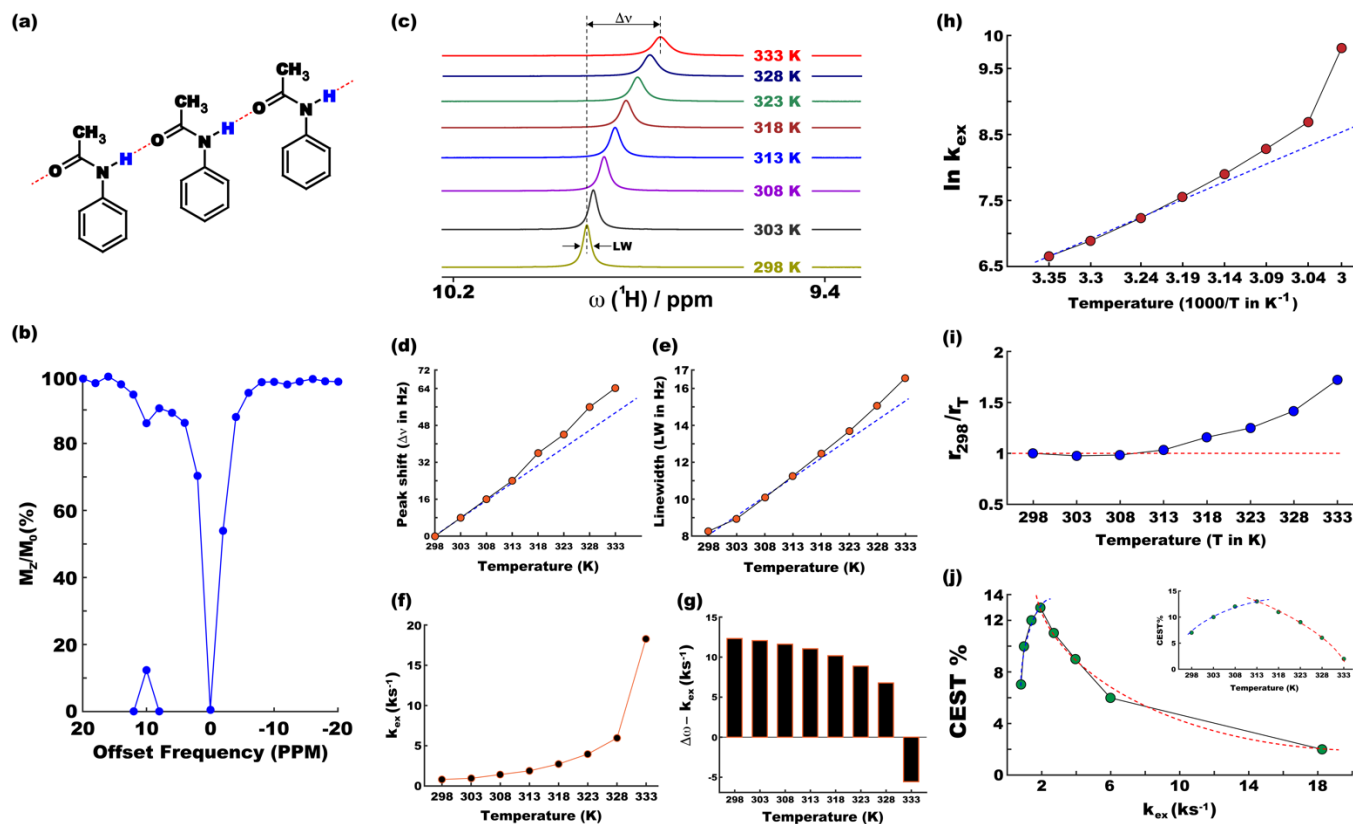but beyond 313 K, the CEST efficiency starts abruptly dropping.

Figure 1 (a) Schematic representation of molecular chain formation through inter-molecular hydrogen bonding by acetanilide in solution. (b) The CEST z-spectrum of acetanilide at the physiological condition (pH 7.4, 37 °C). MTR$_{assym}$ peak on the x-axis shows 12.4% CEST contrast. (c) Stack 1D plot of the labile amine peak of acetanilide in DMSO-d6 as a function of temperature. Temperature dependent peak-shift with respect to the position at 298 K (d) and peak line-width (e) of the acetanilide amine proton. (f) Exchange rate of the amine proton in water as a function of temperature. The exchange rate crosses the important limit of Dw (offset with respect to water peak position) at 333 K (g). (h) Natural logarithm of the exchange constant against the inverse of temperature. (i) The ratio of effective hydrodynamic radii at temperature T and at 298 K. (j) CEST contrast percentage as a function of exchange rate constant and temperature (inset). None of the dotted lines are mathematical fitting of data. They simply help to visualize the pattern of the data points. Please refer to the main text for analysis of the data towards confirming the gradual breaking up of the chain formation with increasing temperature.

A clear change in the slope of the curves (the blue and red dotted guidelines) indicate once again the onset of the event of breaking of interMHB chains. The population of the free acetanilide molecules in the dynamic mixture cannot produce CEST contrast due to very fast exchange and as with increasing temperature the fractional population of free molecules increases, the CEST efficiency gradually drops. At 333 K when the free molecule population dominates heavily, the CEST effect nearly disappears. Figures 2-10 shows the variation of exchange rate of N-phenyl acetamide with temperature.

a.

b.
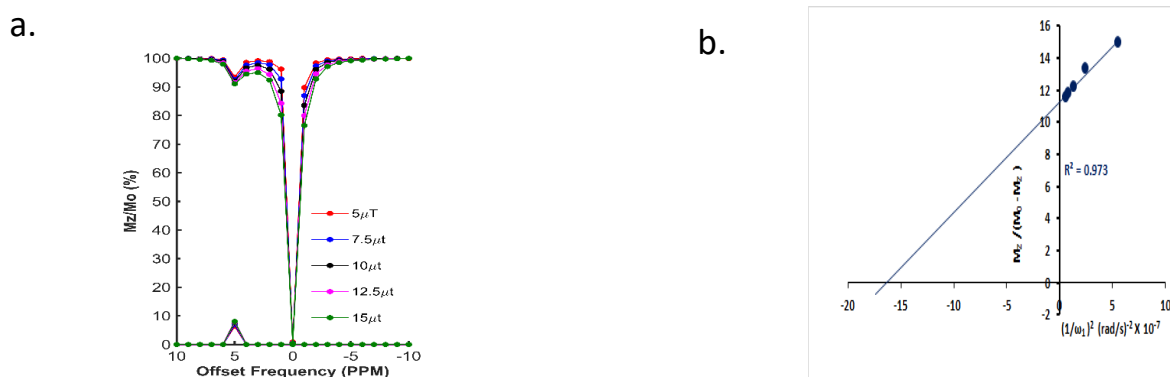
Figure 2: (a) Dependence of CEST percentage on saturation field strength ranging from 5 µT to 15 µT for N-phenylacetamide (**1**) at 298K and pH 7.4 (b) Omega plot for exchange rate measurement. The expected linear relationship of $M_z/(M_0-M_z)$ as a function of $1/\omega_1^2$ $(rad/sec)^{-2}$ x 10^{-7} was obtained when recorded at 16.3 T of 15 mM compound in 0.01M PBS buffer at pH 7.4. RF saturation pulse was applied for 6 s ensuring complete saturation.
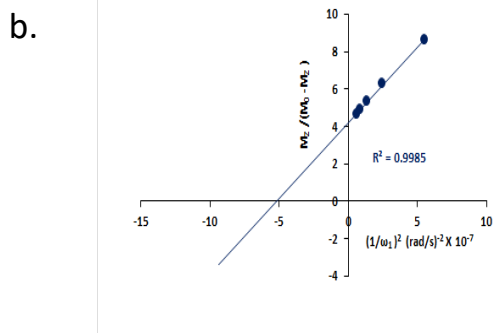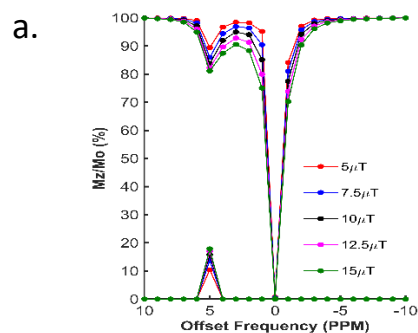
a.

b.
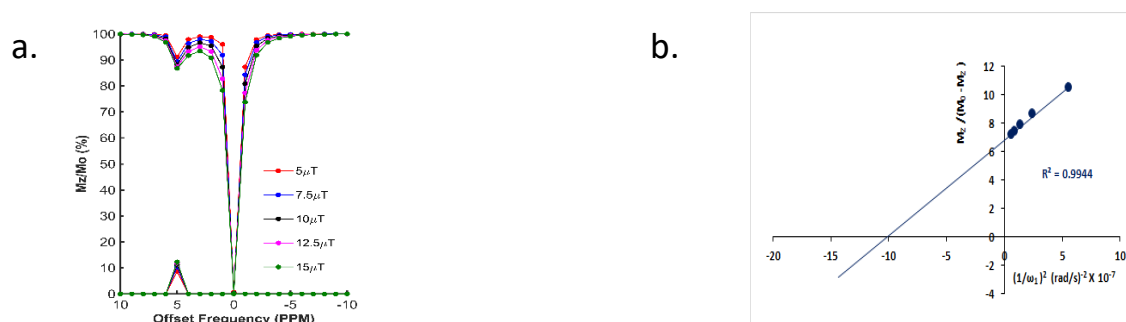
Figure 3: (a) Dependence of CEST percentage on saturation field strength ranging from 5 µT to 15 µT for N-phenylacetamide (**1**) at 303K and pH 7.4 (b) Omega plot for exchange rate measurement. The expected linear relationship of $M_z/(M_0-M_z)$ as a function of $1/\omega_1^2$ $(rad/sec)^{-2}$ x 10^{-7} was obtained when recorded at 16.3 T of 15 mM compound in 0.01M PBS buffer at pH 7.4. RF saturation pulse was applied for 6 s ensuring complete saturation.
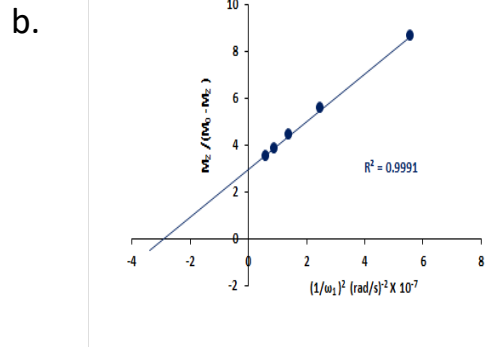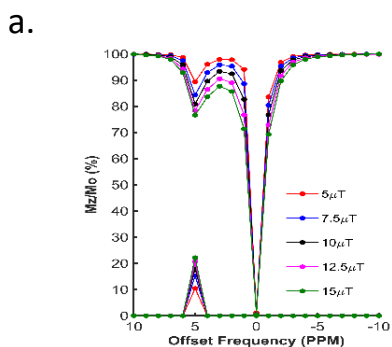
Figure 4: (a) Dependence of CEST percentage on saturation field strength ranging from 5 µT to 15 µT for N-phenylacetamide (**1**) at 308K and pH 7.4 (b) Omega plot for exchange rate measurement. The expected linear relationship of $M_z/(M_0-M_z)$ as a function of $1/\omega_1^2$ $(rad/sec)^{-2}$ x 10^{-7} was obtained when recorded at 16.3 T of 15 mM compound in 0.01M PBS buffer at pH 7.4. RF saturation pulse was applied for 6 s ensuring complete saturation.
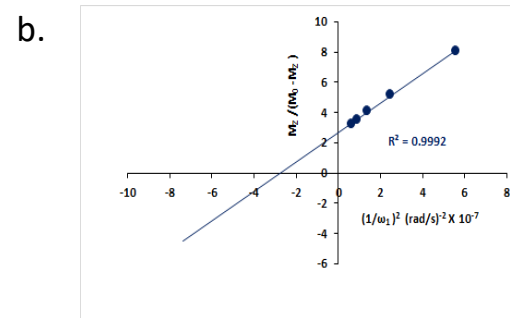

Figure 5: (a) Dependence of CEST percentage on saturation field strength ranging from 5 µT to 15 µT for N-phenylacetamide (**1**) at 310K (b) Omega plot for exchange rate measurement. The expected linear relationship of $M_z/(M_0-M_z)$ as a function of $1/\omega_1^2$ $(rad/sec)^{-2}$ x 10^{-7} was obtained when recorded at 16.3 T of 15 mM compound in 0.01M PBS buffer at pH 7.4. RF saturation pulse was applied for 6 s ensuring complete saturation.
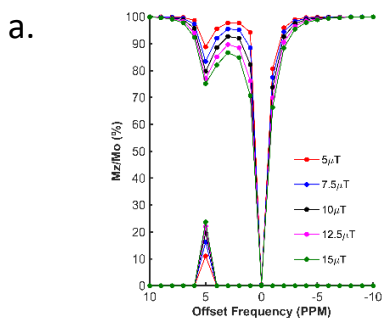

Figure 6: (a) Dependence of CEST percentage on saturation field strength ranging from 5 µT to 15 µT for N-phenylacetamide (**1**) at 313K and pH 7.4 (b) Omega plot for exchange rate measurement. The expected linear relationship of $M_z/(M_0-M_z)$ as a function of $1/\omega_1^2$ $(rad/sec)^{-2}$ x 10^{-7} was obtained when recorded at 16.3 T of 15 mM compound in 0.01M PBS buffer at pH 7.4. RF saturation pulse was applied for 6 s ensuring complete saturation.
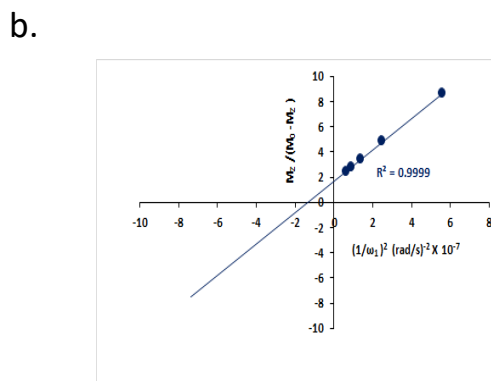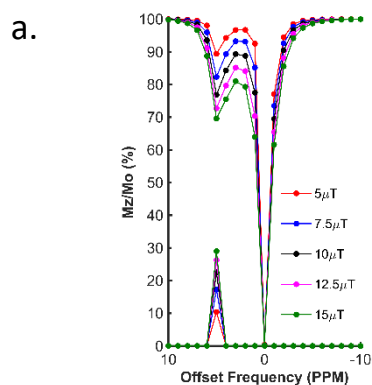
Figure 7: (a) Dependence of CEST percentage on saturation field strength ranging from 5 µT to 15 µT for N-phenylacetamide (**1**) at 318K and pH 7.4 (b) Omega plot for exchange rate measurement. The expected linear relationship of $M_z/(M_0-M_z)$ as a function of $1/\omega_1^2$ $(rad/sec)^{-2}$ x 10^{-7} was obtained when recorded at 16.3 T of 15 mM compound in 0.01M PBS buffer at pH 7.4. RF saturation pulse was applied for 6 s ensuring complete saturation.
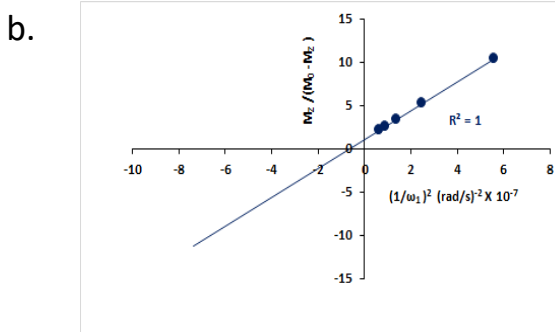

Figure 8: (a) Dependence of CEST percentage on saturation field strength ranging from 5 µT to 15 µT for N-phenylacetamide (**1**) at 323K and pH 7.4 (b) Omega plot for exchange rate measurement. The expected linear relationship of $M_z/(M_0-M_z)$ as a function of $1/\omega_1^2$ $(rad/sec)^{-2}$ x 10^{-7} was obtained when recorded at 16.3 T of 15 mM compound in 0.01M PBS buffer at pH 7.4. RF saturation pulse was applied for 6 s ensuring complete saturation.
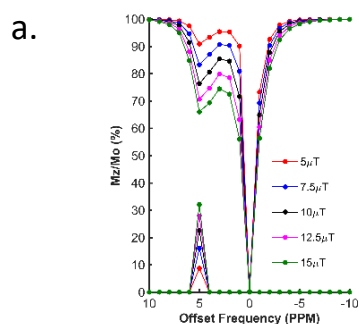

Figure 9: (a) Dependence of CEST percentage on saturation field strength ranging from 5 µT to 15 µT for N-phenylacetamide (**1**) at 328K and pH 7.4 (b) Omega plot for exchange rate measurement. The expected linear relationship of $M_z/(M_0-M_z)$ as a function of $1/\omega_1^2$ $(rad/sec)^{-2}$ x 10^{-7} was obtained when recorded at 16.3 T of 15 mM compound in 0.01M PBS buffer at pH 7.4. RF saturation pulse was applied for 6 s ensuring complete saturation.
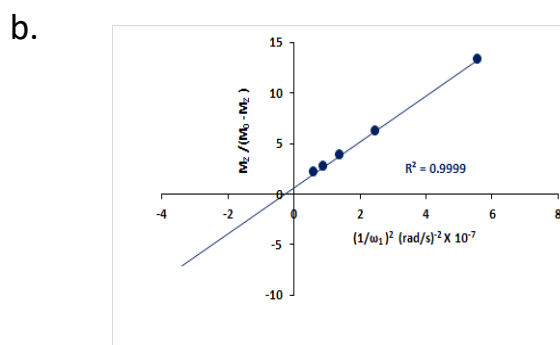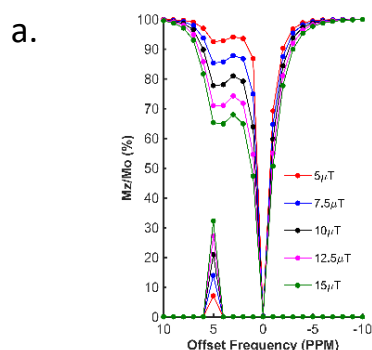
a.

b.

Figure 10: (a) Dependence of CEST percentage on saturation field strength ranging from 5 µT to 15 µT for N-phenylacetamide (**1**) at 333K and pH 7.4 (b) Omega plot for exchange rate measurement. The expected linear relationship of $M_z/(M_0-M_z)$ as a function of $1/\omega_1^2$ (rad/sec)$^{-2}$ x 10^{-7} was obtained when recorded at 16.3 T of 15 mM compound in 0.01M PBS buffer at pH 7.4. RF saturation pulse was applied for 6 s ensuring complete saturation
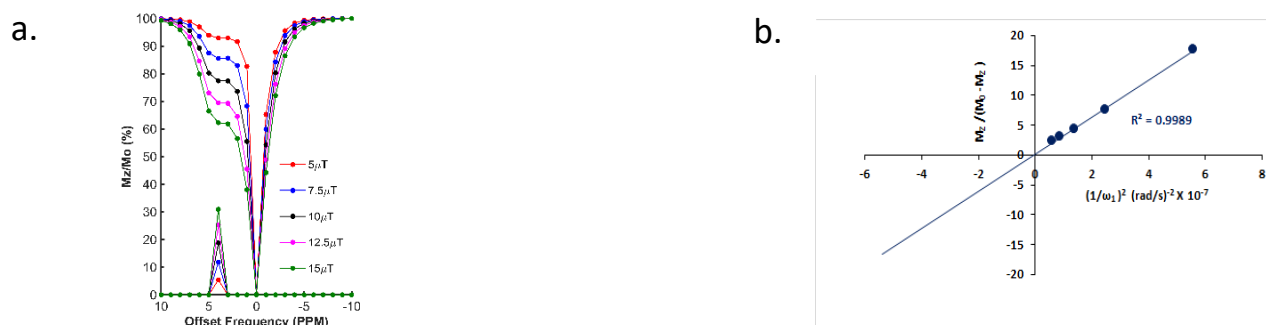
The observation that the onset temperature (313 K) for all the events is so close to the physiological temperature of 310 K made us believe that without the interMHB, acetanilide would have had an exchange rate at the physiological temperature too high for any meaningful CEST contrast.

3.2 Variation of exchange rate and CEST efficiency in different acetanilide derivatives.

Upon being convinced that the acetanilide molecule as a single entity is not effective and needs to form a colony through interMHB to show contrast, we synthesized a number of water-soluble derivatives of acetanilide to explore the system while keeping the interMHB chain formation intact (Table 1, Figures 11-26). The steric and electronic effects brought in by different substitutions generally plays an important role in determining the frequency offset, exchange rate and CEST efficiency of a molecules. In the present scenario, the additional influence of interMHB was expected to play a pivotal role. In presence of electron withdrawing groups like fluorine or carboxylic acid at the para position, the electron density around the NH proton decreases resulting in a downfield shift of the amide proton with respect to acetanilide.

Contrary to this, electron donating group at the para position increases the electron density and causes an upfield shift of the amide proton. In case of ortho substitutions, the field effect produces further upfield shift. For para hydroxy acetanilide the combination of inductive as well as the

mesomeric effect of the hydroxyl group is instrumental in producing maximum upfield shift for the NH proton among all the derivatives studied. We found that for all the para-substitutions, a negative correlation exists between pKa of the molecule and the k_{ex} (Figures. 27-33) for corresponding z-spectra). In the presence of electron-withdrawing substituents like fluorine (**2**), the electron density decreases at the nitrogen centre because of –I effect, which in turn increases the lability and hence k_{ex} of the amine proton. However, we did not find the CEST contrast increasing in accordance in comparison to **1**. For para methyl (**3**) and para methoxy (**4**) substituents both k_{ex} and the CEST efficiency dropped from **1**. In the case of carboxylic acid substitution at the para-position (**5**) the electron density increases at the site of hydrogen bond donation due to the presence of carboxylate anion at the basic pH. Thus the exchange rate as well as the CEST percentage quite expectedly decreased considerably. Among the ortho substituents, *o*-methoxy (**6**) and *o*-hydroxy (**7**) acetanilide showed a drastic increase in k_{ex} most likely due to the solvation of the molecules with the bulk water. Interestingly, even with such a steep increase in k_{ex}, the CEST efficiency was found to be very moderate for both **6** and **7**. In the case of hydroxy substitutions, both meta (**8**) and the para (**9**) substituted acetanilides produced a higher CEST effect than *o*-hydroxy substitution, with **9** being the top of the lot in spite of the fact that **9** does not show the highest exchange rate among the hydroxy-substituted acetanilide compounds. As CEST contrast depends on several other factors including relaxation rate constants of the labile proton of the solute, and in the presence of interMHB network these parameters can widely vary, we could not see any direct correlation of the exchange rate and/or offset frequency with the CEST contrast efficiency of one acetanilide derivative with respect to the other. Paracetamol (**9**) shows better CEST efficiency than most other derivatives in spite of the fact that it has the smallest frequency offset.
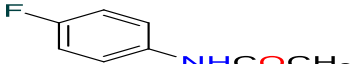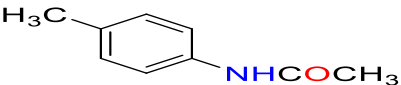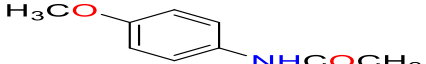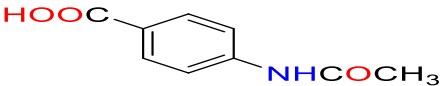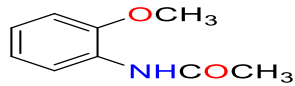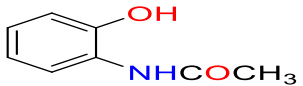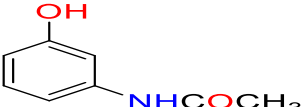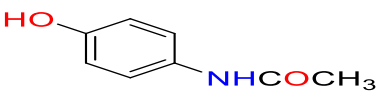
5.21 ppm, 12.4 %, 1.8 ks^{-1}   **5.27 ppm, 11.9 %, 2.7 ks^{-1}**   **5.07 ppm, 6.8 %, 1.7 ks^{-1}**

5.06 ppm, 8.2 %, 1.6 ks^{-1}   **5.53 ppm, 0.5 %, 1.0 ks^{-1}**   **4.41 ppm, 7.5 %, 3.08 ks^{-1}**

4.61 ppm, 8.1 %, 4.1 ks^{-1}   **4.60 ppm, 10.5 %, 2.1 ks^{-1}**   **4.43 ppm, 12 %, 1.2 ks^{-1}**

Table 1: Frequency offset, CEST contrast and exchange rates for acetanilide derivatives. All experiments were performed at 15 mM sample concentration in 10 mM PBS at the physiological condition of pH 7.4 and 37 °C.
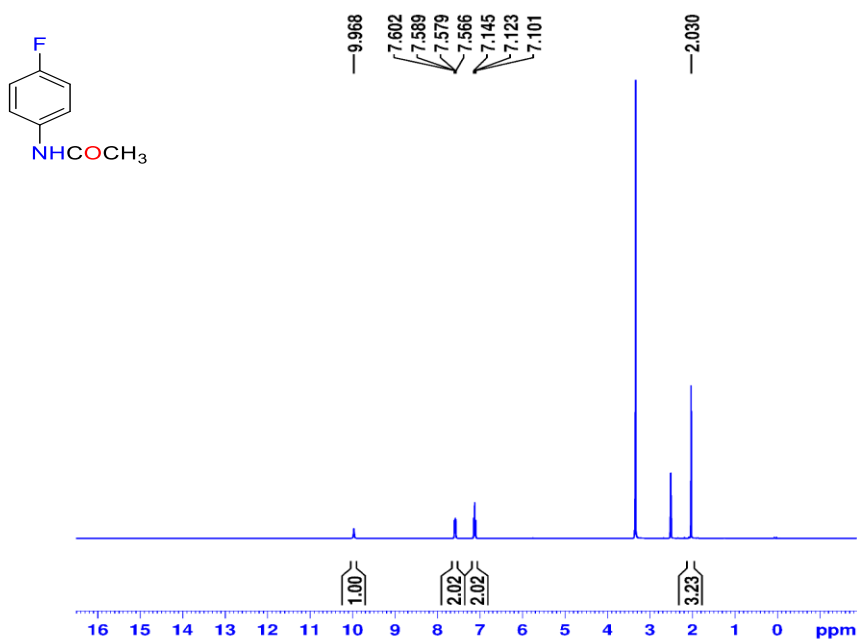
Figure 11: ^{1}H-NMR spectrum of *N*-(4-fluorophenyl)acetamide (**2**) in DMSO-d$_6$ at 298K.
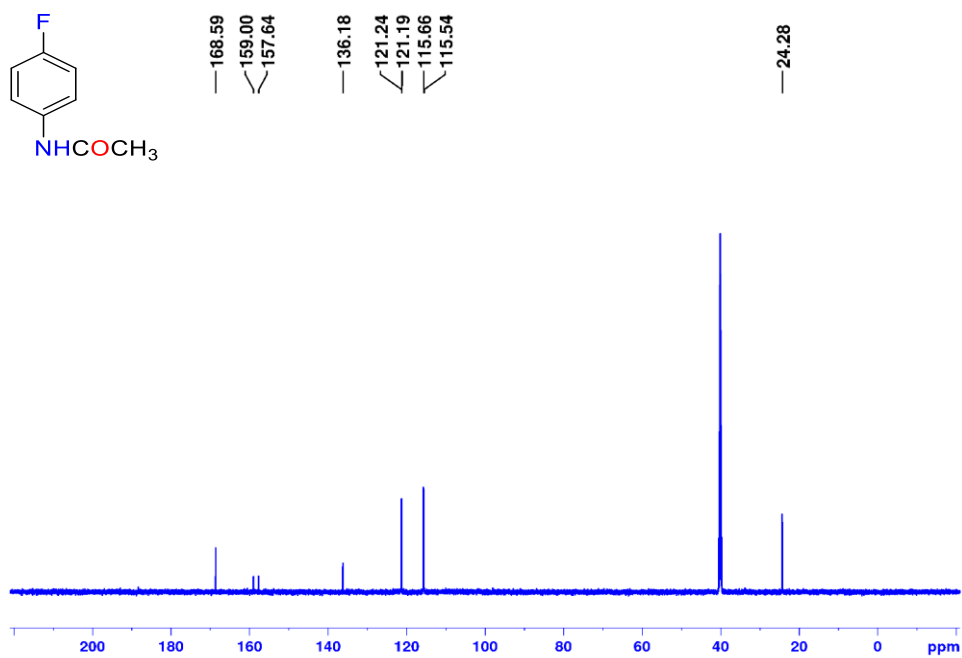
Figure 12: ^{13}C NMR spectrum of *N*-(4-fluorophenyl)acetamide (**2**) in DMSO-d$_6$ at 298K.
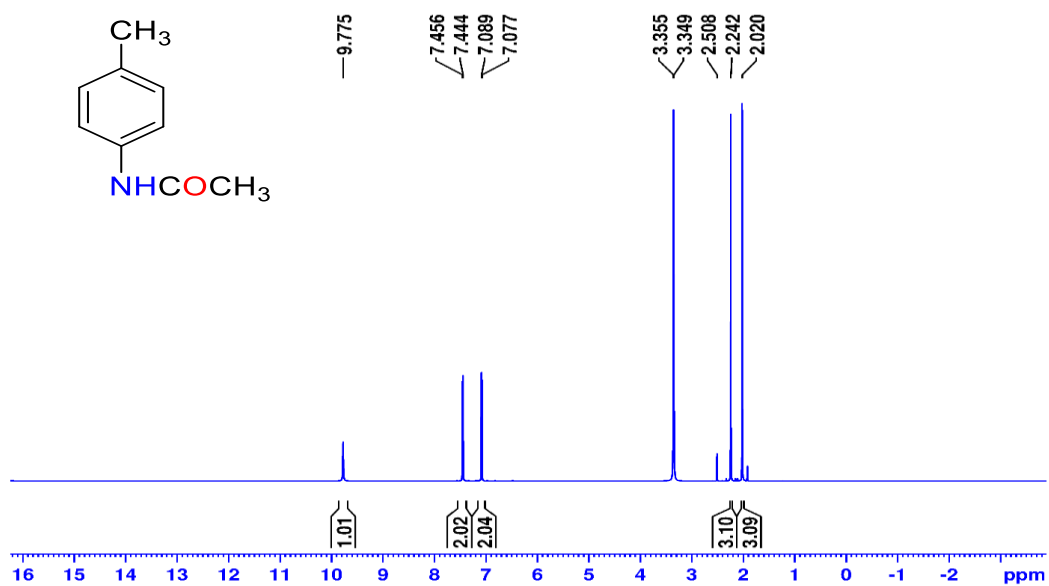
Figure 13: ^{1}H-NMR spectrum of *N*-(p-tolyl)acetamide (**3**) in DMSO-d$_6$ at 298K.
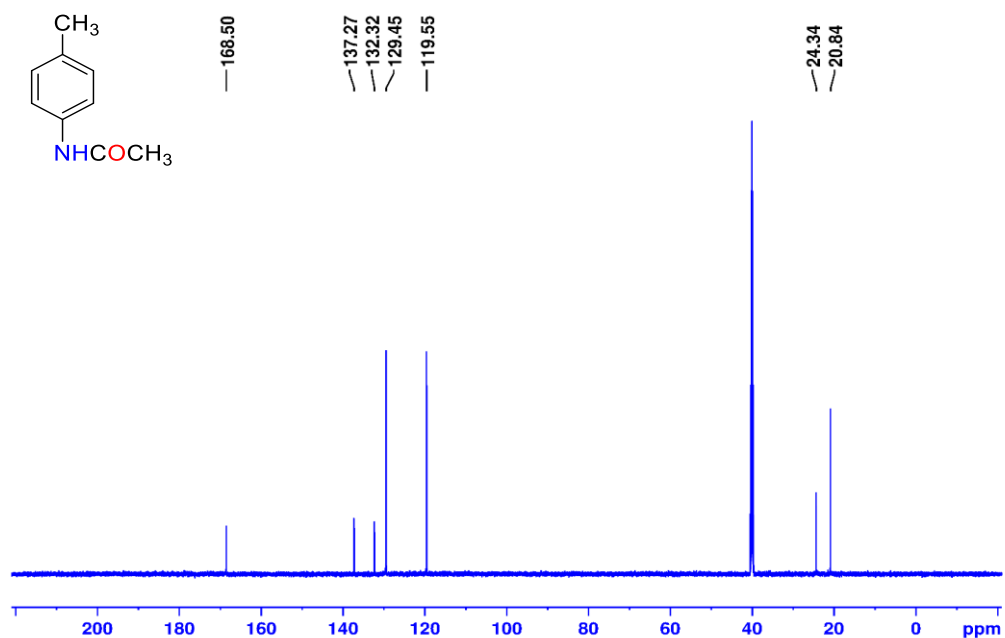
Figure 14: ^{13}C NMR spectrum of *N*-(p-tolyl)acetamide (**3**) in DMSO-d$_6$ at 298K.
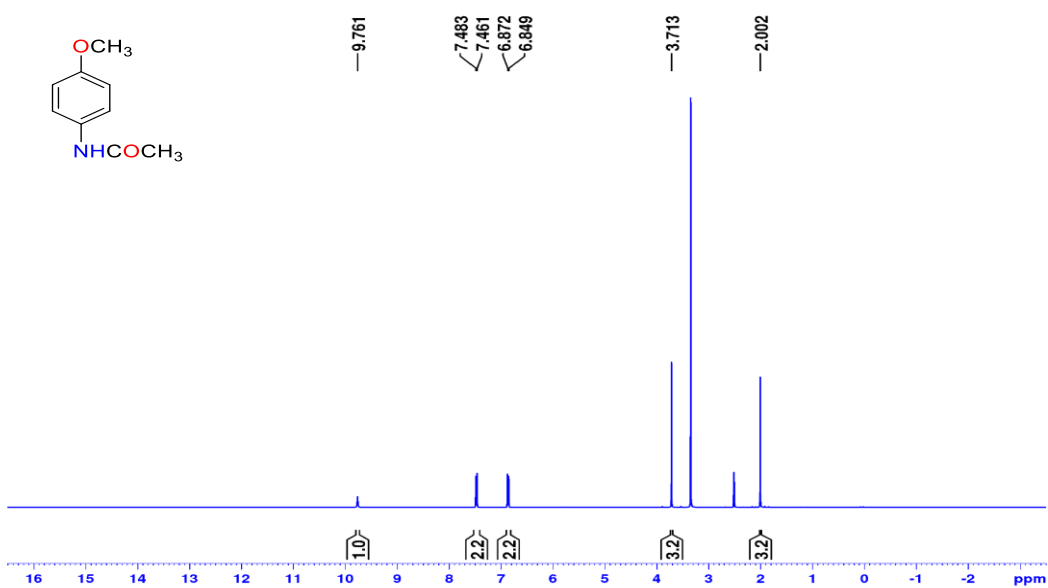
Figure 15: ^{1}H-NMR spectrum of N-(4-methoxyphenyl)acetamide (**4**) in DMSO-d$_6$ at 298K.
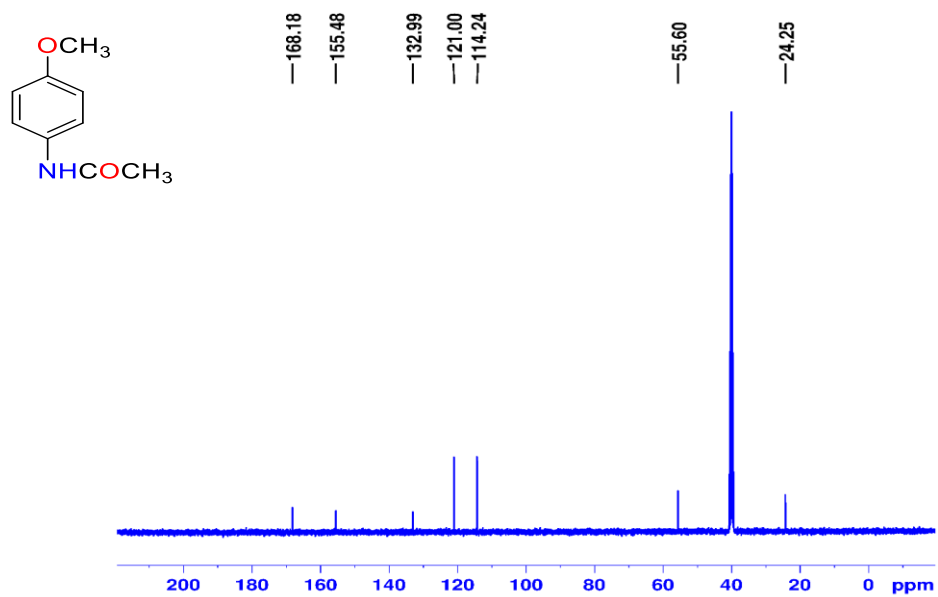
Figure 16: ^{13}C NMR spectrum of N-(4-methoxyphenyl)acetamide (**4**) in DMSO-d$_6$ at 298K.
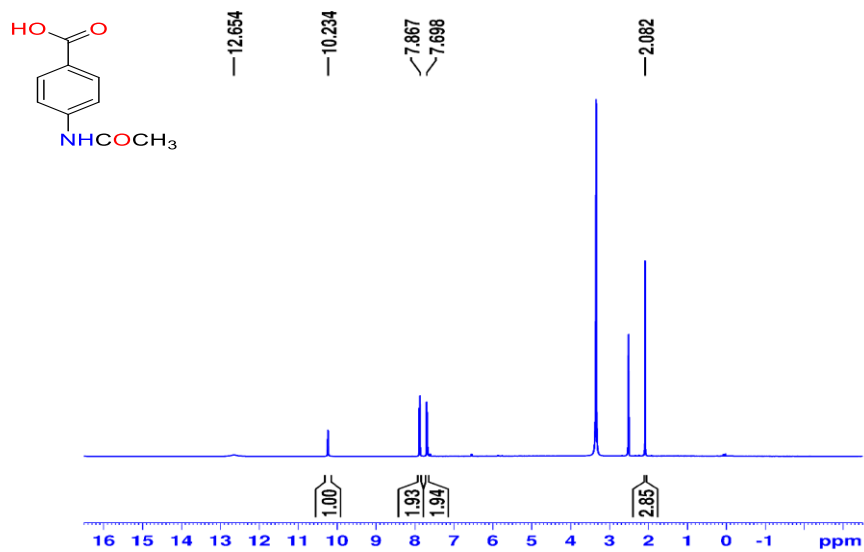
Figure 17: ^{1}H-NMR spectrum of 4-acetamidobenzoic acid (**5**) in DMSO-d$_6$ at 298K.
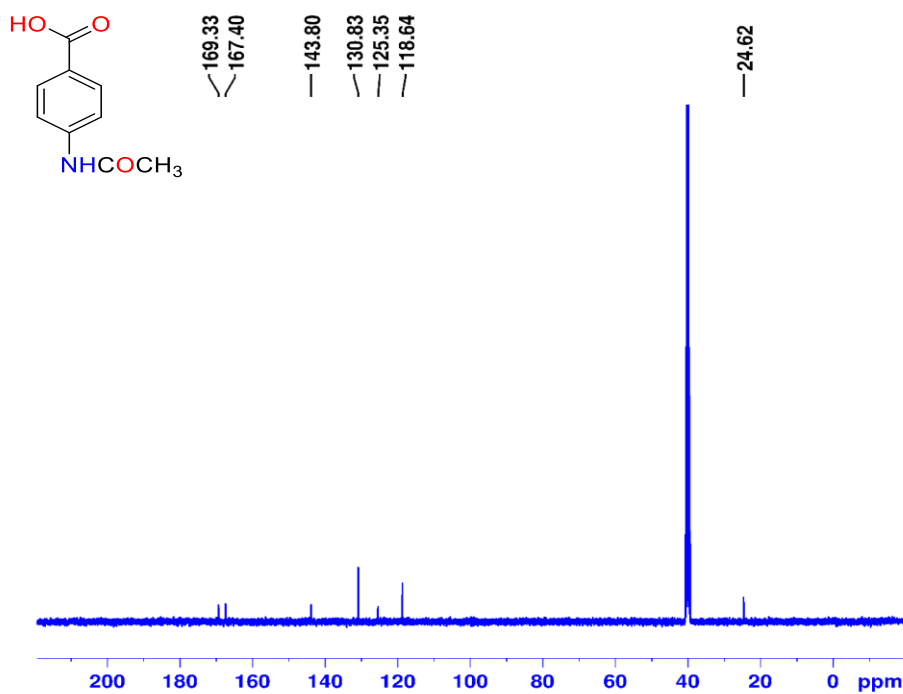
Figure 18: ^{13}C NMR spectrum of 4-acetamidobenzoic acid (**5**) in DMSO-d$_6$ at 298K.
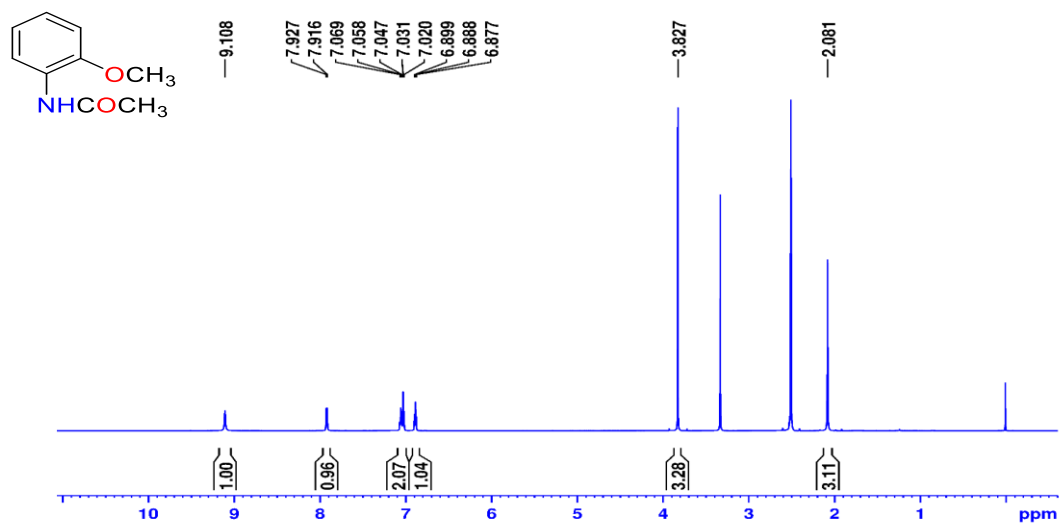
Figure 19: ^{1}H-NMR spectrum of N-(2-methoxyphenyl) acetamide (**6**) in DMSO-d$_6$ at 298K.
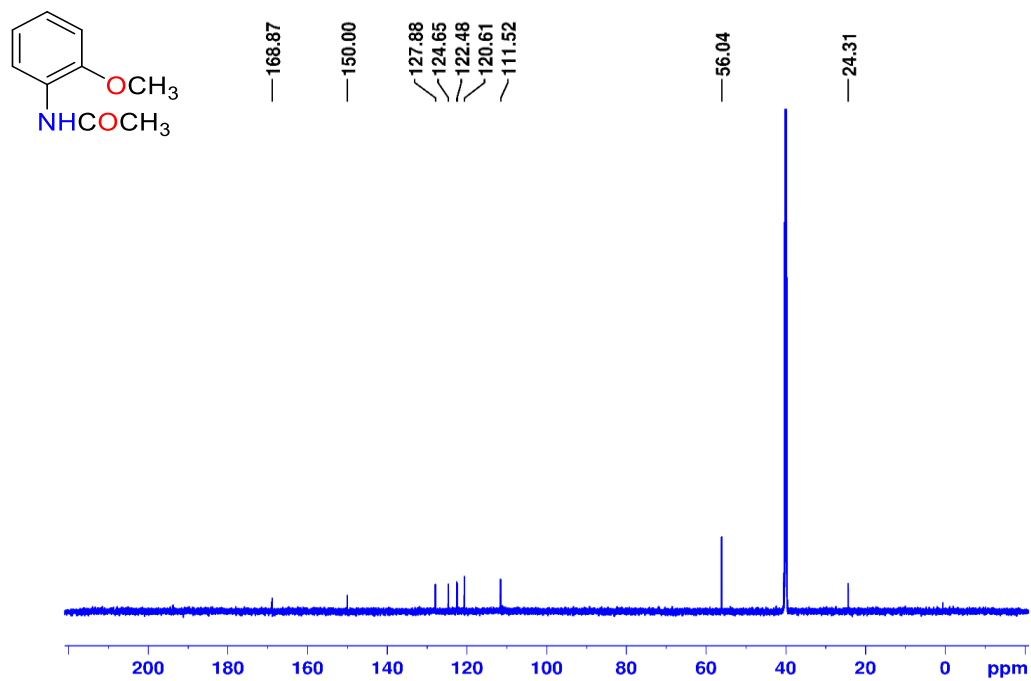
Figure 20: ^{13}C NMR spectrum of N-(2-methoxyphenyl) acetamide (**6**) in DMSO-d$_6$ at 298K.
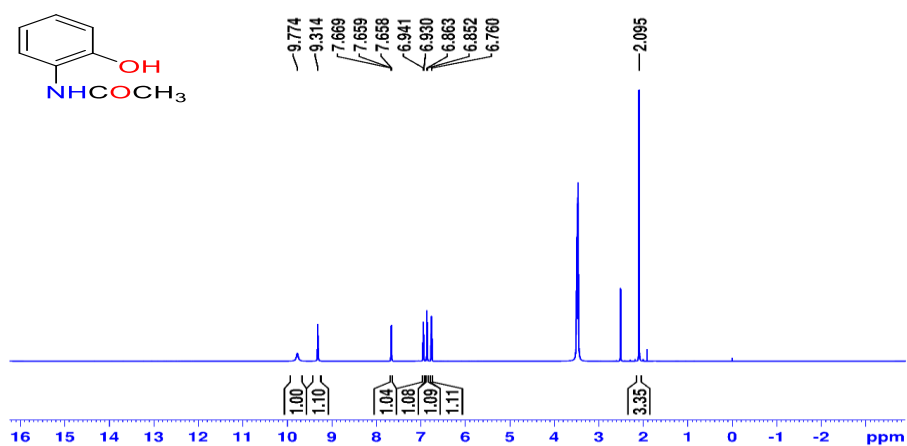
Figure 21: ^{1}H-NMR spectrum of N-(2-hydroxyphenyl)acetamide (**7**) in DMSO-d$_6$ at 298K.
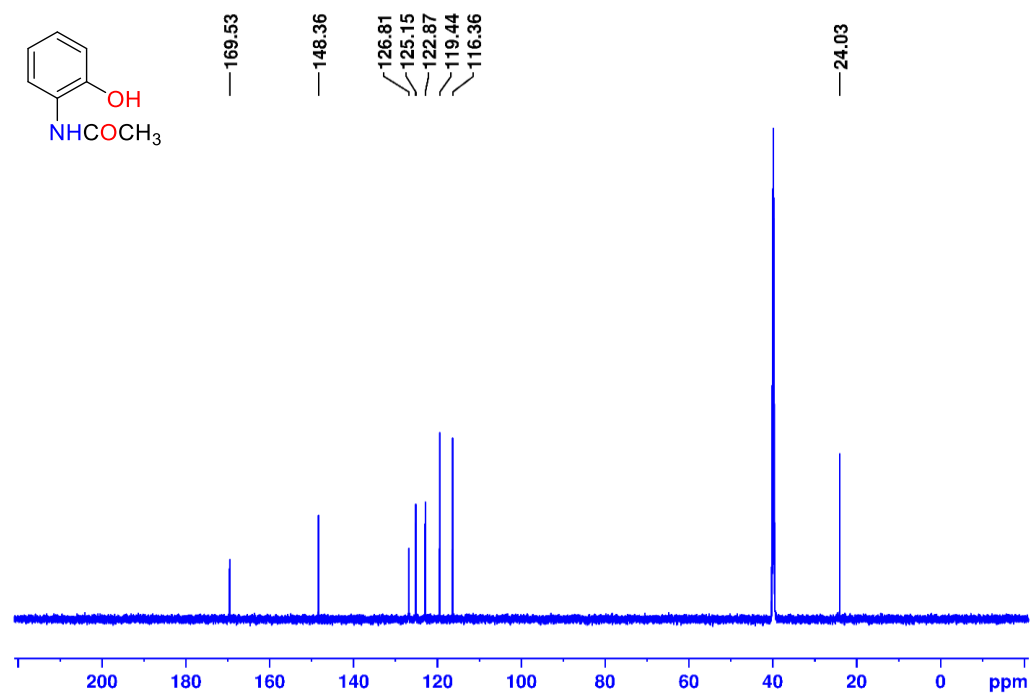
Figure 22: ^{13}C NMR spectrum of N-(2-hydroxyphenyl)acetamide (**7**) in DMSO-d$_6$ at 298K.
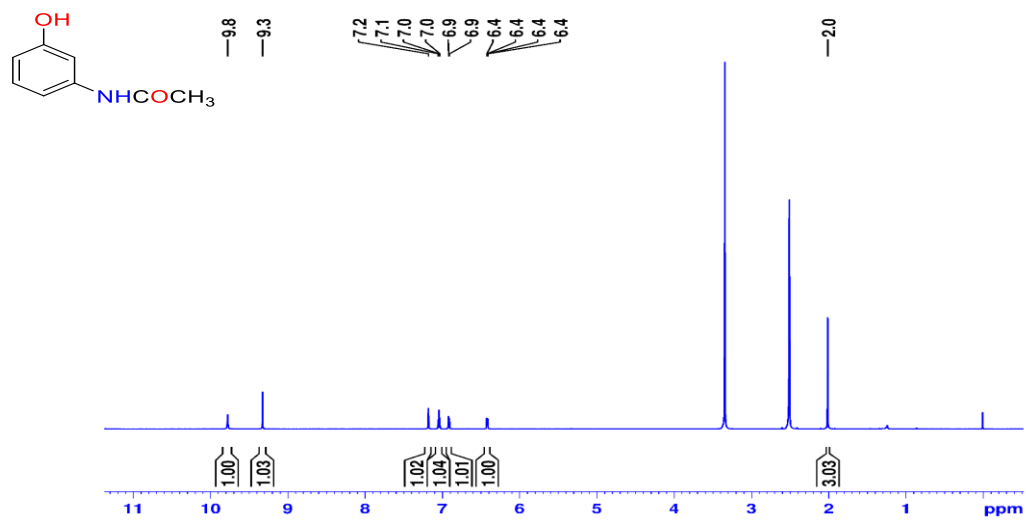
Figure 23: ^1H-NMR spectrum of N-(3-hydroxyphenyl) acetamide (**8**) in DMSO-d$_6$ at 298K.
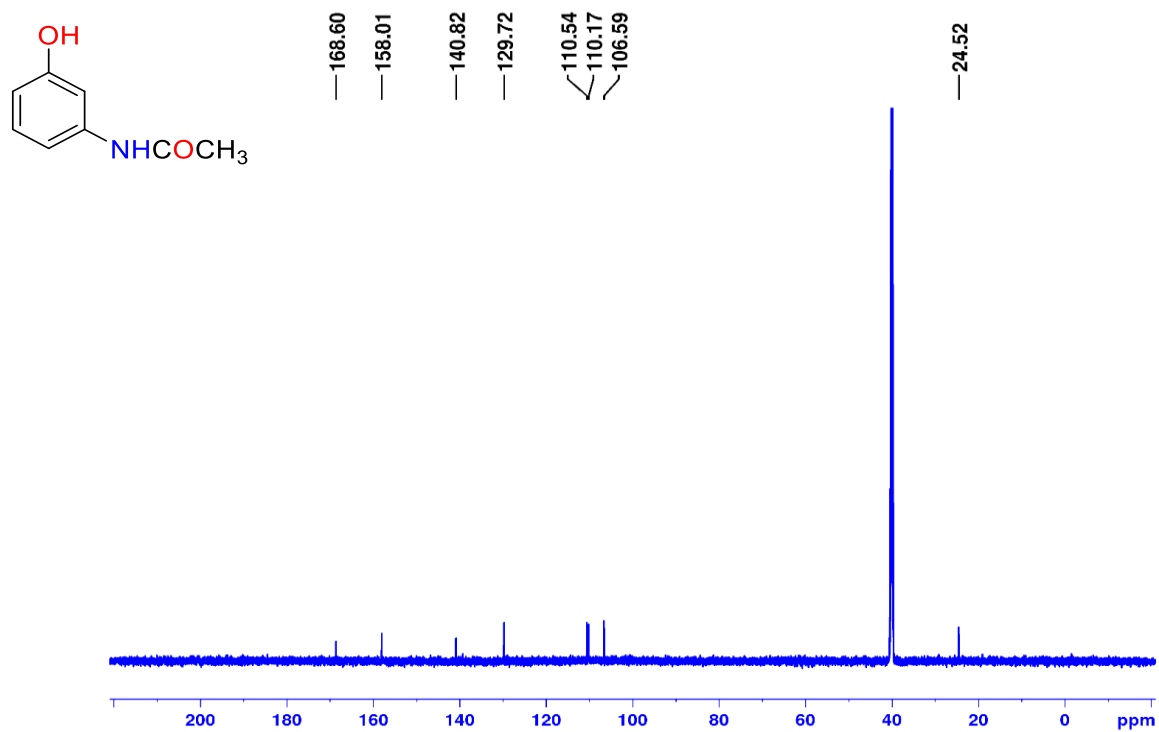
Figure 24: ^{13}C NMR spectrum of N-(3-hydroxyphenyl) acetamide (**8**) in DMSO-d$_6$ at 298K.
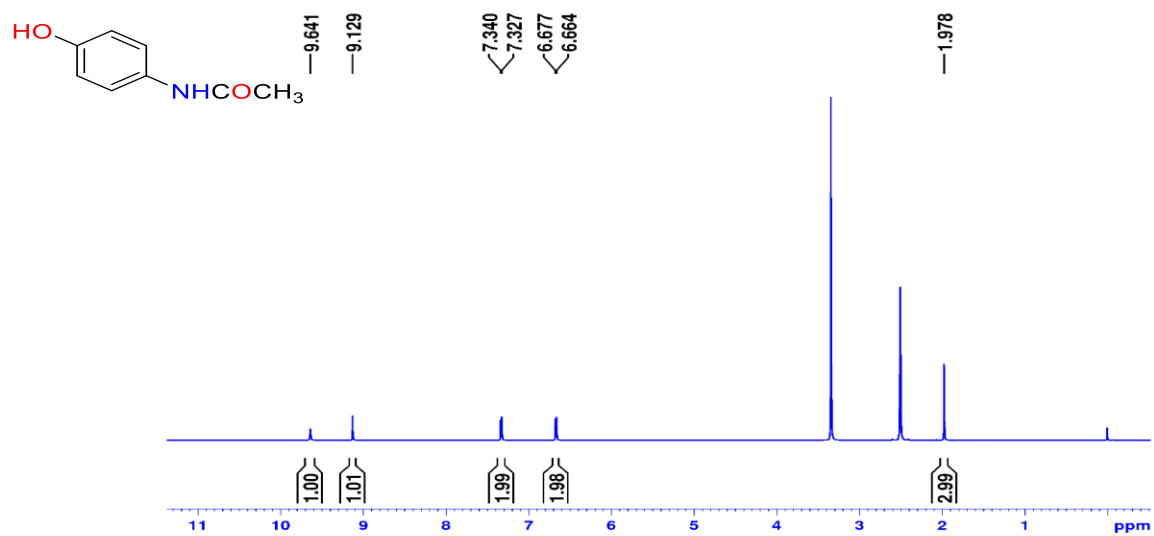
Figure 25: ^{1}H-NMR spectrum of N-(4-hydroxyphenyl) acetamide (**9**) in DMSO-d$_6$ at 298K.
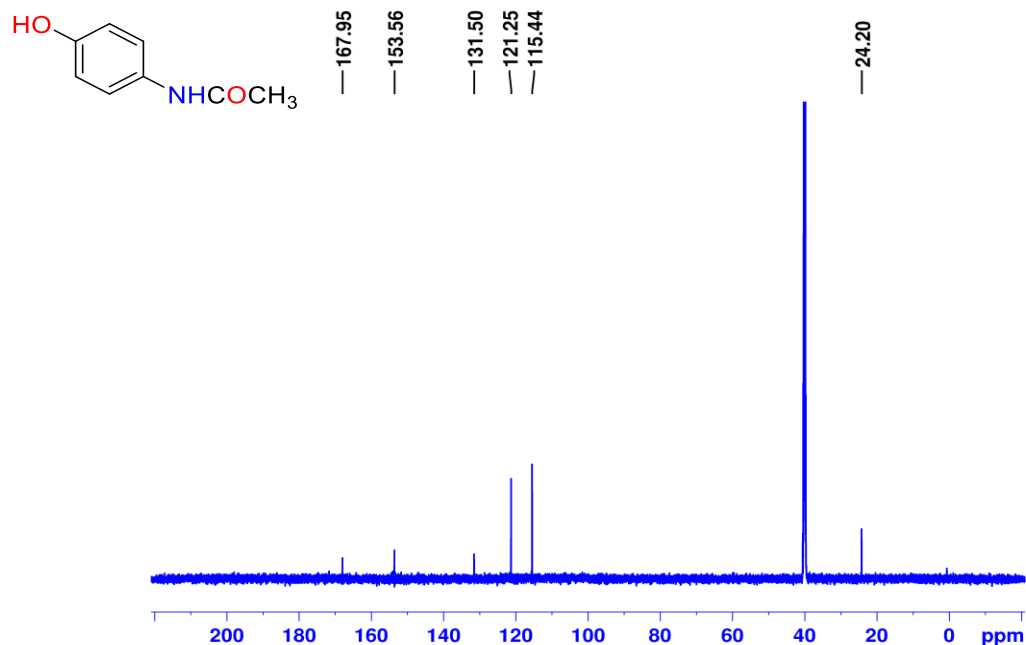
Figure 26: ^{13}C NMR spectrum of N-(4-hydroxyphenyl) acetamide (**9**) in DMSO-d$_6$ at 298K.

Figure 27: (a) z-spectra of 15mM *N*-(4-fluorophenyl)acetamide (**2**) at 310K and at pH 7.4 recorded at 9.3T (b) Dependence of CEST percentage on saturation field strength ranging from 5µT to 15µT for (2) (c) Omega plot for exchange rate measurement. The expected linear relationship of $M_z/(M_0-M_z)$ as a function of $1/\omega_1^2$ (rad/sec)$^{-2}$ x 10^{-7} was obtained when recorded at 16.3 T of 15 mM compound in 0.01M PBS buffer at pH 7.4. RF saturation pulse was applied for 6 s ensuring complete saturation.
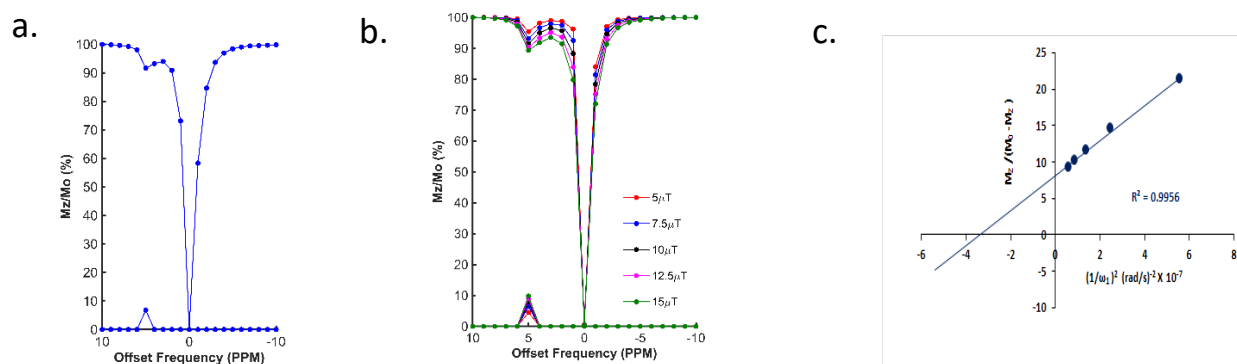
Figure 28: (a) z-spectra of 15mM N-(p-tolyl)acetamide (**3**) at 310K and at pH 7.4 recorded at 9.3T (b) Dependence of CEST percentage on saturation field strength ranging from 5 µT to 15 µT for (3) (c) Omega plot for exchange rate measurement. The expected linear relationship of $M_z/(M_0-M_z)$ as a function of $1/\omega_1^2$ $(rad/sec)^{-2}$ x 10^{-7} was obtained when recorded at 16.3 T of 15 mM compound in 0.01M PBS buffer at pH 7.4. RF saturation pulse was applied for 6 s ensuring complete saturation.
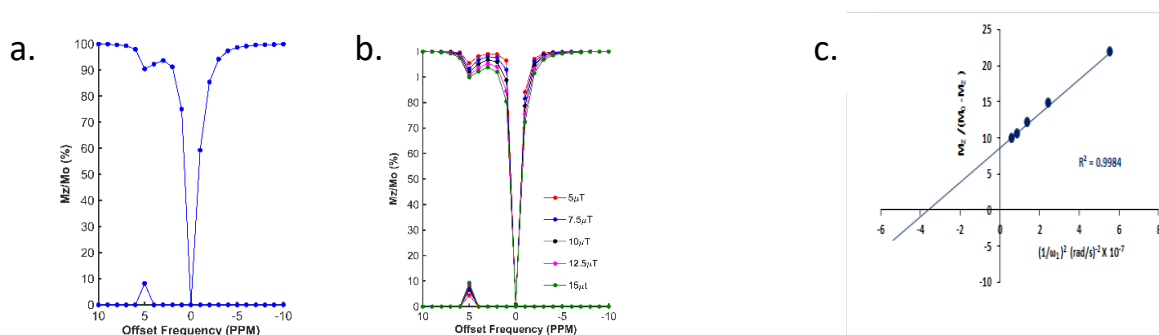
Figure 29: (a) z-spectra of 15mM N-(4-methoxyphenyl)acetamide (**4**) at 310K and at pH 7.4 recorded at 9.3T (b) Dependence of CEST percentage on saturation field strength ranging from 5 µT to 15 µT for (4) (c) Omega plot for exchange rate measurement. The expected linear relationship of $M_z/(M_0-M_z)$ as a function of $1/\omega_1^2$ $(rad/sec)^{-2}$ x 10^{-7} was obtained when recorded at 16.3 T of 15 mM compound in 0.01M PBS buffer at pH 7.4. RF saturation pulse was applied for 6 s ensuring complete saturation.
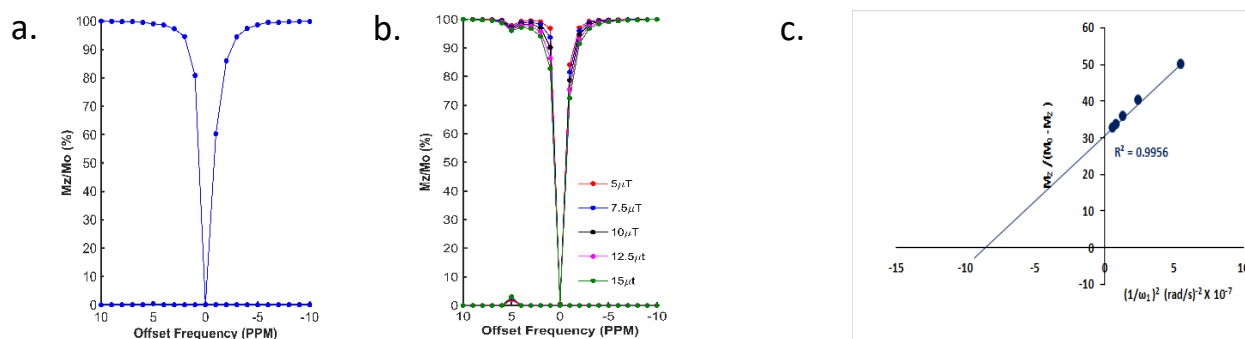
Figure 30: (a) z-spectra of 15mM 4-acetamidobenzoic acid (**5**) at 310K and at pH 7.4 recorded at 9.3T (b) Dependence of CEST percentage on saturation field strength ranging from 5 µT to 15 µT for (5) (c) Omega plot for exchange rate measurement. The expected linear relationship of $M_z/(M_0-M_z)$ as a function of $1/\omega_1^2$ $(rad/sec)^{-2}$ x 10^{-7} was obtained when recorded at 16.3 T of 15 mM compound in 0.01M PBS buffer at pH 7.4. RF saturation pulse was applied for 6 s ensuring complete saturation.
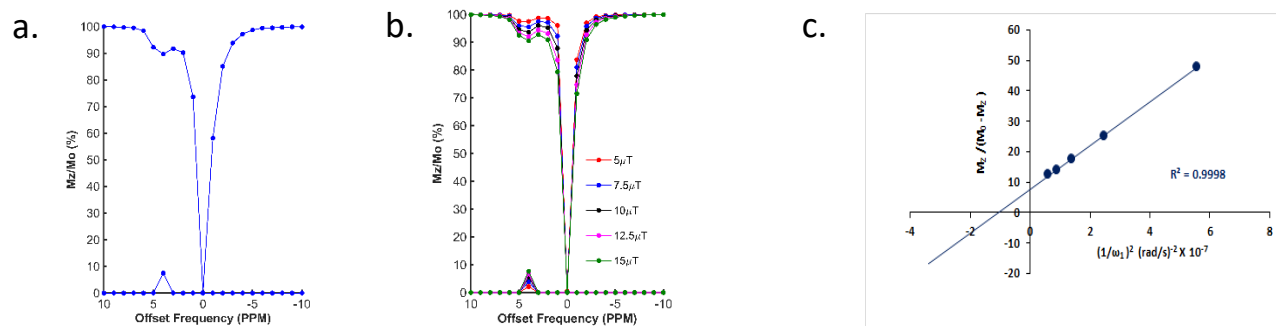
Figure 31: (a) z-spectra of 15mM N-(2-methoxyphenyl)acetamide (**6**) at 310K and at pH 7.4 recorded at 9.3T (b) Dependence of CEST percentage on saturation field strength ranging from 5 µT to 15 µT for (6) (c) Omega plot for exchange rate measurement. The expected linear relationship of $M_z/(M_0-M_z)$ as a function of $1/\omega_1^2$ (rad/sec)$^{-2}$ x 10^{-7} was obtained when recorded at 16.3 T of 15 mM compound in 0.01M PBS buffer at pH 7.4. RF saturation pulse was applied for 6 s ensuring complete saturatio
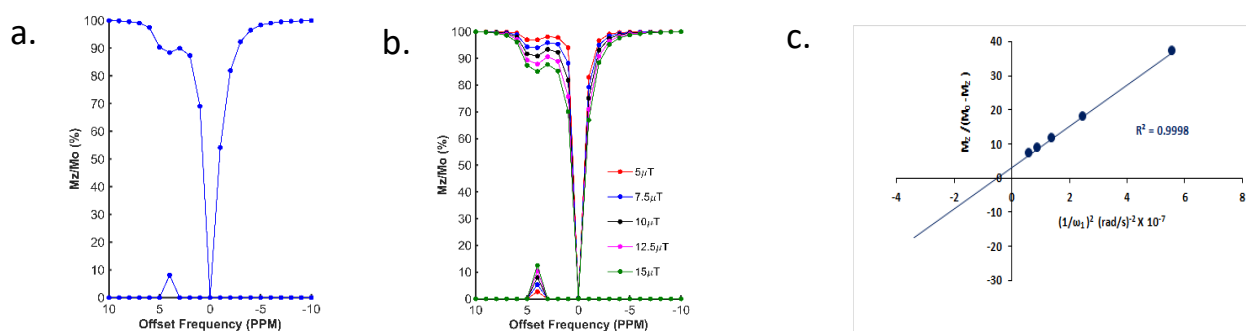
Figure 32: (a) z-spectra of 15mM N-(2-hydroxyphenyl)acetamide (**7**) at 310K and at pH 7.4 recorded at 9.3T (b) Dependence of CEST percentage on saturation field strength ranging from 5 µT to 15 µT for (7) (c) Omega plot for exchange rate measurement. The expected linear relationship of $M_z/(M_0-M_z)$ as a function of $1/\omega_1^2$ (rad/sec)$^{-2}$ x 10^{-7} was obtained when recorded at 16.3 T of 15 mM compound in 0.01M PBS buffer at pH 7.4. RF saturation pulse was applied for 6 s ensuring complete saturation.
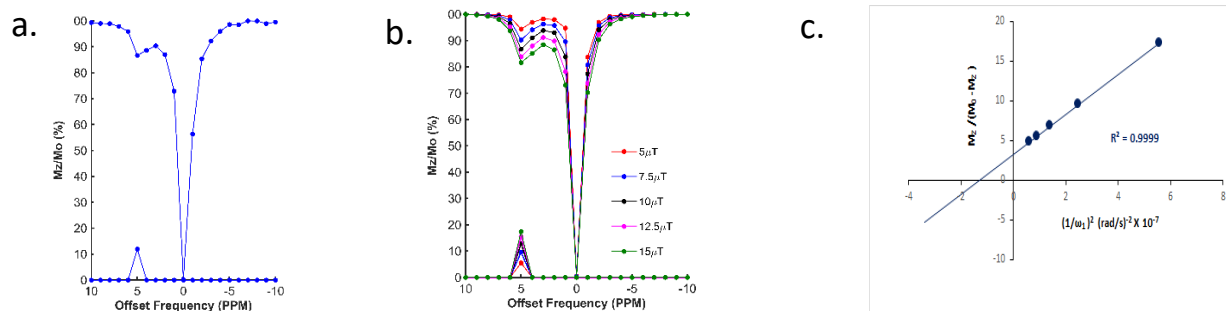

Figure 33: (a) z-spectra of 15mM N-(3-hydroxyphenyl)acetamide (**8**) at 310K and at pH 7.4 recorded at 9.3T (b) Dependence of CEST percentage on saturation field strength ranging from 5 µT to 15 µT for (8) (c) Omega plot for exchange rate measurement. The expected linear relationship of $M_z/(M_0-M_z)$ as a function of $1/\omega_1^2$ (rad/sec)$^{-2}$ x 10^{-7} was obtained when recorded at 16.3 T of 15 mM compound in 0.01M PBS buffer at pH 7.4. RF saturation pulse was applied for 6 s ensuring complete saturation.

3.3 Study of CEST properties of paracetamol. After exploring the electronic and steric influences of different substitutions on the CEST properties of acetanilide, we propose para-hydroxyl acetanilide (also known popularly as Paracetamol) as a potential CEST contrast agent. Paracetamol is a widely used analgesic having a proven safety track record for human consumption.[24] It is easily synthesizable in pure form from 4-aminophenol using the procedure discussed earlier. At ambient temperatures, paracetamol makes two-dimensional sheet through interMHB as shown in Figure. 34a.[25] Both the hydroxyl and the carbonyl oxygen atoms take part in an alternative arrangement to form the sheet. Figure. 34b shows the overlaid CEST z-spectra of paracetamol at physiological temperature of 37 °C and pH 7.4 in the buffer and two biological media, Fetal Bovine Serum (FBS) and Horse Serum (HS). At 15 mM concentration, paracetamol produces 12% contrast in the buffer as well as in biological media with 3 s saturation at 5 µT irradiation power. The CEST contrast increases with saturation duration (observed in buffer) and saturates at 15% above 6 s saturation duration (Figure. 34c).
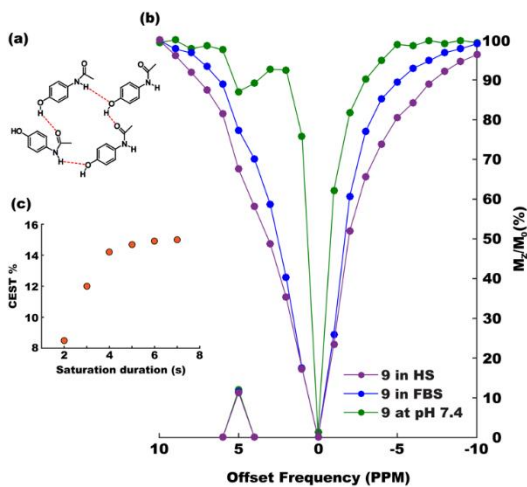
Figure 34 (a) The intermolecular hydrogen bond mediated molecular sheet formation by paracetamol.[23] (b) Overlaid z-spectra of 15 mM solutions of paracetamol in 10 mM (1X) PBS buffer (green), Fetal Bovine Serum (FBS, blue) and Horse Serum (HS, purple) at the physiological condition acquired with 3 s saturation with 5 µT power. (c) CEST efficiency (MTR$_{assym}$) as a function of saturation duration at 5 µT r.f. power.

Exchange rates between the two pools of protons, one constituted by the solute and the other by the solvent, dictates the efficiency of a CEST contrast agent. To ensure accurate measurement of exchange rates, all the experimental conditions required for exchange rate measurement using the method proposed by Dixon *et al*. were satisfied.[21] Long 6 s saturation was used for complete saturation (as indicated by Figure. 34c), the maximum power used was 639 Hz (corresponding to 15 µT field strength) which is well within $\Delta\omega$ = 3276 Hz at 16.4 T (the highest magnetic field available in the laboratory) and DS was measured to be less than 3% even with the maximum applied r.f power. Figure. 35a shows the overlaid z-spectra of paracetamol at different saturation fields at the physiological condition. The corresponding linear relationship between $M_Z/(M_0 - M_Z)$ and $1/\omega_1^2$ is shown in Figure. 35b for the physiological pH 7.4 and also for the two endpoints of the pH range (pH 7 and pH 8.1) for the current study. The goodness of linear fit is evident in all the plots. At the physiological condition, paracetamol shows an exchange rate of 1.26 ± 0.04 ks^{-1} which is well within the desired slow to medium exchange window.
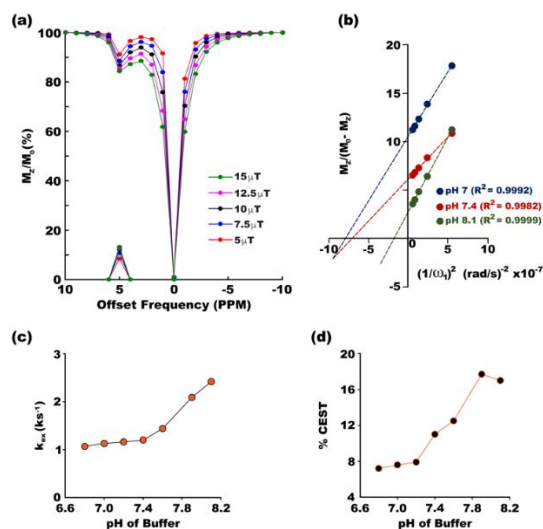
Figure 35 (a) Overlaid z-spectra of paracetamol at different irradiation powers with 3 s saturation in the physiological condition. The peaks on the x-axis show corresponding MTR$_{assym}$. (b) The linear fit for $M_Z/(M_0 - M_Z)$ plotted against $1/\omega_1^2$ for three pH values, 7, 7.4 and 8.1. The goodness of fitting is given by the R^2 values. Plots at other pH values are given in Figures. 36-41. Exchange rate constant (c) and CEST efficiency (d) at different pH of the medium show gradual increase of both at basic pH.

Paracetamol shows monotonically increasing exchange rate as the buffer pH moves from acidic to basic (Figure. 35c). Such a pattern is well observed in most CEST contrast agents. Following the thumb rule of CEST agents, the CEST efficiency also increases along with the exchange rate and reaches a maximum of 17.7% at pH 7.9 (Figure. 35d). However, the CEST efficiency drops marginally at a very basic pH of 8.1 due to exchange broadening. Figures 36-41 shows the exchange rate of paracetamol with varying pH.
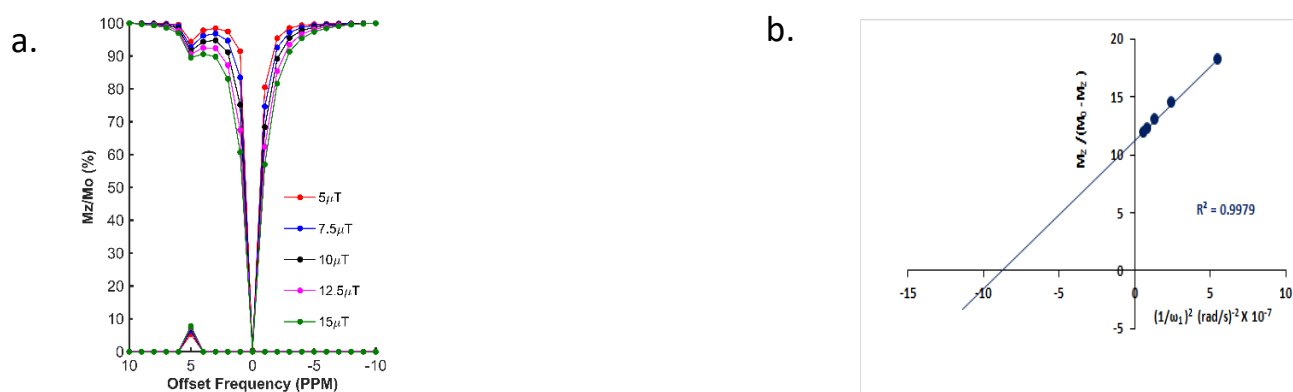
Figure 36: (a) Dependence of CEST percentage on saturation field strength ranging from 5 µT to 15 µT for N-(4-hydroxyphenyl) acetamide (**9**) at pH 6.8. (b) Omega plot for exchange rate measurement. The expected linear relationship of $M_z/(M_0-M_z)$ as a function of $1/\omega_1^2$ (rad/sec)$^{-2}$ x 10^{-7} was obtained when recorded at 16.3 T of 15 mM compound in 0.01M PBS buffer. RF saturation pulse was applied for 6 s ensuring complete saturation.
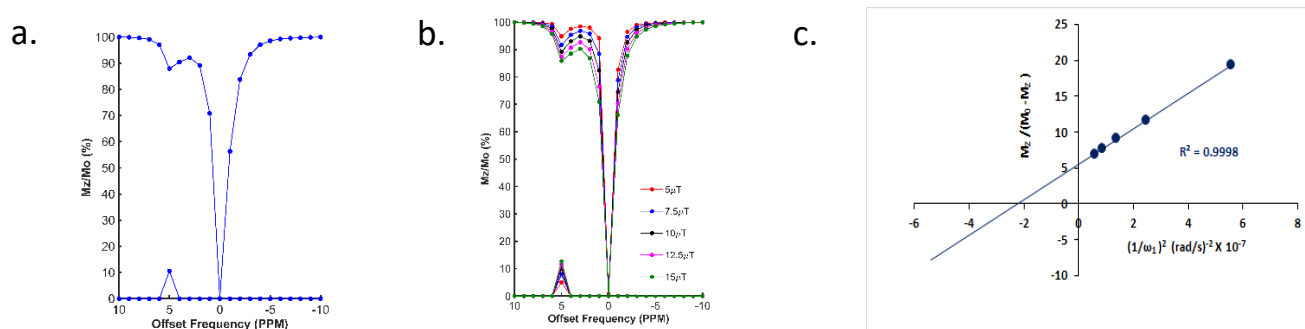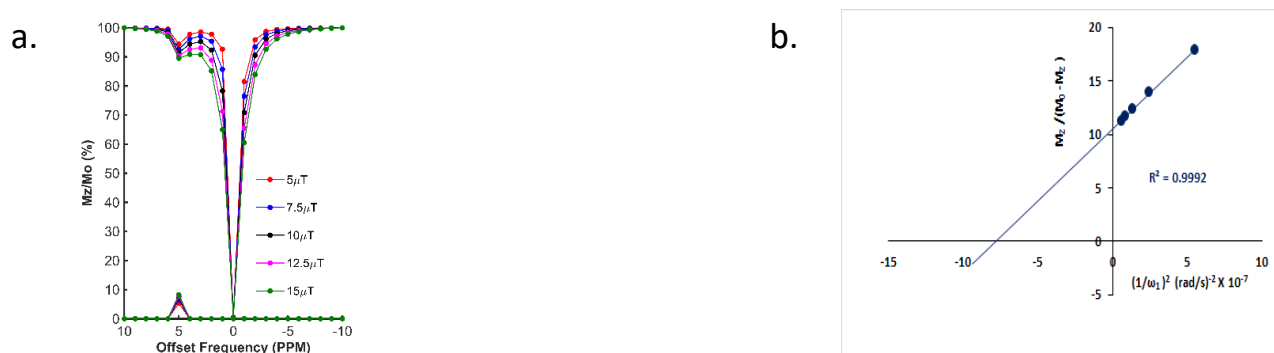

Figure 37: (a) Dependence of CEST percentage on saturation field strength ranging from 5 µT to 15 µT for N-(4-hydroxyphenyl) acetamide (**9**) at pH 7.0. (b) Omega plot for exchange rate measurement. The expected linear relationship of $M_z/(M_0-M_z)$ as a function of $1/\omega_1^2$ (rad/sec)$^{-2}$ x 10^{-7} was obtained when recorded at 16.3 T of 15 mM compound in 0.01M PBS buffer. RF saturation pulse was applied for 6 s ensuring complete saturation.
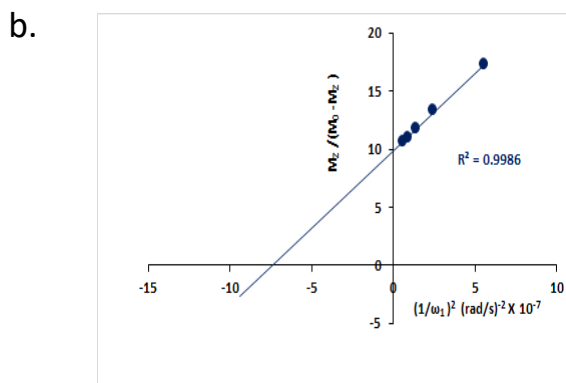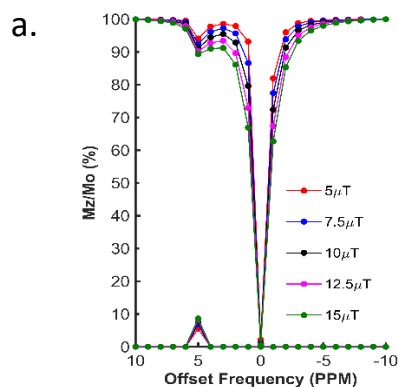
Figure 38: (a) Dependence of CEST percentage on saturation field strength ranging from 5 µT to 15 µT for N-(4-hydroxyphenyl) acetamide (**9**) at pH 7.2 (b) Omega plot for exchange rate measurement. The expected linear relationship of $M_z/(M_0-M_z)$ as a function of $1/\omega_1^2$ (rad/sec)$^{-2}$ x 10^{-7} was obtained when recorded at 16.3 T of 15 mM compound in 0.01M PBS buffer. RF saturation pulse was applied for 6 s ensuring complete saturation.
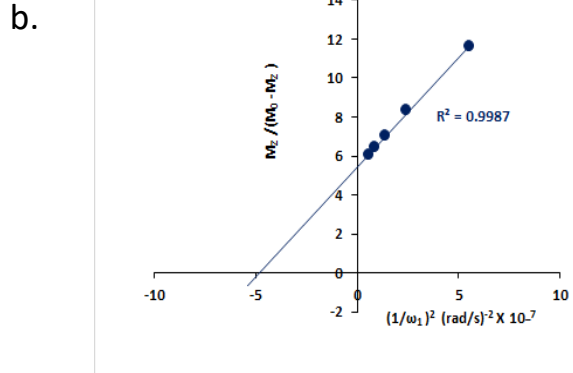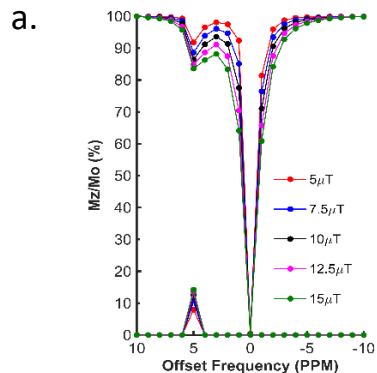
Figure 39: (a) Dependence of CEST percentage on saturation field strength ranging from 5 µT to 15 µT for N-(4-hydroxyphenyl) acetamide (**9**) at pH 7.6 (b) Omega plot for exchange rate measurement. The expected linear relationship of $M_z/(M_0-M_z)$ as a function of $1/\omega_1^2$ (rad/sec)$^{-2}$ x 10^{-7} was obtained when recorded at 16.3 T of 15 mM compound in 0.01M PBS buffer. RF saturation pulse was applied for 6 s ensuring complete saturation.
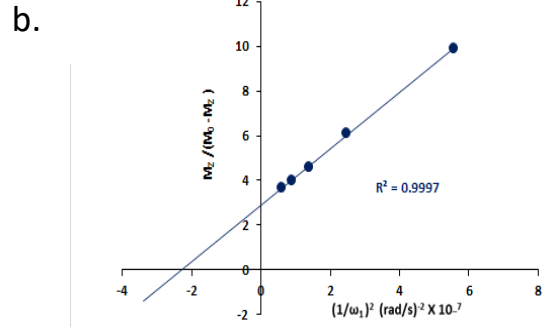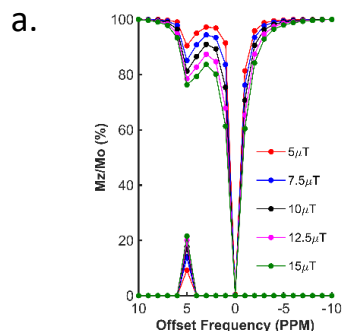
Figure 40: (a) Dependence of CEST percentage on saturation field strength ranging from 5 µT to 15 µT for N-(4-hydroxyphenyl) acetamide (**9**) at pH 7.9 (b) Omega plot for exchange rate measurement. The expected linear relationship of $M_z/(M_0-M_z)$ as a function of $1/\omega_1^2$ (rad/sec)$^{-2}$ x 10^{-7} was obtained when recorded at 16.3 T of 15 mM compound in 0.01M PBS buffer. RF saturation pulse was applied for 6 s ensuring complete saturation.

a.

b.
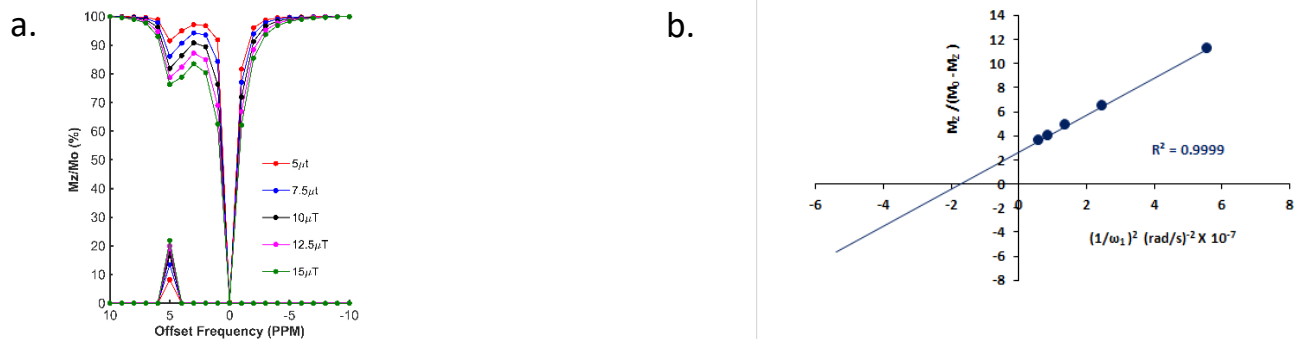
Figure 41: (a) Dependence of CEST percentage on saturation field strength ranging from 5 µT to 15 µT for N-(4-hydroxyphenyl) acetamide (**9**) at pH 8.1 .(b) Omega plot for exchange rate measurement. The expected linear relationship of $M_z/(M_0-M_z)$ as a function of $1/\omega_1^2$ $(rad/sec)^{-2}$ x 10^{-7} was obtained when recorded at 16.3 T of 15 mM compound in 0.01M PBS buffer. RF saturation pulse was applied for 6 s ensuring complete saturation.

Paracetamol has a proven safety record for human consumption. But even then it is always desired that any foreign object be administered in the human body at a minimal possible concentration. To check the efficiency of paracetamol as a CEST agent in the range of concentrations generally considered safe we recorded CEST spectra at six different concentrations ranging between 25 mM and 5 mM (Figure. 42a). The CEST contrast was found dropping nearly linearly from approximately 17% (25 mM) to 7% (5 mM) in the said range (Figure. 42b).
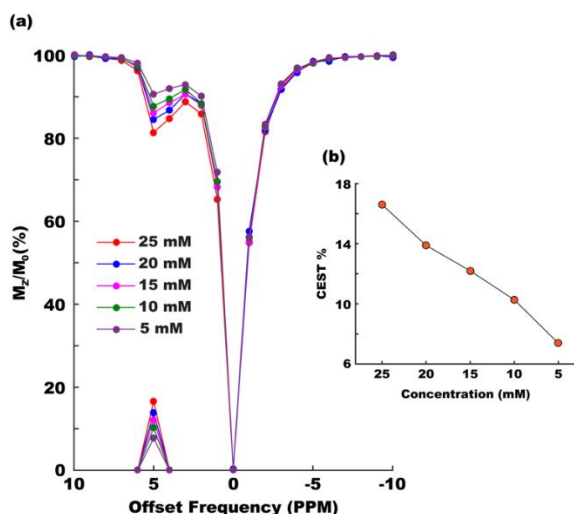
Figure. 42 CEST contrast efficiency of paracetamol at different concentrations between 5 mM and 25 mM. (a) Overlaid z-spectra and (b) MTR_{assym} as a function of concentration. All experiments were performed with 3 s saturation duration at 5 µT irradiation power.

Finally, we calculated the relaxivities of paracetamol by measuring concentration normalized changes in longitudinal (for R_1 relaxivity) and transverse (for R_2 relaxivity) relaxation times of water in presence of paracetamol. The R_1 and R_2 relaxivities of paracetamol were found, respectively, 0.02 s^{-1} mM^{-1} and 0.01 s^{-1} mM^{-1}. The calculated value for R_2 relaxivity matched a previous report where it has been discussed that the high relaxivity is due to the phenolic proton of paracetamol.[26] The phenolic proton executes a much faster exchange in comparison to the CEST producing amine proton and hence shows R_{2ex} contrast instead. This makes paracetamol a very special molecule in which two different labile protons produce MRI contrast following two completely different mechanisms.

4. Conclusions

In summary, we have demonstrated that the formation of molecular chains or sheets through inter-molecular hydrogen bonding can transform a collection of otherwise not suitable acetanilide derivatives into diamagnetic CEST MRI contrast agents. The hydrogen bonding network shifts the contrast producing labile protons downfield and lowers their exchange constants so optimally that the performance of the contrast agents peaks just about at the physiological condition. A notable member of the group is the well-known analgesic drug 'paracetamol' which shows 12% contrast with 15 mM concentration at the physiological temperature and pH. Paracetamol is regularly administered both orally and through intravenous route in humans and hence paracetamol has the potential of being used as either oral contrast agent (OCA)[27] or as extracellular fluid contrast agent (ECF).[27] Nearly 95% of paracetamol metabolism occurs in the liver and is generally considered safe for human consumption.[24] Although one can expect marginal drop in CEST efficiency at the lower magnetic field of clinical MRI scanner, we believe our findings make it a good candidate nonetheless for *in-vivo* applications as a diaCEST agent.

5. Spectral characterization

N-(4-Fluorophenyl)acetamide (**2**)[28]: ^{1}H NMR (400 MHz, DMSO) δ 9.97 (s, 1H), 7.60 – 7.56 (m, 2H), 7.12 (t, *J* = 8.9 Hz, 1H), 2.03 (s, 3H). ^{13}C NMR (176 MHz, DMSO) δ 168.60, 159.00, 157.64, 136.19, 121.24, 121.20, 115.66, 115.54, 24.28.

N-(4-Tolyl)acetamide (**3**)[29]: ^{1}H NMR (700 MHz, DMSO) δ 9.78 (s, 1H), 7.45 (d, *J* = 8.2 Hz, 2H), 7.08 (d, *J* = 8.2 Hz, 2H), 2.24 (s, 3H), 2.02 (s, 3H). ^{13}C NMR (176 MHz, DMSO) δ 168.50, 137.28, 129.45, 119.56, 24.35, 20.85.

N-(4-Methoxyphenyl)acetamide (**4**)[29]: ^{1}H NMR (400 MHz, DMSO) δ 9.76 (s, 1H), 7.47 (d, *J* = 9.1 Hz, 1H), 6.86 (d, *J* = 9.0 Hz, 1H), 3.71 (s, 3H), 2.00 (s, 3H). ^{13}C NMR (101 MHz, DMSO) δ 168.18, 155.48, 132.99, 121.00, 114.25, 55.60, 24.25.

4-Acetamidobenzoic acid (**5**)[30]: ^{1}H NMR (400 MHz, DMSO) δ 12.64 (s, 1H), 10.23 (s, 1H), 7.88 (d, *J* = 8.7 Hz, 2H), 7.69 (d, *J* = 8.8 Hz, 1H), 2.08 (s, 3H). ^{13}C NMR (101 MHz, DMSO) δ 169.33, 167.40, 143.80, 130.84, 125.36, 118.64, 24.62.

N-(2-Methoxyphenyl) acetamide (**6**)[31]: ^{1}H NMR (700 MHz, DMSO) δ 9.11 (s, 1H), 7.92 – 7.91 (m, 1H), 7.09 – 7.04 (m, 1H), 7.03 (dd, *J* = 8.2, 1.6 Hz, 1H), 6.89 (td, *J* = 7.7, 1.6 Hz, 1H), 3.83 (s, 3H), 2.08 (s, 3H). ^{13}C NMR (176 MHz, DMSO) δ 168.88, 150.00, 127.88, 124.65, 122.49, 120.61, 111.53, 56.05, 24.31.

N-(2-Hydroxyphenyl)acetamide (**7**)[32]: ^{1}H NMR (700 MHz, DMSO) δ 9.77 (s, 1H), 9.31 (s, 1H), 7.66 (dd, *J* = 8.0, 1.7 Hz, 1H), 7.01 – 6.91 (m, 1H), 6.86 (dd, *J* = 8.0, 1.5 Hz, 1H), 6.76 (t, *J* = 7.7 Hz, 1H), 2.09 (s, 3H). ^{13}C NMR (176 MHz, DMSO) δ 169.54, 148.36, 126.82, 125.16, 122.88, 119.44, 116.37, 24.03.

N-(3-Hydroxyphenyl)acetamide (**8**)[33]: ^{1}H NMR (700 MHz, DMSO) δ 9.78 (s, 1H), 9.33 (s, 1H), 7.18 (d, *J* = 2.1 Hz, 1H), 7.04 (t, *J* = 8.0 Hz, 1H), 6.91 (dd, *J* = 8.0, 2.0 Hz, 1H), 6.42 (dd, *J* = 8.0, 2.4 Hz, 1H), 2.01 (s, 3H). ^{13}C NMR (176 MHz, DMSO) δ 168.61, 158.01, 140.82, 129.73, 110.55, 110.18, 106.59, 24.52.

N-(4-hydroxyphenyl)acetamide (**9**)[34]: ^{1}H NMR (700 MHz, DMSO) δ 9.64 (s, 1H), 9.13 (s, 1H), 7.33 (d, *J* = 8.8 Hz, 2H), 6.67 (d, *J* = 8.7 Hz, 1H), 1.98 (s, 3H). ^{13}C NMR (176 MHz, DMSO) δ 167.96, 153.57, 131.50, 121.25, 115.4

References

1. V. P. B. Grover, J. M. Tognarelli, M. M. E. Crossey, I. J. Cox, S. D. Taylor-Robinson and M. J. W. McPhail, *Journal of clinical and experimental hepatology*, 2015, **5**, 246-255.

2. E. Seeram, *Radiol. Technol.*, 2018, **89**, 279CT-302CT.

3. (a) Y.-D. Xiao, R. Paudel, J. Liu, C. Ma, Z.-S. Zhang and S.-K. Zhou, *Int. J. Mol. Med.*, 2016, **38**, 1319-1326; (b) C. F. G. C. Geraldes and S. Laurent, *Contrast Media Mol. Imaging*, 2009, **4**, 1-23.

4. I. R. Young, G. J. Clarke, D. R. Baffles, J. M. Pennock, F. H. Doyle and G. M. Bydder, *J. Comput. Tomogr.*, 1981, **5**, 543-547.

5. (a) D. V. Hingorani, A. S. Bernstein and M. D. Pagel, *Contrast Media Mol. Imaging*, 2015, **10**, 245-265; (b) F. Ye, S. Laurent, A. Fornara, L. Astolfi, J. Qin, A. Roch, A. Martini, M. S. Toprak, R. N. Muller and M. Muhammed, *Contrast Media Mol. Imaging*, 2012, **7**, 460-468.

6. K. M. Ward, A. H. Aletras and R. S. Balaban, *J. Magn. Reson.*, 2000, **143**, 79-87.

7. (a) A. D. Sherry and M. Woods, *Annu. Rev. Biomed. Eng.*, 2008, **10**, 391-411; (b) P. C. M. van Zijl and N. N. Yadav, *Magn. Reson. Med.*, 2011, **65**, 927-948; (c) G. Liu, X. Song, K. W. Y. Chan and M. T. McMahon, *NMR Biomed.*, 2013, **26**, 810-828.

8. (a) S. Aime, M. Botta, M. Fasano and E. Terreno, *Chem. Soc. Rev.*, 1998, **27**, 19-29; (b) S. Aime, A. Barge, D. Delli Castelli, F. Fedeli, A. Mortillaro, F. U. Nielsen and E. Terreno, *Magn. Reson. Med.*, 2002, **47**, 639-648; (c) S. Aime, D. Delli Castelli and E. Terreno, *Angew. Chem. Int. Ed.*, 2002, **41**, 4334-4336; (d) S. Zhang, M. Merritt, D. E. Woessner, R. E. Lenkinski and A. D. Sherry, *Acc. Chem. Res.*, 2003, **36**, 783-790; (e) M. Woods, D. E. Woessner and A. D. Sherry, *Chem. Soc. Rev.*, 2006, **35**, 500-511; (f) S. Aime, D. D. Castelli, S. G. Crich, E. Gianolio and E. Terreno, *Acc. Chem. Res.*, 2009, **42**, 822-831; (g) S. Viswanathan, Z. Kovacs, K. N. Green, S. J. Ratnakar and A. D. Sherry, *Chem. Rev.*, 2010, **110**, 2960-3018; (h) I. Hancu, W. T. Dixon, M. Woods, E. Vinogradov, A. D. Sherry and R. E. Lenkinski, *Acta Radiol.*, 2010, **51**, 910-923; (i) P. B. Tsitovich, J. M. Cox, J. A. Spernyak and J. R. Morrow, *Inorg. Chem.*, 2016, **55**, 12001-12010; (j) P. J. Burns, J. M. Cox and J. R. Morrow, *Inorg. Chem.*, 2017, **56**, 4545-4554; (k) R. N. Pradhan, S. Chakraborty, P. Bharti, J. Kumar, A. Ghosh and A. K. Singh, *Dalton Trans.*, 2019, **48**, 8899-8910.

9. C. Rydahl, H. S. Thomsen and P. Marckmann, *Invest. Radiol.*, 2008, **43**, 141-144.

10. (a) P. C. van Zijl, C. K. Jones, J. Ren, C. R. Malloy and A. D. Sherry, *Proc. Natl. Acad. Sci. U. S. A.*, 2007, **104**, 4359-4364; (b) W. Ling, R. R. Regatte, G. Navon and A. Jerschow, *Proc. Natl. Acad. Sci. U. S. A.*, 2008, **105**, 2266; (c) M. Haris, K. Cai, A. Singh, H. Hariharan and R. Reddy, *Neuroimage*, 2011, **54**, 2079-2085; (d) K. Cai, M. Haris, A. Singh, F. Kogan, J. H. Greenberg, H. Hariharan, J. A. Detre and R. Reddy, *Nat. Med.*, 2012, **18**, 302-306; (e) G. Liu, M. Moake, Y.-e. Har-el, C. M. Long, K. W. Y. Chan, A. Cardona, M. Jamil, P. Walczak, A.

A. Gilad, G. Sgouros, P. C. M. van Zijl, J. W. M. Bulte and M. T. McMahon, *Magn. Reson. Med.*, 2012, **67**, 1106-1113; (f) K. W. Y. Chan, M. T. McMahon, Y. Kato, G. Liu, J. W. M. Bulte, Z. M. Bhujwalla, D. Artemov and P. C. M. van Zijl, *Magn. Reson. Med.*, 2012, **68**, 1764-1773; (g) A. Bar-Shir, G. Liu, M. M. Greenberg, J. W. M. Bulte and A. A. Gilad, *Nat. Protoc.*, 2013, **8**, 2380-2391; (h) A. Bar-Shir, G. Liu, Y. Liang, N. N. Yadav, M. T. McMahon, P. Walczak, S. Nimmagadda, M. G. Pomper, K. A. Tallman, M. M. Greenberg, P. C. M. van Zijl, J. W. M. Bulte and A. A. Gilad, *J. Am. Chem. Soc.*, 2013, **135**, 1617-1624; (i) K. W. Y. Chan, G. Liu, X. Song, H. Kim, T. Yu, D. R. Arifin, A. A. Gilad, J. Hanes, P. Walczak, P. C. M. van Zijl, J. W. M. Bulte and M. T. McMahon, *Nat. Mater.*, 2013, **12**, 268-275; (j) S. Walker-Samuel, R. Ramasawmy, F. Torrealdea, M. Rega, V. Rajkumar, S. P. Johnson, S. Richardson, M. Gonçalves, H. G. Parkes, E. Arstad, D. L. Thomas, R. B. Pedley, M. F. Lythgoe and X. Golay, *Nat. Med.*, 2013, **19**, 1067-1072; (k) M. Haris, A. Singh, K. Cai, K. Nath, R. Crescenzi, F. Kogan, H. Hariharan and R. Reddy, *J. Neurosci. Methods*, 2013, **212**, 87-93; (l) A. Bar-Shir, G. Liu, K. W. Y. Chan, N. Oskolkov, X. Song, N. N. Yadav, P. Walczak, M. T. McMahon, P. C. M. van Zijl, J. W. M. Bulte and A. A. Gilad, *ACS Chem. Biol.*, 2014, **9**, 134-138; (m) K. W. Chan, T. Yu, Y. Qiao, Q. Liu, M. Yang, H. Patel, G. Liu, K. W. Kinzler, B. Vogelstein, J. W. Bulte, P. C. van Zijl, J. Hanes, S. Zhou and M. T. McMahon, *J. Control. Release*, 2014, **180**, 51-59; (n) K. W. Y. Chan, J. W. M. Bulte and M. T. McMahon, *WIREs Nanomed. and Nanobiotechnol.*, 2014, **6**, 111-124; (o) S. Maruyama, J. Ueda, A. Kimura and K. Murase, *Magn. Reson. Med. Sci.*, 2016, **15**, 324-334.

11. (a) X. Yang, X. Song, Y. Li, G. Liu, S. Ray Banerjee, M. G. Pomper and M. T. McMahon, *Angew. Chem. Int. Ed.*, 2013, **52**, 8116-8119; (b) W. G. Lesniak, N. Oskolkov, X. Song, B.

Lal, X. Yang, M. Pomper, J. Laterra, S. Nimmagadda and M. T. McMahon, *Nano Lett.*, 2016, **16**, 2248-2253.

12. X. Song, X. Yang, S. Ray Banerjee, M. G. Pomper and M. T. McMahon, *Contrast Media Mol. Imaging*, 2015, **10**, 74-80.

13. X. Yang, N. N. Yadav, X. Song, S. Ray Banerjee, H. Edelman, I. Minn, P. C. M. van Zijl, M. G. Pomper and M. T. McMahon, *Chem. Eur. J.*, 2014, **20**, 15824-15832.

14. X. Yang, X. Song, S. Ray Banerjee, Y. Li, Y. Byun, G. Liu, Z. M. Bhujwalla, M. G. Pomper and M. T. McMahon, *Contrast Media Mol. Imaging*, 2016, **11**, 304-312.

15. (a) X. Zhang, Y. Yuan, S. Li, Q. Zeng, Q. Guo, N. Liu, M. Yang, Y. Yang, M. Liu, M. T. McMahon and X. Zhou, *Magn. Reson. Med.*, 2019, **82**, 577-585; (b) S. Chakraborty, M. Das, A. Srinivasan and A. Ghosh, *New J. Chem.*, 2020, DOI: 10.1039/D0NJ04869K.

16. (a) S. Aime, L. Calabi, L. Biondi, M. De Miranda, S. Ghelli, L. Paleari, C. Rebaudengo and E. Terreno, *Magn. Reson. Med.*, 2005, **53**, 830-834; (b) D. L. Longo, W. Dastrù, G. Digilio, J. Keupp, S. Langereis, S. Lanzardo, S. Prestigio, O. Steinbach, E. Terreno, F. Uggeri and S. Aime, *Magn. Reson. Med.*, 2011, **65**, 202-211; (c) D. L. Longo, P. Z. Sun, L. Consolino, F. C. Michelotti, F. Uggeri and S. Aime, *J. Am. Chem. Soc.*, 2014, **136**, 14333-14336; (d) S. Sinharay, E. A. Randtke, C. M. Howison, N. A. Ignatenko and M. D. Pagel, *Mol. Imaging Biol.*, 2018, **20**, 240-248; (e) X. Cai, J. Zhang, J. Lu, L. Yi, Z. Han, S. Zhang, X. Yang and G. Liu, *Chem. Eur. J.*, 2020, **26**, 11705-11709.

17. (a) A. Greenberg, C. M. Breneman and J. F. Liebman, *The Amide Linkage: Structural Significance in Chemistry, Biochemistry, and Materials Science*, Wiley, pp; (b) J. Pitzer and K. Steiner, *J. Biotechnol.*, 2016, **235**, 32-46; (c) A. K. Agrahari, A. K. Singh, A. S. Singh, M. Singh, P. Maji, S. Yadav, S. Rajkhowa, P. Prakash and V. K. Tiwari, *New J. Chem.*, 2020, **44**,

19300-19313; (d) C. W. Evans, S. Edwards, J. A. Kretzmann, G. L. Nealon, R. Singh, T. D. Clemons, M. Norret, C. A. Boyer and K. S. Iyer, *New J. Chem.*, 2020, **44**, 20013-20020; (e) S. Zhang, J. Li, J. Li, N. Du, D. Li, F. Li and J. Man, *RSC Advances*, 2020, **10**, 34308-34322; (f) L. Posada, D. Davyt and G. Serra, *RSC Advances*, 2020, **10**, 43653-43659.

18. J. Binoy, N. B. Prathima, C. Murali Krishna, C. Santhosh, I. Hubert Joe and V. S. Jayakumar, *Laser Physics*, 2006, **16**, 1253-1263.

19. B. J. Anderson, *Pediatric Anesthesia*, 2008, **18**, 915-921.

20. B. S. Furniss, A. J. Hannaford, P. W. G. Smith and A. R. Tatchell, *Vogel's textbook of practical organic chemistry*, Longman Scientific & Technical, 5th edn., pp. 985, 1989.

21. W. T. Dixon, J. Ren, A. J. M. Lubag, J. Ratnakar, E. Vinogradov, I. Hancu, R. E. Lenkinski and A. D. Sherry, *Magn. Reson. Med.*, 2010, **63**, 625-632.

22. D. H. Wu, A. D. Chen and C. S. Johnson, *Journal of Magnetic Resonance, Series A*, 1995, **115**, 260-264.

23. C. C. Miller and J. Walker, *Proceedings of the Royal Society of London. Series A, Containing Papers of a Mathematical and Physical Character*, 1924, **106**, 724-749.

24. (a) L. L. Mazaleuskaya, K. Sangkuhl, C. F. Thorn, G. A. FitzGerald, R. B. Altman and T. E. Klein, *Pharmacogenetics and genomics*, 2015, **25**, 416-426; (b) J. A. Forrest, J. A. Clements and L. F. Prescott, *Clin. Pharmacokinet.*, 1982, **7**, 93-107.

25. G.-W. An, H. Zhang, X.-L. Cheng, Q.-L. Zhuo and Y.-C. Lv, *Struct. Chem.*, 2008, **19**, 613.

26. J. Zhang, Y. Li, S. Slania, N. N. Yadav, J. Liu, R. Wang, J. Zhang, M. G. Pomper, P. C. van Zijl, X. Yang and G. Liu, *Chem. Eur. J.*, 2018, **24**, 1259-1263.

27. Y.-D. Xiao, R. Paudel, J. Liu, C. Ma, Z.-S. Zhang and S.-K. Zhou, *Int. J. Mol. Med.*, 2016, **38**, 1319-1326.

28. G. K. S. Prakash, M. D. Moran, T. Mathew and G. A. Olah, *J. Fluorine Chem.*, 2009, **130**, 806-809.

29. S. R. Thopate, S. R. Kote, S. V. Rohokale and N. M. Thorat, *J. Chem. Res.*, 2011, **35**, 124-125.

30. S. Mönch, M. Netzel, G. Netzel and M. Rychlik, *Anal. Biochem.*, 2010, **398**, 150-160.

31. B. P. Fors, K. Dooleweerdt, Q. Zeng and S. L. Buchwald, *Tetrahedron*, 2009, **65**, 6576-6583.

32. R. Moreno-Corral, H. Höpfl, L. Machi-Lara and K. O. Lara, *Eur. J. Org. Chem.*, 2011, DOI: https://doi.org/10.1002/ejoc.201001312, 2148-2162.

33. S. S. van Berkel, B. van der Lee, F. L. van Delft and F. P. J. T. Rutjes, *Chem. Commun. (Cambridge, U. K.)*, 2009, DOI: 10.1039/B906762K, 4272-4274.

34. A. S. El-Shahawy, S. M. Ahmed and N. K. Sayed, *Spectrochimica Acta Part A: Molecular and Biomolecular Spectroscopy*, 2007, **66**, 143-152.

CHAPTER 5

Optimization of experimental NMR parameters towards enhanced diaCEST efficiency

1. Introduction

Chemical exchange saturation transfer-based contrast agents work in a fundamentally different way compared to the relaxation-based contrast agents.[1-2] Selective saturation of exchangeable protons of the solute resonating away from bulk water followed by chemical exchange of the saturated proton with that of the bulk water reduces the bulk water signal intensity.[3] Saturation transfer-based contrast agents have emerged as a powerful technique for contrast generation in MRI as just by tweaking few experimental parameters, an image with zero contrast can readily be obtained compared to the relaxation based contrast agent where the contrast cannot be removed once the agent have been injected. The CEST agents are broadly classified based on the presence (paraCEST)[4-5] or absence (diaCEST)[6] of the paramagnetic metal center. The resonance frequency of the exchangeable solute proton in paraCEST agents are way higher than their diamagnetic counterpart and therefore they are capable of producing high contrast.[7-8] On the other hand, the diaCEST agents produce less contrast as the offset of the exchangeable solute proton is comparatively less. However, they are considered to be physiologically safe due to the absence of any metal center.[9-13] In order to screen or develop saturation transfer-based contrast agent successfully a synergy between the experimental NMR parameters as well as the electronic properties of the molecule is advocated. A potential CEST contrast agent can show drastically detrimental effect because of inappropriate selection of experimental NMR parameters. Similarly, misfit of the electronic properties of a molecule can heavily slump the percentage of CEST contrast.

The outcome of any CEST experiment depends not only on the molecule itself, but also upon suitable choice of acquisition parameters. The parameters are so intertwined that slight maladjustment of any of them produces a compelling effect on the other parameters. Apart from

the acquisition parameters, another factor that plays a key role in producing optimal CEST contrast is the strength of the main magnetic field (B_0). Among the parameters, we present here the study of the effect of four key parameters namely pulse length, relaxation delay, saturation duration and pulse shape on CEST efficiency. While many of the effects are already known,[14-15] we wish to revisit and see if a careful tuning of parameters can enhance the efficiency of diaCEST agent. We have therefore chosen salicylic acid as the sample as it has widely been investigated elsewhere. Salicylic acid and their analogues are high performing diaCEST agent owing to their CEST producing highly down fielded phenol OH protons.[16-17] In this chapter we demonstrate that well harmonized adjustment of the NMR experimental parameters can improve the CEST percentage further.

2. Experiments and methods:

2.1 Sample preparation and instrumentation: 25 mM salicylic acid solution was prepared by dissolving 1.72 mg of salicylic acid in 400 microliter phosphate buffer saline (1X). pH was adjusted to 7.4 (physiological pH) by suitably using 0.5 (M) NaOH and/or 0.5 (M) HCl solution. pH measurement were performed using an Eutech pH meter, before acquiring NMR experiments at the physiological temperature of 37^0 C (310 K). All NMR experiments were performed at the physiological condition (310 K temperature and pH 7.4) on a 9.4 T Bruker AVANCE-III nanobay spectrometer equipped with a BBFO broadband probe, except for the experiments where the effect of field strength on CEST percentage were calculated. Those were performed on a 16.4 T Bruker AVANCE-III AV700 ascend spectrometer equipped with a triple resonance room temperature probe. D_2O filled capillaries were placed co-axially inside the NMR tube for deuterium lock. Methanol-d4 was used to calibrate the probe temperature before acquiring each NMR experiment.

2.2 Preparation of CEST z-spectra: CEST experiments were acquired with a radiofrequency field of 7.5 µT (319.5 Hz), similar to the one previously reported by McMohan et.al. to compare the effect of other NMR parameter optimization towards tuning the CEST efficiency.(8) Data were obtained at a resolution of 1ppm and the normalized intensity of water signal (100 x M_z/M_0) was plotted against the frequency offsets to obtain the z-spectra. M_z and M_0 denote the intensities of the water peak, respectively, with and without on-resonance saturation. Asymmetric magnetization transfer ratio, as given below, was used to calculate the CEST contrast.

$$\%\text{Contrast} = \frac{M(-\Delta\omega) - M(\Delta\omega)}{M(-\Delta\omega)} X100\% \qquad (1),$$

where, $M(\Delta\omega)$ represents the water signal intensity after saturation is incurred on resonance (at the resonance frequency of the exchangeable proton having an offset of $\Delta\omega$ with respect to bulk water), and $M(-\Delta\omega)$ represents the water signal intensity at an equal offset on the other side of the water peak. All the processing and plotting were performed using in-house MATLAB (R2014b) scripts.

3. Results and discussion

3.1 Pulse length: For a low power long irradiation, the transverse magnetization intensity profile generated through excitation matches with the Fourier transform of the pulse shape. Selection of an appropriate shaped pulse is therefore necessary to get an optimal CEST contrast. This is also important as, to minimize the perturbation in physiological condition inside the tissue, concentration of CEST agent is used in mM range. Selective saturation is done best when the duration of the shaped pulse is matched to the inverse of the full width at half maximum (FWHM)

of the exchangeable proton. This ensures maximum signal to noise ratio through excitation of the entire region of interest. As the exchange rate of the exchangeable proton in a typical diaCEST agent lies in the slow to medium exchange range, the exchangeable peak generally shows relatively high FWHM requiring the pulse width adjusted very accurately. One of the important factors, that governs the selectivity of different shapes, is their corresponding bandwidth factors. The bandwidth factor of a shaped pulse is a dimensionless quantity and is directly related to the width of excitation profile of the pulse and is given by the equation $\Delta f = F/\Delta t$, where F is the bandwidth factor of the shaped pulse and Δf and Δt correspond, respectively, to the excitation bandwidth (in Hz) and duration of the shaped pulse (in seconds). Thus, for a given bandwidth factor higher pulse length brings in more selectivity through excitation of a narrower region, as Δf and Δt are inversely related by the uncertainty principle. Bandwidth factor therefore becomes pivotal to get the best saturation result. For example, the Gaussian shape and the smooth square shape have the bandwidth factor of 0.88 and 1.12, respectively. According to the equation mentioned above, given the same pulse length of 50ms, Gaussian pulse and Smooth-square pulse would excite the regions of 17.6 Hz and 22.4 Hz, respectively. As a rule of thumb, lower the bandwidth factor, better is the selectivity of a shape.

We carried out CEST experiments with salicylic acid at 7.5 µT peak radiofrequency field with a moderate 3 s total saturation duration but with varying individual pulse widths (Figure 1). We found that there is no considerable effect of increasing or decreasing the pulse length on the CEST efficiency given a fixed total saturation duration. The individual pulse widths can be set to almost any value as long as other pulse length related characteristics (discussed below) are properly taken care of.

A typical Z-spectrum has few relevant characteristics. CEST percentage from a Z-spectrum is

calculated from the intensity drop of the water magnetization with saturation at $+\Delta\omega$ and $-\Delta\omega$ from

water, where $\Delta\omega$ corresponds to the offset of the solute. In order to detect correctly the intensity

drop due to saturation transfer of any exchangeable proton close to water, the direct saturation

(DS) profile resulting from saturation of bulk water, should be narrowed down as much as

possible.
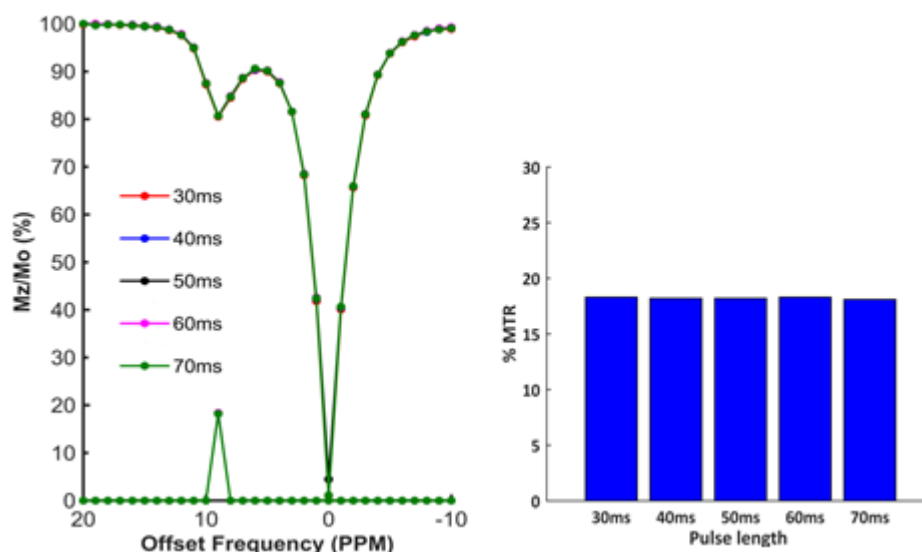
Figure 1: Effect of pulse length on the CEST profile of 25 mM salicylic acid. Sinc shaped pulse was used for saturation with a saturation duration of 3 s and a relaxation delay of 5 s while the RF field was set at 7.5 μT.

A narrow water DS profile also eliminates the possibility of spurious calculation of CEST

contrast efficiency. With too low pulse width, significant amount of unwanted magnetization will

also be saturated. On the other hand, too much increase of the pulse length is also not advisable

as it would not be able to fully saturate a broad peak..

3.2 Relaxation delay: Relaxation delay is an important experimental parameter in any saturation

transfer based experiment. In general, for any NMR experiment the recycle delay should be at

least five times of the longest T_1 present in the system. It serves two purposes. First, it allows the

magnetization to attain the equilibrium condition before the next scan, and second, it helps to satisfy the duty cycle requirement to prevent excessive sample heating. This is of utmost importance in saturation transfer experiments as with increasing temperature the exchange rate of a compound increases. If at an elevated temperature, the exchange rate of the solute breaches the limit of the chemical shift offset of the exchangeable proton then the CEST percentage drops drastically due to coalescence.

To experimentally observe the effect of relaxation delay on CEST efficiency, a series of CEST experiments have been acquired with the relaxation delay varied between 4 s and 10 s. Saturation duration was kept constant at 3 s in all the experiments. It is worth mentioning that the relaxation delay includes the saturation duration. With the saturation duration unchanged, the efficiency of saturation was kept constant in all the experiments. With the increase in relaxation delay the CEST percentage very surprisingly decreased slightly from 17 % at 4 s to approximately 15 % at 10 s in a saturating way (Figure 2).

The fact that it saturated close to about 3 times T_1 of water, led us to believe that it is coming from a sort of memory effect. The standard *stddiff* pulse sequence we employed for the CEST experiment consists of an eight-step phase cycle. If the saturation that is incurred upon the exchangeable proton and transferred to water in one cycle is retained to some extent and gets added up to the next cycle due to quick repetition ($d_1 << 3T_{1,water}$), such an effect might be observed. As a result, we observed a false enhancement, albeit very small, of the CEST efficiency which is not desired. In order to avoid such false exaggeration a sufficiently long relaxation delay needs to be used to obtain the correct CEST percentage. With water T_1 close to 3 s, the relaxation delay (including saturation duration) should be ideally about 9 s for multi-scan *in-vitro* studies.

The observation we made has a serious implication. While the demand of long relaxation delay increases the overall experiment time, a short relaxation delay might help in *in-vivo* studies where high contrast can be achieved can be achieved by cumulative effect from multiple scans. That is of-course with SAR requirements be honored.
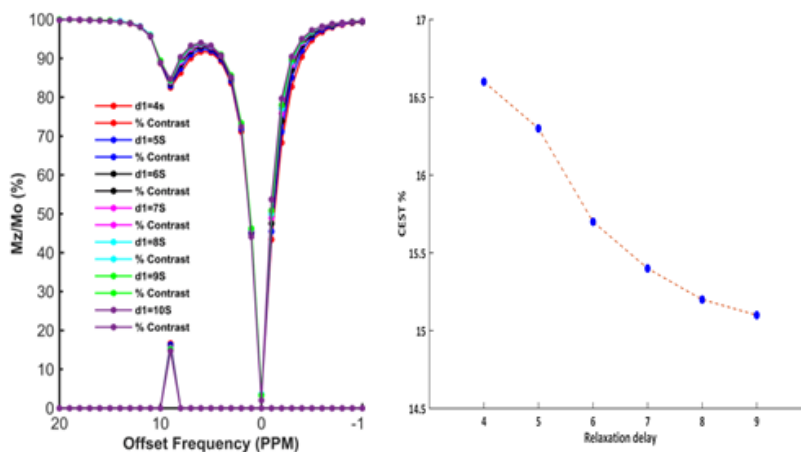
Figure 2: Effect of relaxation delay on the CEST profile of 25 mM salicylic acid. Sinc shaped pulse was used for saturation with a saturation duration of 3 s and relaxation delay was varied from 4 s to 9 s while the RF field was set at 7.5 µT.

3.3 Saturation duration: Administration of CEST contrast agent beyond a certain concentration is not advisable for *in-vivo* applications as it might change the physiological environment of the local tissue. For a solute having a concentration in milimolar range, it is practically impossible to produce any desirable effect of decreased proton density of the bulk water by a "single" transfer of saturation from the exchangeable protons of the solute, particularly when the solvent concentration is as high as 55.55 M. The way out is two-fold. First, the exchange rate of a potential CEST agent should fall in the slow to medium exchange range and second, the saturation duration should be long enough to facilitate multiple exchange events. Considering a two site exchange model, the residence time of a proton corresponding to slow to medium exchange regime is in

millisecond range. Selective saturation of several seconds then is capable of producing considerable CEST effect through several thousand exchange events during that time even with a solute concentration lying in the millimolar range.

With increasing saturation duration the CEST percentage increases as more number of solute are saturated and the saturation is transferred to the bulk water efficiently. However, with increasing saturation duration at some point the CEST percentage saturates.

At this point we compare three different categories of diaCEST agents and their response to CEST percentage as a function of saturation duration. In the third chapter we have discussed about TmPyP as a potential diaCEST contrast agent. The free base porphyrin is soluble in water and produces CEST effect due to the presence of a counter anion which stabilizes the positive charge on the meso-pyridyl carbocation. In the next chapter we discussed that para-hydroxy acetanilide (paracetamol) can produce CEST because of the presence of inter-molecular hydrogen bond which reduces the exchange rate of the labile amine proton to slow to medium exchange regime with respect to the NMR time scale. Salicylic acid on the other hand shows appreciable CEST effect when at neutral or slightly basic pH due to the intra-molecular hydrogen bond between the hydroxyl proton and the carboxylate anion.

When we plotted the CEST percentages of these three different solutes against the saturation duration (Figure 3), we found that they follow a similar pattern. For all of them, with the increase of saturation duration the CEST percentage first increases and then saturates at about 9 s. This is because water starts losing incurred saturation around ~9 s which is roughly three times the T_1 of water.

Consequently, those factors which can alter the longitudinal relaxation time constant of bulk

water can potentially alter the saturation duration at which the CEST percentage of a particular solute saturates.

Paracetamol and salicylic acid both have comparable exchange rate. However the pKa of paracetamol (9.5) is way higher than the pka of salicylic acid (2.7). As a result, given the same exchange rate lying in the slow to medium exchange regime with respect to the NMR time scale, the hydroxyl proton of salicylic acid possesses high lability compared to the amine proton of paracetamol. Consequently salicylic acid shows a higher CEST percentage compared to paracetamol at the same saturation duration.
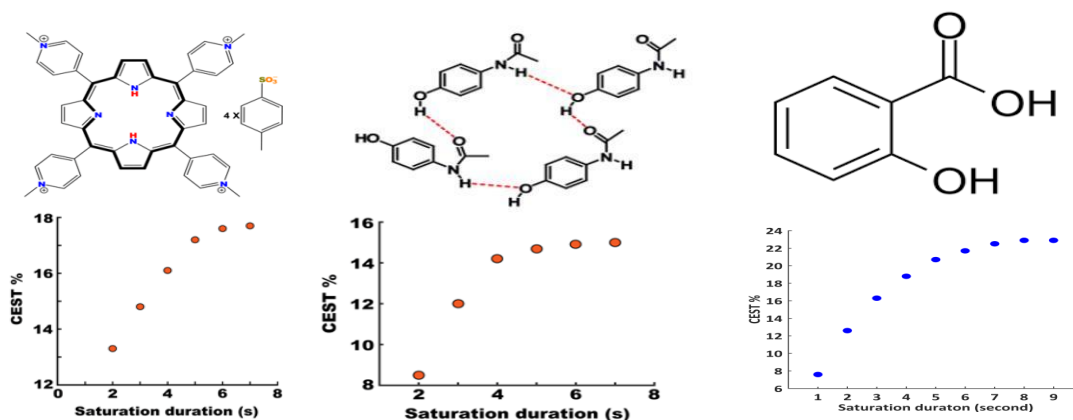
Figure 3: Effect of saturation duration on the CEST profile of TmPyp, Paracetamol and Salicylic acid.

TmPyP on the other hand possesses a higher exchange rate compared to paracetamol and salicylic acid. However the pKa of TmPyP (6.6) is intermediate to that of paracetamol and salicylic acid and as a result it shows a intermediate CEST percentage at the same saturation duration.

Therefore, the CEST percentage of any solute containing exchangeable proton is result of the combined effect of pKa as well as exchange rate. If the exchange rate lies in the CEST favorable

regime then the pKa is of utmost importance in deciding the CEST percentage with a given saturation duration.

In case of magnetic resonance imaging, paramount importance is given for the specific absorption rate (SAR) requirements. The SAR describes the potential for heating of the patient's tissue due to the application of RF energy. To avoid or minimize the effect of such complications, the frequency and power of the radiofrequency should be kept at the lowest possible level.

Although a long saturation duration is needed for efficient saturation, and hence for an increase in the CEST percentage to a certain value, long irradiation also increases the rf power depositions, before it ceases to saturate. Total irradiation duration should not be increased beyond the limit of specific absorption rate (SAR) recommendations. Any CEST agent that needs longer than normal (~2-3 s) saturation time or higher than normal power (~ 5 µT) to extract meaningful CEST contrast will therefore have a lesser probability to be used a potential *in-vivo* contrast agent.

3.4 Pulse shape: The CEST pulse sequence consists of a saturation block followed by a readout pulse to detect the apparent proton density loss of the bulk water resulting from the saturation transfer. The saturation block is implemented to carry out selective saturation of the exchangeable solute protons. For a selective on-resonance excitation, the effective field lies very close to the principal axis of rotation and hence the offset (Ω) becomes comparable to the RF field strength (ω_1). As a result, the RF field used for the excitation is comparatively less than the conventional non-selective pulse. The long pulse length that is required for selectivity thus gets compensated. Put together the duty cycle requirement gets satisfied. Continuous wave rectangular pulses are frequently used in saturation transfer MRI as this allows a rapid and efficient

saturation of the exchangeable protons. Additionally, numerical solution of the Bloch equations becomes simpler using rectangular pulses allowing faster computation of required RF field strength. In rectangular pulses, only the saturation power (B_1) and the duration of saturation (t_{sat}) need to be optimized for efficient saturation.[18] The optimum RF field required for generating best contrast for a given a contrast agent, having exchange rate k_{sw}, is estimated to be $k_{sw}/2\pi$.[19] The contrast to noise ratio should also be considered while RF saturation is optimized, as the direct saturation and magnetization transfer contrast also increases with increasing saturation field strength. Sun et. al. demonstrated the correlation between CEST contrast, direct saturation and RF field strength using an analytical solution of the Bloch equations.[20] Using the expression derived by Sun et.al., the optimum B_1 required to achieve the maximum proton transfer ratio for poly-L-lysine was found to be in accordance with the experimental value. This optimum RF field is independent of the agent concentration. Despite the complicacy of the equation, it can be simplified into three major components, namely, saturation efficiency (α), spillover factor and ideal PTR.[21] Saturation efficiency is a function of the radiofrequency field applied for saturation (ω_1) and the exchange rate (k_{sw}). Saturation efficiency increases with increasing ω_1 and decreases with increasing k_{ex}. The spillover factor originates from the direct water saturation whereas, an ideal PTR is devoid of other magnetization transfer pathways as well as the spillover factor. The optimum B_1 can be obtained by experimentally tuning the saturation efficiency and the spillover factor. The major drawback of that expression lies in the fact that it does not consider the magnetization transfer contrast, which must be taken care of for *in-vivo* imaging.

Although, conventionally continuous wave rectangular pulses are used for CEST imaging, clinical imaging using continuous wave pulses often raises SAR concerns due to the high field strength of the saturation pulses. The permitted value of field-strength is difficult to quantify as

the specific absorption rate is also dependent upon the type of transmit coil being used. Parallel or smaller transmit coils significantly reduces the heat deposition.[22] Additionally, long (soft) rectangular pulses excite substantial unwanted magnetization outside the desired bandwidth as a rectangular pulse has a sinc excitation response. On the other hand, phase shifted composite pulses such as phase-incremented pulses (PIP) or shifted laminar pulses (SLP) although reduce sensitivity to instrumental artifacts such as rf inhomogeneity, they are extremely sensitive to radiation damping and relaxation effects. Moreover, composite pulses cannot easily achieve a narrow excitation profile.[23] These limit their usefulness as selective pulses. A solution to the problem comes in the form of a train of shaped pulses that are used instead of a single continuous wave rectangular pulse. On the flip side, analytical solution to the modified Bloch equations cannot be obtained for shaped pulses. Also, use of pulsed saturation instead of continuous wave rectangular pulse demands optimization of several additional parameters, that influence the performance of a shaped pulse. The important parameters include pulse duration (τ_p), inter-pulse delay (τ_d), and the shape of the pulse defined by the time dependent B_1 function [$B_1(t)$]. Additionally, the flip angle of the saturation pulse, determined by the net effect of the radiofrequency pulse on a spin over the duration of the pulse and the duty cycle determined by τ_p /($\tau_p + \tau_d$) become important too. McMohan et. al. have demonstrated that with a flip angle of 180^0, the d-SNOB pulse produces approximately similar result to that of a rectangular pulse. Later it was however found that the Fermi pulse shows even a better result for a flip angle of 1620^0 compared to a flip angle of 180^0 at a peak field strength of 3.8 µT.[15] Sun et. al. formulated a reduced expression for optimizing necessary conditions for CEST acquisitions involving certain shaped pulses.[24]

Another characteristic that changes from one shape to another is the shape of the

excitation region. For example, with a steep ramping, the response from a smooth square pulse results in a square excitation profile, whereas, a gaussian pulse produces a gaussian excitation profile.

The third important factor that governs the excitation profile of a shaped pulse is the truncation level at +70 db. This also has some effect on the selectivity change. For example, the bandwidth factors of Gaussian shaped pulse and sinc pulse are close to each other but truncation levels are 4% and 0%, respectively, and hence a sinc shaped pulse gives a slightly better selectivity.

Although pulse shape is an important parameter for CEST and a variety of waveforms have been reported previously in conventional magnetic resonance spectroscopy as well as other magnetization transfer studies,[25-27] not many systematic studies of pulse shape on CEST efficiency has been performed. Available shapes include (among others) fermi, e-burp, d-SNOB, seduce, gaussian and Blackman shaped inversion pulses. Mc Mahon et. al. performed simulations using SPINEVOLUTION to demonstrate the ways to choose the waveform for CEST studies.[15]

In this study, we attempt to see systematically the effect of different shapes on CEST spectra with a special focus on improving CEST efficiency of salicylic acid. We acquired CEST spectra of 25mM salicylic acid (pH 7.4, 37^0C) with nine different pulse shapes namely (i) Reburp.1000, (ii) Pc9_4_90.1000, (iii) Rsnob.1000, (iv) Gauss1_180r.1000, (v) Gauss1_180i.1000, (vi) Esnob.1000, (vii) Seduce.100, (viii) Sinc1.1000, and (ix) Squa100.1000.

The highest CEST contrast (37%) was obtained for Squa100.1000 and the lowest CEST contrast (4%) was obtained for Reburp.1000 (Figure 4). Interestingly, the highest contrast obtained was nearly double the contrast reported (20%) for the same concentration of salicylic acid (keeping other experimental parameters also same) using the same radiofrequency field strength. Pulse

shape turned out to be an extremely important experimental parameter.

In case of diaCEST agents the offset of the exchangeable proton with respect to water is significantly lower as compared to agents containing paramagnetic metal centers. Due to the low offset, the high contamination by water direct saturation (DS) becomes a serious concern for almost all diaCEST agents. DS impacts in two ways. First, for the assessment of true CEST efficiency from the asymmetric magnetization transfer ratio, the normalized water peak intensity obtained by off-resonance saturation at the equal but opposite offset of that of the solute needs to be subtracted, thereby doubling measurement time. If the water direct saturation is significantly high then a wrong assessment of the MTR can possibly be made. Second and more importantly, measurements that demand low DS such as the measurement of exchange rate by the method proposed by Dixon et. al.[8] become erroneous with large water direct saturation. Considering this two things the extent of direct water saturation was measured for all the shaped pulses. It was found that although the effect of DS is higher for Squa100.1000, it is within 2% with a radiofrequency field of upto 15 µT and, therefore, can be used for the measurement of exchange rate without introducing much error.

Squa100.1000 pulse shape produces high efficiency as it's average delivered power is equal to the peak applied power during the entire pulse duration . For all the other shaped pulses we studied, the average power delivered is significantly lower than the power delivered by the Squa pulse given the same peak power and total length. As a result, the efficiency of saturation associated with Squa pulse is significantly higher than the other pulses. Due to this increased efficiency the CEST contrast is also enhanced for this type of shaped pulse. There exists a nearly linear relationship between the average power delivered by a shape and the CEST efficiency produced by that shape. This is very interesting as we have previously seen that pulse width of individual

pulses does not change the CEST efficiency as long as the total saturation is kept constant. Unlike pulse width, the average power delivery has a huge effect on CEST.
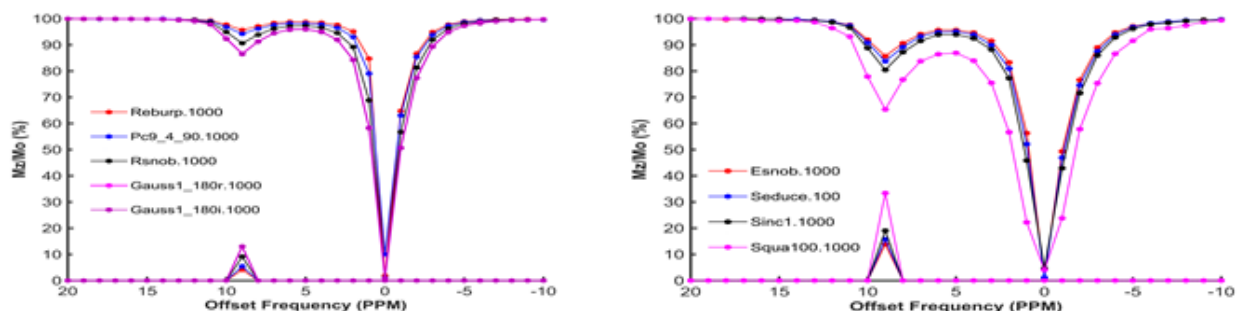

Figure 4: Effect of pulse shape on CEST profile of salicylic acid. The Highest CEST percentage is obtained for Squa 100.1000 pulse shape with 3 s saturation. The pulse length for all the experiment was kept 50 miliseconds with a moderate relaxation delay of 5 s.

To understand clearly the dependency of the average power of a shape on the CEST efficiency it produces, CEST experiments were carried out with Squa100.1000 shaped pulse with suitably adjusted peak power to match the average power to that of the other pulses. For example, the theoretical ratio of average powers of Sinc shaped pulse to that of Squa is 0.45. This means that for a peak power of 7.5 µT, the average power that is actually delivered by a Sinc pulse train for saturation of the exchangeable proton is roughly 3.37 µT. As a result, Sinc shape is comparatively less efficient in incurring saturation upon the exchangeable protons. When CEST experiments were carried out with Squa100.1000 shaped pulse with the peak radiofrequency field strength of 3.37 µT, the amount of CEST contrast as well as the extent of water direct saturation matched exactly with those obtained with Sinc shaped pulse train. A similar observation was made also with the other shapes that we studied (Figure 5.)
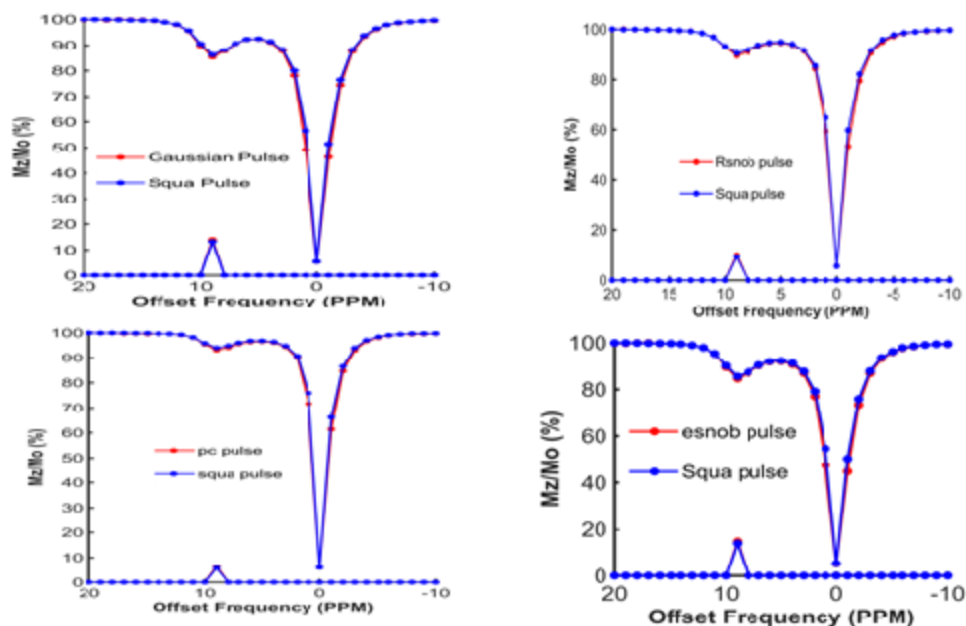
Figure

5: Average power normalized CEST profile with squa 100.1000 shaped pulses with respect to different pulse shapes. Other experimental conditions were kept unchanged.

The analysis points out a very important characteristic of CEST experiment. It is the fact that not only the peak saturating power that generally is mentioned but also the average power delivered by the saturating pulse shape determines the CEST efficiency and direct water saturation. It is therefore important that pulse shapes be explicitly mentioned in any scientific report.

3.5 Calibration of average power delivery by a pulse shape using CEST:

Pulse shapes play an important role in many NMR experiments not necessarily related to MRI contrast generation. For example, decoupling efficiency depends to a large extent on the pulse shape.

Many of the newer pulse shapes that are developed now a days are done by using computer generated alogorithms. These shapes are complicated and are not easily analytically integratable due to rapid intensity and phase modulation. Hence, calculation of average power becomes

tremendously difficult unless performed numerically. In this section of the chapter we discuss how CEST can be utilized as a quick analytical tool to ascertain the average power delivery associated with any given pulse shape in comparison to an already known shape.This is possible based on our erlier reported observation that CEST efficiency is an extremely regular function of average delivered power of the saturating pulse shape.

In order to calibrate the relationship of average power of a shaped pulse to that of the CEST percentage, we bar-plotted the average powers and CEST percentages of the shaped pulses used. The similarity of the two bar-plots (Figure 6) further demonstrates that the CEST percentage is a regular function of the average power delivery associated with different saturating shaped pulses when other parameters are kept unchanged.

We next tried to estimate the average delivered power of a shape from the CEST percentage through comparison to another shape. We then matched that value to the value obtained theoretically (from the shape tool display of the Bruker spectrometer). It was found that the CEST estimated average power correlated well with the known theoretical values.

We found, however, that the correlation is not entirely linear when a Squa pulse shape is used as a standard. In order to investigate further we plotted the average power derived from CEST percentage with the theoretical average power, taking the Sinc shaped pulse as standard and we got a much better linear dependency as shown in Figure 7. We therefore suspected that the average power delivery of the Squa pulse shape is not correctly reported in the shape tool. When we calculated back the average power of Squa with respect to Sinc, we found it to be 79:45 for Squa:Sinc instead of expected 100:45. This further demonstrates the power of CEST as a tool to estimate average power of a shape without any theoretical calculation.
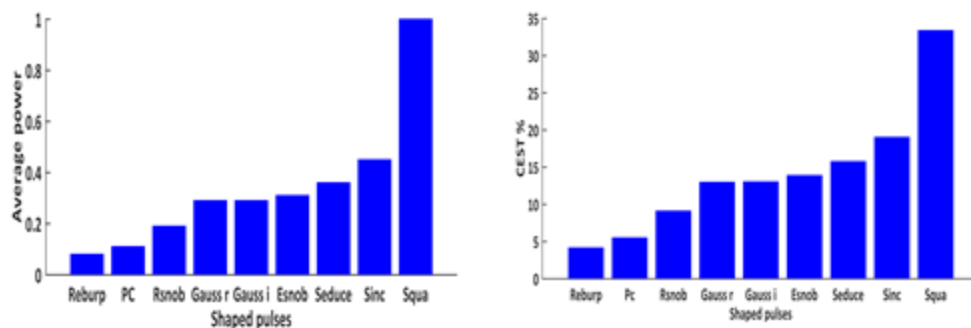
Figure 6: Bar plot of Average power (left) and CEST percentage (right) for different shape pulses. The similarity shows the dependence of CEST percentage on the average power delivery associated with the shaped pulses.
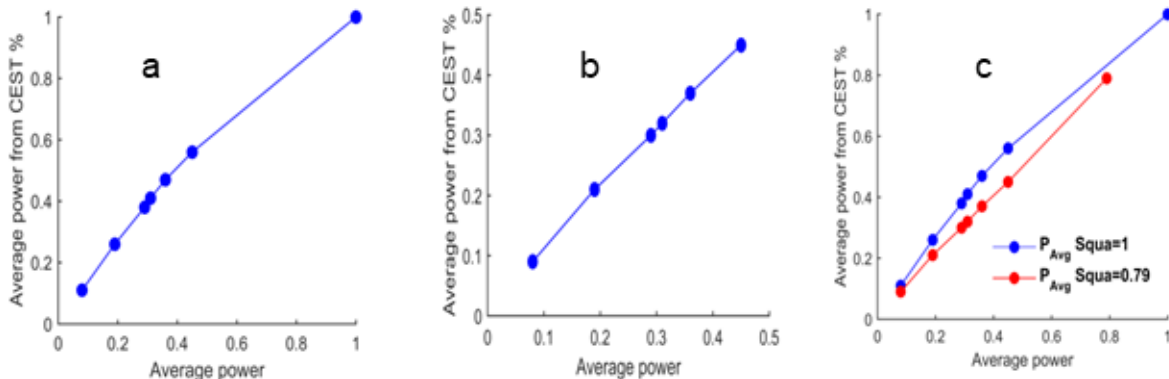

Figure 7: Comparison of theoretical average power to that of determined from CEST percentage. Squa shaped pulse as a standard (a) Sinc shaped pulse as standard (b) Comparison of Squa and Sinc as standard (c).

4. Conclusion

In summary, we have shown that tuning of NMR experimental parameters is equally important in producing optimum contrast as selecting a suitable contrast agent. Among a number of parameters that influence the outcome of a magnetic resonance experiment in general and MRI imaging in particular, we have chosen three parameters here and demonstrated how pulse length, saturation duration, and relaxation delay influence the contrast efficiency. We specifically have shown that

an appropriate choice of pulse shape alone can enhance the CEST efficiency by an appreciable amount.

In a different vein, we introduce CEST as a reliable yet easily implementable analytical tool for quick experimental verification of the theoretical average power delivery associated with a pulse of any shape compared to an already known shape. We anticipate that such a tool would be extremely helpful in designing and optimizing complex computer-generated pulse shapes in future.

References

1.   Caravan, P.; Ellison, J. J.; McMurry, T. J.; Lauffer, R. B., Gadolinium(III) Chelates as MRI Contrast Agents: Structure, Dynamics, and Applications. *Chem. Rev.* **1999,** *99* (9), 2293-352.

2.   Livramento, J. B.; Helm, L.; Sour, A.; O'Neil, C.; Merbach, A. E.; Tóth, É., A benzene-core trinuclear GdIII complex: towards the optimization of relaxivity for MRI contrast agent applications at high magnetic field. *Dalton Trans.* **2008,** (9), 1195-1202.

3.   Ward, K. M.; Aletras, A. H.; Balaban, R. S., A new class of contrast agents for MRI based on proton chemical exchange dependent saturation transfer (CEST). *Journal of magnetic resonance (San Diego, Calif. : 1997)* **2000,** *143* (1), 79-87.

4.   Woods, M.; Woessner, D. E.; Sherry, A. D., Paramagnetic lanthanide complexes as PARACEST agents for medical imaging. *Chem. Soc. Rev.* **2006,** *35* (6), 500-511.
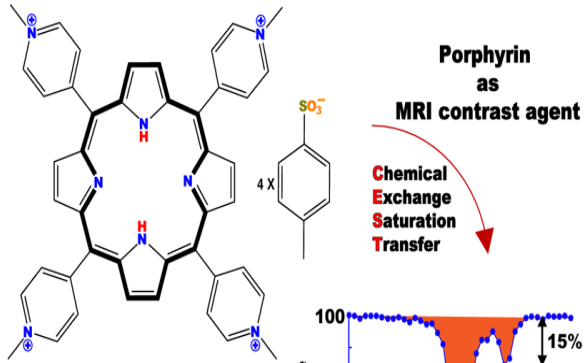
5.   Viswanathan, S.; Kovacs, Z.; Green, K. N.; Ratnakar, S. J.; Sherry, A. D., Alternatives to gadolinium-based metal chelates for magnetic resonance imaging. *Chem. Rev.* **2010,** *110* (5), 2960-3018.

6.   Chan, K. W. Y.; Bulte, J. W. M.; McMahon, M. T., Diamagnetic chemical exchange saturation transfer (diaCEST) liposomes: physicochemical properties and imaging applications. *Wiley Interdiscip Rev Nanomed Nanobiotechnol* **2014,** *6* (1), 111-124.

7.   Tsitovich, P. B.; Cox, J. M.; Spernyak, J. A.; Morrow, J. R., Gear Up for a pH Shift: A Responsive Iron(II) 2-Amino-6-picolyl-Appended Macrocyclic paraCEST Agent That Protonates at a Pendent Group. *Inorg. Chem.* **2016,** *55* (22), 12001-12010.

8.   Dixon, W. T.; Ren, J.; Lubag, A. J.; Ratnakar, J.; Vinogradov, E.; Hancu, I.; Lenkinski, R. E.; Sherry, A. D., A concentration-independent method to measure exchange rates in PARACEST agents. *Magnetic resonance in medicine* **2010,** *63* (3), 625-32.

9.   Chan, K. W. Y.; Yu, T.; Qiao, Y.; Liu, Q.; Yang, M.; Patel, H.; Liu, G.; Kinzler, K. W.; Vogelstein, B.; Bulte, J. W. M.; van Zijl, P. C. M.; Hanes, J.; Zhou, S.; McMahon, M. T., A diaCEST MRI approach for monitoring liposomal accumulation in tumors. *J Control Release* **2014,** *180*, 51-59.

10.   Longo, D. L.; Dastrù, W.; Digilio, G.; Keupp, J.; Langereis, S.; Lanzardo, S.; Prestigio, S.; Steinbach, O.; Terreno, E.; Uggeri, F.; Aime, S., Iopamidol as a responsive MRI-chemical exchange saturation transfer contrast agent for pH mapping of kidneys: In vivo studies in mice at 7 T. *Magnetic resonance in medicine* **2011,** *65* (1), 202-11.

11.   Longo, D. L.; Sun, P. Z.; Consolino, L.; Michelotti, F. C.; Uggeri, F.; Aime, S., A general MRI-CEST ratiometric approach for pH imaging: demonstration of in vivo pH mapping with iobitridol. *J. Am. Chem. Soc.* **2014,** *136* (41), 14333-6.

12.   Bar-Shir, A.; Liu, G.; Chan, K. W. Y.; Oskolkov, N.; Song, X.; Yadav, N. N.; Walczak, P.; McMahon, M. T.; van Zijl, P. C. M.; Bulte, J. W. M.; Gilad, A. A., Human protamine-1 as an MRI reporter gene based on chemical exchange. *ACS Chem Biol* **2014,** *9* (1), 134-138.

13.   van Zijl, P. C.; Jones, C. K.; Ren, J.; Malloy, C. R.; Sherry, A. D., MRI detection of glycogen in vivo by using chemical exchange saturation transfer imaging (glycoCEST). *Proc Natl Acad Sci U S A* **2007,** *104* (11), 4359-64.

14.   van Zijl, P. C.; Yadav, N. N., Chemical exchange saturation transfer (CEST): what is in a name and what isn't? *Magnetic resonance in medicine* **2011,** *65* (4), 927-48.

15.   Liu, G.; Song, X.; Chan, K. W. Y.; McMahon, M. T., Nuts and bolts of chemical exchange saturation transfer MRI. *NMR Biomed.* **2013,** *26* (7), 810-828.

16.   Yang, X.; Song, X.; Li, Y.; Liu, G.; Ray Banerjee, S.; Pomper, M. G.; McMahon, M. T., Salicylic Acid and Analogues as diaCEST MRI Contrast Agents with Highly Shifted Exchangeable Proton Frequencies. *Angew. Chem. Int. Ed.* **2013,** *52* (31), 8116-8119.

17.   Yang, X.; Yadav, N. N.; Song, X.; Ray Banerjee, S.; Edelman, H.; Minn, I.; van Zijl, P. C. M.; Pomper, M. G.; McMahon, M. T., Tuning Phenols with Intra-Molecular Bond Shifted HYdrogens (IM-SHY) as diaCEST MRI Contrast Agents. *Chem. Eur. J.* **2014,** *20* (48), 15824-15832.

18.   McMahon, M. T.; Gilad, A. A.; Zhou, J.; Sun, P. Z.; Bulte, J. W. M.; van Zijl, P. C. M., Quantifying exchange rates in chemical exchange saturation transfer agents using the saturation time and saturation power dependencies of the magnetization transfer effect on the magnetic resonance imaging signal (QUEST and QUESP): Ph calibration for poly-L-lysine and a starburst dendrimer. *Magnetic resonance in medicine* **2006,** *55* (4), 836-847.
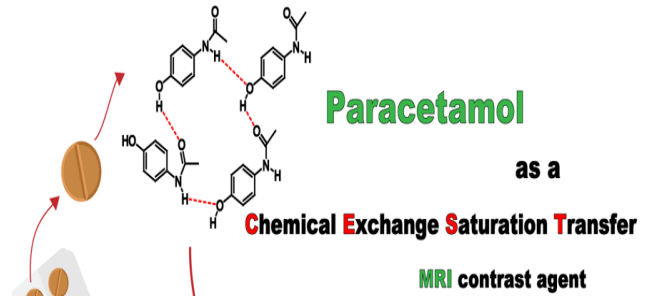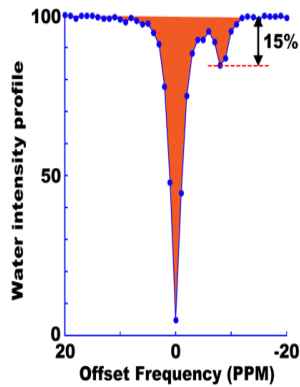
19.   Woessner, D. E.; Zhang, S.; Merritt, M. E.; Sherry, A. D., Numerical solution of the Bloch equations provides insights into the optimum design of PARACEST agents for MRI. *Magnetic resonance in medicine* **2005,** *53* (4), 790-9.

20.   Sun, P. Z.; Zhou, J.; Huang, J.; van Zijl, P., Simplified quantitative description of amide proton transfer (APT) imaging during acute ischemia. *Magnetic resonance in medicine* **2007,** *57* (2), 405-10.

21.   Sun, P. Z.; van Zijl, P. C.; Zhou, J., Optimization of the irradiation power in chemical exchange dependent saturation transfer experiments. *Journal of magnetic resonance (San Diego, Calif. : 1997)* **2005,** *175* (2), 193-200.

22.   Tse, D. H. Y.; da Silva, N. A.; Poser, B. A.; Shah, N. J., inhomogeneity mitigation in CEST using parallel transmission. *Magnetic resonance in medicine* **2017,** *78* (6), 2216-2225.

23.   Cavanagh, J.; Fairbrother, W. J.; Palmer, A. G.; Rance, M.; Skelton, N. J., CHAPTER 3 - EXPERIMENTAL ASPECTS OF NMR SPECTROSCOPY. In *Protein NMR Spectroscopy (Second Edition)*, Cavanagh, J.; Fairbrother, W. J.; Palmer, A. G.; Rance, M.; Skelton, N. J., Eds. Academic Press: Burlington, 2007; pp 114-270.

24.   Sun, P. Z.; Benner, T.; Kumar, A.; Sorensen, A. G., Investigation of optimizing and translating pH-sensitive pulsed-chemical exchange saturation transfer (CEST) imaging to a 3T clinical scanner. *Magnetic resonance in medicine* **2008,** *60* (4), 834-41.

25.   Meldrum, T.; Bajaj, V. S.; Wemmer, D. E.; Pines, A., Band-selective chemical exchange saturation transfer imaging with hyperpolarized xenon-based molecular sensors. *Journal of magnetic resonance (San Diego, Calif. : 1997)* **2011,** *213* (1), 14-21.

26.   Dixon, W. T.; Hancu, I.; Ratnakar, S. J.; Sherry, A. D.; Lenkinski, R. E.; Alsop, D. C., A multislice gradient echo pulse sequence for CEST imaging. *Magnetic resonance in medicine* **2010,** *63* (1), 253-6.

27.   Aime, S.; Delli Castelli, D.; Terreno, E., Novel pH-reporter MRI contrast agents. *Angew. Chem. Int. Ed. Engl.* **2002,** *41* (22), 4334-6.

Summary

Porphyrin as MRI contrast agent

Chemical
Exchange
Saturation
Transfer

- High contrast
- Good contrast at all pH
- No unsafe metal ion
- Negligible metal affinity

Paracetamol as a **C**hemical **E**xchange **S**aturation **T**ransfer **MRI contrast agent**

- Safe
- Good contrast
- No metal ion